CHAPTER FIVE

# Optical coherence and electromagnetic surface waves

**Yahong Chen[a,b], Andreas Norrman[c,d], Sergey A. Ponomarenko[e,f], Ari T. Friberg[a]**

[a]Institute of Photonics, University of Eastern Finland, Joensuu, Finland
[b]School of Physical Science and Technology, Soochow University, Suzhou, China
[c]Max Planck Institute for the Science of Light, Erlangen, Germany
[d]Photonics Laboratory, ETH Zurich, Zurich, Switzerland
[e]Department of Electrical and Computer Engineering, Dalhousie University, Halifax, NS, Canada
[f]Department of Physics and Atmospheric Science, Dalhousie University, Halifax, NS, Canada

## Contents



*Progress in Optics*, Volume 65
ISSN 0079-6638
https://doi.org/10.1016/bs.po.2019.11.001

## Abstract

The subject of this review lies at the cross-roads of optical coherence theory and surface wave physics. We first recall how electromagnetic surface waves affect the spectrum, polarization, and spatial correlation properties of thermal near fields. We then discuss the modulation, control, and measurement of spatial coherence of random optical beams by surface plasmon polaritons (SPPs). We review the spectral polarization and subwavelength coherence of three-dimensional evanescent fields. Finally, we examine polychromatic, structured SPP fields of tailored electromagnetic coherence.

**Keywords:** Coherence, Polarization, Spectrum, Surface plasmon polaritons, Evanescent waves, Structured fields, Thermal light, Optical beams

## 1. Introduction

Emil Wolf laid down the foundation of classical optical coherence theory by introducing a (second-order) mutual coherence function and showing that its free-space propagation is governed by a pair of coupled wave equations bearing his name (Wolf, 1955). His subsequent pioneering work (Wolf, 1956, 1959) has extended the scalar optical coherence theory into the electromagnetic realm through introducing the concept of the degree of polarization of beam-like electromagnetic fields (Wolf, 1959). Emil Wolf and collaborators have also derived fundamental conservation laws involving electromagnetic field correlations (Roman & Wolf, 1960a, 1960b), thereby establishing that electromagnetic field correlations propagate in the form of waves in free space. Wolf has then made another fundamental contribution to the subject by establishing a mathematically rigorous space–frequency representation of stationary random source ensembles and the fields they produce in terms of the source coherent modes (Wolf, 1981, 1982). Not merely do these seminal achievements furnish deeper insights into the second-order coherence structure of random electromagnetic sources and their generated fields, but the foundations established by Emil Wolf facilitate the discovery, characterization, and exploitation of new classes of partially coherent, complex-structured electromagnetic fields as we will demonstrate in this review.

To date, coherence has emerged as a central degree of freedom in optical physics and it has played an important role in understanding and fine-tuning fundamental properties of light and light–matter interactions (Mandel & Wolf, 1995). It is now well established that controlling optical coherence enables to tailor the spatial, spectral, and polarization distributions of propagating statistical beams (Cai, Chen, Yu, Liu, & Liu, 2017). Such partially

coherent optical beams are superior with respect to their fully coherent counterparts in a number of applications, such as speckle-free imaging (Redding, Choma, & Cao, 2012), ghost imaging (Erkmen & Shapiro, 2010; Shirai, 2017), information transfer through random environments (Gbur, 2014), and microparticle trapping and manipulation (Auñón & Nieto-Vesperinas, 2013). Electromagnetic surface waves, whose attractiveness comes from their unique capacity of strong confinement and long-range guidance of electromagnetic energy along the supporting interface, are ubiquitous in optical science as well and have gained ever-growing interest (Polo, Mackay, & Lakhtakia, 2013). Among them evanescent waves (de Fornel, 2001) and the celebrated surface polaritons (Agranovich & Mills, 1982), manifested in forms of plasmons, phonons, excitons, and magnons, have especially occupied a pivotal position in modern nanophotonics (Novotny & Hecht, 2012). The recent application of optical coherence theory to electromagnetic surface waves has led to instructive fundamental insights and results that constitute the subject of this review.

We address, on the one hand, the impacts of surface polaritons on external optical fields and examine, on the other hand, the coherence and polarization properties of physically important surface excitations, namely evanescent waves and surface plasmon polariton (SPP) fields. More specifically, we discuss how the salient characteristics, such as the near-field spectrum, correlation length, and degree of polarization, of thermal radiation from primary half-space sources in thermal equilibrium strongly depend on whether any surface polaritons are excited in the system. We then show that SPPs can be utilized to manipulate, control, and measure spatial coherence of propagating optical beams in a Young-type interference experiment with finite-size slits in a metal screen. We review the unique polarization features and subwavelength coherence structure associated with genuinely three-dimensional, partially coherent evanescent waves created by total internal reflection at a dielectric interface. Finally, we demonstrate how the recently advanced notion of plasmon coherence engineering enables one to design polychromatic, complex-structured SPP fields of arbitrary state of coherence, endowed with nontrivial and versatile field intensity, polarization, energy flow, and angular momentum distributions.

Emil Wolf has directly or indirectly mentored generations of scientists in optical physics from all over the world. Indeed, two of the authors of this article (S.A.P. and A.T.F.) are former students of Emil Wolf and the other two (Y.C. and A.N.) are their students. It is truly our honor and privilege to dedicate this review to Professor Emil Wolf, our mentor and the pioneer of optical coherence theory.

## 2. Surface-wave impacts on thermal field coherence

Thermal radiation is an electromagnetic field induced by the randomly fluctuating motion of particles in matter. All natural objects, ranging from biological systems to astrophysical entities, emit thermal radiation, and numerous applications, such as thermographic cameras, solar photovoltaic systems, and lighting arrangements, exploit thermal light. Due to its high spatial isotropy, broadband spectrum, and random polarization, thermal radiation is generally regarded as an incoherent light field. Nonetheless, ever since the advent of modern optical coherence theory, it has been known that the electromagnetic field emitted by a thermal source exhibits at least some degree of coherence (Mandel & Wolf, 1995). In particular, the classical coherence and polarization properties of universal blackbody radiation within a cavity, in an aperture, and in the aperture far zone have been extensively studied (Blomstedt, Friberg, & Setälä, 2017). It is now also well established that the statistical characteristics of a thermal near field may differ significantly from those of the thermal far field (Jones, O'Callahan, Yang, & Raschke, 2013), offering many exciting opportunities for thermophotonic engineering and management (Liu, Wang, & Zhang, 2015).

The presence of electromagnetic surface waves, in particular, can strongly modulate the coherence, spectrum, and polarization of the thermal near field (Joulain, Mulet, Marquier, Carminati, & Greffet, 2005). The spatial correlations in thermal near-field radiation may extend over several tens of wavelengths when surface polaritons are involved (Carminati & Greffet, 1999; Henkel, Joulain, Carminati, & Greffet, 2000). Likewise, a thermal broadband near field can become essentially quasimonochromatic (Babuty, Joulain, Chapuis, Greffet, & De Wilde, 2013; Shchegrov, Joulain, Carminati, & Greffet, 2000) and highly polarized (Setälä, Kaivola, & Friberg, 2002) under surface-polariton excitations. By imparting a linear momentum onto the surface waves via a grating structure, objects in thermal equilibrium can emit radiation in the form of spatially coherent beam lobes of directionally dependent spectra (Greffet et al., 2002; Han & Norris, 2010; Park, Han, Nagpal, & Norris, 2016). Besides gratings, coherent thermal field emission can also be created by resonant photonic crystals and metamaterials (Inoue, De Zoysa, Asano, & Noda, 2014; Laroche, Carminati, & Greffet, 2006; Lee, Fu, & Zhang, 2005; Liu et al., 2011; Pralle et al., 2002). In this section, we review the extraordinary impacts that electromagnetic surface-wave resonances have on the spatial correlations, the spectrum, and the degree of polarization of thermally excited light fields.

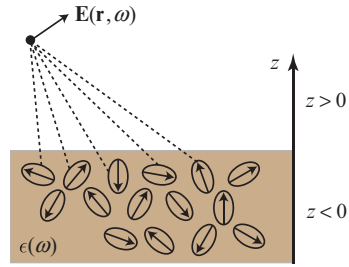


**Fig. 1** Schematic of the microscopic origin of thermal radiation. The random electric field $\mathbf{E}(\mathbf{r}, \omega)$ at angular frequency $\omega$ above the surface ($z > 0$) is emitted by the fluctuating currents or polarization fluctuations within the medium ($z < 0$) of complex permittivity $\epsilon(\omega)$. The random source currents in the medium are related to the induced radiation field through the Green tensor of the system.

## 2.1 Thermal light fields

Let us consider a homogeneous, isotropic, and nonmagnetic thermal source filling the half-space $z < 0$ (see Fig. 1). The source medium is in local thermodynamic equilibrium at a uniform temperature $T$ and described by a complex relative permittivity $\epsilon(\omega)$ at angular frequency $\omega$. Hereafter we will refer to $\epsilon(\omega)$ as simply the *complex permittivity*. The thermal motion of the source charges induces a fluctuating, statistically stationary electric current in the medium, which in turn generates a thermal radiation field above the source ($z > 0$). We let $\mathbf{E}(\mathbf{r}, \omega)$ represent a monochromatic realization of the thermal electric field at position $\mathbf{r}$ in the space–frequency domain. The field $\mathbf{E}(\mathbf{r}, \omega)$ can then be expressed via the associated Green tensor as (Carminati & Greffet, 1999)

$$\mathbf{E}(\mathbf{r},\omega) = \mathrm{i}\mu_0\omega \int_V \mathbf{G}(\mathbf{r},\mathbf{r}',\omega)\cdot\mathbf{j}(\mathbf{r}',\omega)\mathrm{d}^3\mathbf{r}', \tag{1}$$

where $\mu_0$ is the vacuum permeability, $\mathbf{j}(\mathbf{r}', \omega)$ is the electric current density at location $\mathbf{r}'$ within the source medium, and the integration volume $V$ covers the whole half-space $z < 0$. The *Green tensor* $\mathbf{G}(\mathbf{r}, \mathbf{r}', \omega)$, being essentially a spatial transfer function between the source current $\mathbf{j}(\mathbf{r}', \omega)$ and the resultant electric field $\mathbf{E}(\mathbf{r}, \omega)$, is conveniently expressed as a superposition of reflected and refracted plane waves at the surface $z = 0$ (Carminati & Greffet, 1999). The nonradiating evanescent waves, resulting from total internal reflections at the interface, are thus fully taken into account. Moreover, since the Green tensor is explicitly equipped with the Fresnel coefficients, all surface polariton effects are also naturally manifested, as they correspond to the presence of a pole in the transmission coefficient for $p$-polarized light.

The second-order correlation properties of the thermal field, at points $\mathbf{r}_1$ and $\mathbf{r}_2$, can then be characterized in the space–frequency domain by the 3 × 3 *spectral electric coherence matrix* (Friberg & Setälä, 2016; Tervo, Setälä, & Friberg, 2004)

$$\mathbf{W}(\mathbf{r}_1, \mathbf{r}_2, \omega) = \langle \mathbf{E}^*(\mathbf{r}_1, \omega)\mathbf{E}^{\mathrm{T}}(\mathbf{r}_2, \omega)\rangle, \tag{2}$$

where the asterisk, superscript T, and angle brackets denote the complex conjugate, matrix transpose, and ensemble average, respectively. The statistical character of the thermal field originates from the randomly fluctuating electric current densities, whose correlations at points $\mathbf{r}_1'$ and $\mathbf{r}_2'$ within the source are governed by the *fluctuation–dissipation theorem* (Jones et al., 2013)

$$\langle \mathbf{j}^*(\mathbf{r}_1', \omega)\mathbf{j}^{\mathrm{T}}(\mathbf{r}_2', \omega)\rangle = \frac{\omega}{\pi}\epsilon_0\epsilon''(\omega)\Theta(\omega, T)\delta(\mathbf{r}_1' - \mathbf{r}_2')\mathbf{I}. \tag{3}$$

Here $\epsilon_0$ is the vacuum permittivity, $\epsilon''(\omega)$ is the imaginary part of the complex permittivity of the medium, $\Theta(\omega, T)$ is the mean energy of a Planck oscillator, $\delta(\mathbf{r}_1' - \mathbf{r}_2')$ is the Dirac delta function, and $\mathbf{I}$ is the 3 × 3 unit matrix. It then follows from Eqs. (1)–(3) that the electric coherence matrix of the thermal radiation field can be written as

$$\mathbf{W}(\mathbf{r}_1, \mathbf{r}_2, \omega) = \frac{\omega^3}{\pi}\mu_0^2\epsilon_0\epsilon''(\omega)\Theta(\omega, T)\int_V \mathbf{G}^*(\mathbf{r}_1, \mathbf{r}', \omega)\mathbf{G}^{\mathrm{T}}(\mathbf{r}_2, \mathbf{r}', \omega)\mathrm{d}^3\mathbf{r}', \tag{4}$$

which contains all the information about the spectral correlations among the orthogonal thermal field components at the two points. Moreover, it has been shown that $\mathbf{W}(\mathbf{r}_1, \mathbf{r}_2, \omega) \propto \mathbf{G}''(\mathbf{r}_1, \mathbf{r}_2, \omega)$, i.e., the spatial coherence properties of the field are described by the spatial dependence of the imaginary part of the Green tensor (Setälä, Blomstedt, Kaivola, & Friberg, 2003).

## 2.2 Spatial correlation changes

Conventional wisdom in optical coherence theory presumes that spatial correlations in the electromagnetic field extend, *at least*, over distances on the order of the wavelength (Foley, Carter, & Wolf, 1986; Foley, Kim, & Nussenzveig, 1988). Such a presumption has been tested by rigorous calculations pertaining to fields emitted by thermal half-space sources (Carminati & Greffet, 1999; Henkel et al., 2000). Some key results are presented in Fig. 2. If the source consists of slightly lossy glass, the field correlations along the surface, such as $W_{xx}(\mathbf{r}_1, \mathbf{r}_2, \omega) = \langle E_x^*(\mathbf{r}_1, \omega)E_x(\mathbf{r}_2, \omega)\rangle$, indeed behave as $\mathrm{sinc}(k\rho)$ very close to the interface, where $k$ is the free-space wave number and $\rho = |\mathbf{r}_1 - \mathbf{r}_2|$. This behavior is characteristic of

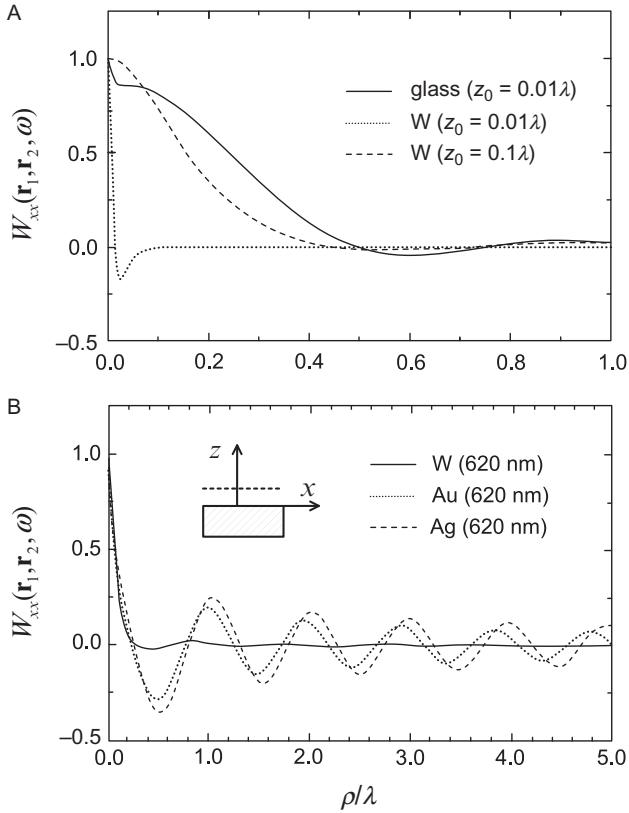


**Fig. 2** Coherence matrix component $W_{xx}(\mathbf{r}_1, \mathbf{r}_2, \omega)$ of the near-field thermal radiation as a function of the distance $\rho = |\mathbf{r}_1 - \mathbf{r}_2|$ at fixed height $z_0$ above a semiinfinite thermal half-space source. (A) Lossy glass and tungsten (W) (at two heights) at wavelength $\lambda = 500$ nm. (B) Tungsten (W), gold (Au), and silver (Ag) for $\lambda = 620$ nm and $z_0 = 0.05\lambda$. All curves are normalized by their maximum at $\rho = 0$. *From Carminati, R., & Greffet, J.-J. (1999). Near-field effects in spatial coherence of thermal sources. Physical Review Letters, 82(8), 1660–1663.*

radiation of a planar blackbody (Blomstedt et al., 2017). However, if the medium is tungsten (W), which reveals strong absorption at the free-space wavelength $\lambda = 500$ nm, the longitudinal correlation length close to the source surface is *very short*, only on the order of $0.06\lambda$, corresponding to about the skin depth of tungsten at this particular wavelength. When moving farther away from the boundary, the field coherence assumes the typical blackbody form, as seen in Fig. 2A. The extremely narrow, quite unusual spatial correlations in the immediate vicinity of a tungsten source are explained by absorption, causing the loss of field correlations over a

skin-depth distance within the medium (Carminati & Greffet, 1999; Henkel et al., 2000). In principle, a finite-sized source can produce a light field whose coherence length within the source may be arbitrarily short, even in the absence of absorption (Blomstedt, Setälä, & Friberg, 2007a).

The coherence behavior is quite different if electromagnetic *surface-wave resonances* are present. For example, at $\lambda = 620$ nm, both silver (Ag) and gold (Au) support surface plasmon polaritons (SPPs). The SPP presence is manifested in field correlations, as shown in Fig. 2B, where the spatial correlation $W_{xx}(\mathbf{r}_1, \mathbf{r}_2, \omega)$ oscillates and has an exponentially decaying envelope. The decay lengths of the correlations are much longer than the wavelength, on the order of the SPP propagation lengths $16\lambda$ (Au) and $65\lambda$ (Ag), indicating that the fields are coherent over long distances along the interface. Similar *long-range correlations* occur for silicon carbide (SiC) at $\lambda = 11.36\ \mu$m when a surface phonon polariton is generated (Carminati & Greffet, 1999). Such long-range coherences seem unexpected because the fluctuating currents are $\delta$-correlated, as dictated by the fluctuation–dissipation theorem in Eq. (3). Actually, an increase in the spatial coherence of a statistically homogeneous planar source has the effect of diminishing the long-range correlation of the near field under surface-wave resonances (Auñón & Nieto-Vesperinas, 2011).

## 2.3 Spectral changes

Surface-wave excitations can also strongly affect the *temporal coherence* of the thermal near field via changes in the *spectral density* (or spectrum)

$$S(\mathbf{r}, \omega) = \mathrm{tr}\mathbf{W}(\mathbf{r}, \mathbf{r}, \omega), \tag{5}$$

where tr denotes the matrix trace. Fig. 3 displays the spectral density of the thermal radiation for a semiinfinite SiC source at $T = 300$ K at different heights above the surface. It is observed from Fig. 3A that the radiation spectrum in the far field is broadband in the frequency range $0 < \omega < 400 \cdot 10^{12}\ \mathrm{s}^{-1}$, indicating poor temporal coherence of the field. As the distance from the source is decreased, the contribution to the energy density is increasingly more confined to a narrow volume at the surface (Shchegrov et al., 2000), with a corresponding decrease in the linewidth and increase in the temporal coherence. As shown in Fig. 3C, in the very near field (height $z_a \ll \overline{\lambda}$, where the mean wavelength of the radiation is about $\overline{\lambda} \approx 10\ \mu$m) the spectrum is *virtually monochromatic* at the central frequency $\omega_0 = 178.7 \cdot 10^{12}\ \mathrm{s}^{-1}$. At the frequency $\omega_0$ the real part of the material complex permittivity $\epsilon'(\omega_0) = -1$, an indication that near $\omega_0$ there exist a large number of surface

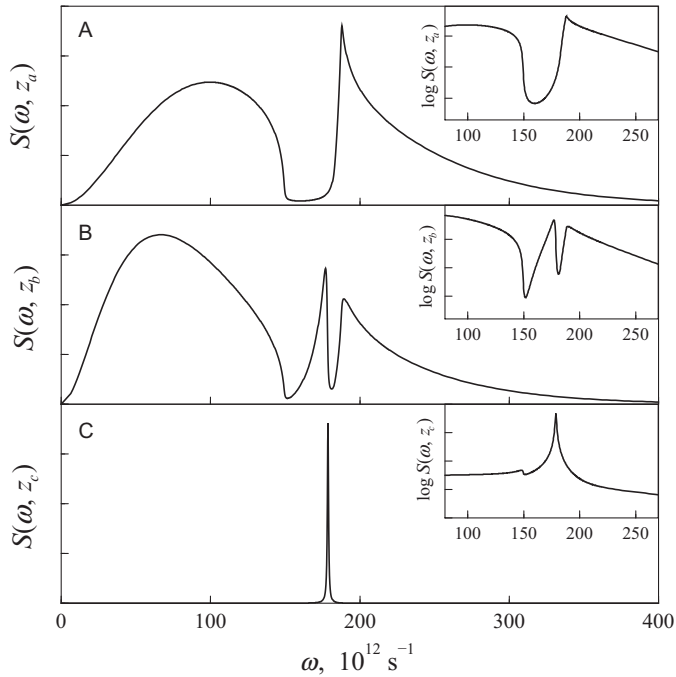


**Fig. 3** Spectral density $S(\omega, z)$ of the thermal field for a semiinfinite SiC sample at temperature $T = 300$ K at three different heights above the surface: (A) $z_a = 1000\ \mu$m, (B) $z_b = 2\ \mu$m, (C) $z_c = 0.1\ \mu$m. The insets show the spectral density on a semilog scale in the region of strong contributions from evanescent surface modes. *From Shchegrov, A. V., Joulain, K., Carminati, R., & Greffet, J.-J. (2000). Near-field spectral effects due to electromagnetic surface excitations. Physical Review Letters, 85(7), 1548–1551.*

modes with different wave numbers but with frequencies that are very close to each other (Joulain et al., 2005). The density of surface modes will thus necessarily display a strong peak at $\omega = \omega_0$, but since the modes decay exponentially away from the surface the peak vanishes in the far zone. In more general scenarios, it is not only the surface waves but also the spatial coherence of the source that modulate the spectrum (Roychowdhury & Wolf, 2003) as well as the spatial correlations (Apostol & Dogariu, 2003) of an electromagnetic near field.

## 2.4 Polarization changes

The thermal radiation is a genuine *three-component* electric field whose polarization properties are in the space–frequency domain described by the $3 \times 3$ *spectral polarization matrix* (Gil & Ossikovski, 2016)

$$\mathbf{\Phi}(\mathbf{r}, \omega) = \mathbf{W}(\mathbf{r}, \mathbf{r}, \omega). \tag{6}$$

For a two-component field, the associated $2 \times 2$ polarization matrix can be written unambiguously as a sum of two matrices, one describing unpolarized light and the other polarized light, and in this case the *degree of polarization* is defined as the ratio of the spectral density of the polarized part to that of the total field (Mandel & Wolf, 1995). For the $3 \times 3$ polarization matrix, however, such a decomposition does not generally exist (Brosseau, 1998; Gil & Ossikovski, 2016), rendering the concept of degree of polarization more involved (Gil, Norrman, Friberg, & Setälä, 2018b).

To quantify the degree of polarization or the *degree of polarimetric purity* (Gil, 2007; Gil & Ossikovski, 2016; Gil & San José, 2010) of an arbitrary three-component field, one may use the measure (Setälä, Kaivola, & Friberg, 2002; Setälä, Shevchenko, Kaivola, & Friberg, 2002)

$$P_{3D}(\mathbf{r}, \omega) = \sqrt{\frac{3}{2}\left[\frac{\mathrm{tr}\boldsymbol{\Phi}^2(\mathbf{r}, \omega)}{\mathrm{tr}^2\boldsymbol{\Phi}(\mathbf{r}, \omega)} - \frac{1}{3}\right]}, \tag{7}$$

which is invariant under unitary operations and satisfies $0 \leq P_{3D}(\mathbf{r}, \omega) \leq 1$. The upper bound $P_{3D}(\mathbf{r}, \omega) = 1$ describes polarized light and is encountered only if all the field components are completely correlated. The lower bound $P_{3D}(\mathbf{r}, \omega) = 0$ represents unpolarized light in the full *three-dimensional sense*: the spectral densities of the three orthogonal components are the same and no correlation exists between them in any reference frame. In fact, the quantity $P_{3D}(\mathbf{r}, \omega)$ can be interpreted as describing how far the state $\boldsymbol{\Phi}(\mathbf{r}, \omega)$ is from such a fully unpolarized light state (necessarily proportional to the $3 \times 3$ unit matrix) (Luis, 2005). It can also be viewed as a measure characterizing the intensity and spin anisotropy of a three-component field (Gil, Norrman, Friberg, & Setälä, 2019). In a frame where the diagonal elements of $\boldsymbol{\Phi}(\mathbf{r}, \omega)$ are equal, $P_{3D}(\mathbf{r}, \omega)$ turns into a direct measure for the average correlations among the three orthogonal field components (Setälä, Shevchenko, et al., 2002), analogously to the traditional degree of polarization for planar, two-component beam fields (Born & Wolf, 1999). Likewise, one may construct $P_{3D}(\mathbf{r}, \omega)$ via expanding the polarization matrix in terms of the Gell-Mann matrices and the generalized Stokes parameters (Setälä, Shevchenko, et al., 2002), similarly to the Pauli matrices and the Stokes parameters for the usual degree of polarization (Mandel & Wolf, 1995).

Fig. 4 illustrates the degree of polarization $P_{3D}(\mathbf{r}, \omega)$ of the near-field thermal radiation as a function of the height $z$ above a source consisting of Au and SiC (both at two wavelengths) as well as glass. Because glass does not support electromagnetic surface waves, the degree of polarization decays

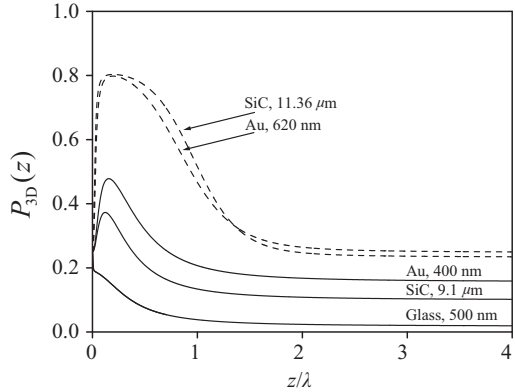


**Fig. 4** Degree of polarization $P_{3D}(z)$ of the thermal near field at certain wavelengths $\lambda$ as a function of the height $z$ above some semiinfinite sources at temperature $T = 300$ K. *From Setälä, T., Kaivola, M., & Friberg, A. T. (2002). Degree of polarization in near fields of thermal sources: Effects of surface waves. Physical Review Letters, 88(12), 123902.*

monotonically as $z$ increases due to the loss of the evanescent modes. On the other hand, for Au at $\lambda = 620$ nm an *SPP resonance* takes place, rendering the near field *strongly polarized* with a peak value of $P_{3D}(\mathbf{r}, \omega) = 0.8$ at height $z \approx 0.2\lambda$. A similar behavior is observed in the near field of the SiC source at $\lambda = 11.36$ $\mu$m, corresponding to a surface phonon polariton. However, tuning the wavelength off resonance reduces the degree of polarization significantly, as evidenced by the curves for Au at $\lambda = 400$ nm and for SiC at $\lambda = 9.1$ $\mu$m. The abrupt reduction of $P_{3D}(\mathbf{r}, \omega)$ in the very near field, with $P_{3D}(\mathbf{r}, \omega) \to 1/4$ in the limit $z \to 0$ irrespective of the material (Setälä, Kaivola, & Friberg, 2002), is caused by the so-called quasistatic field which dominates over the surface waves or any other effects immediately above the source (Henkel et al., 2000).

## 2.5 Highly directional thermal beams

So far the discussion has concerned surface-wave impacts on the thermal *near field*. Indeed, since the surface waves are strongly evanescent in nature, their influence on the thermal *far field* seems completely negligible. Yet, quite remarkably, if a linear momentum is imparted onto the surface waves, they may alter the thermal far-field radiation dramatically. In particular, a grating structure can be employed to efficiently convert electromagnetic surface waves into propagating fields, giving rise to *directional emission* of almost *coherent radiation* from thermal sources at certain wavelengths (Greffet et al., 2002). By properly choosing the period of the grating, it is possible to

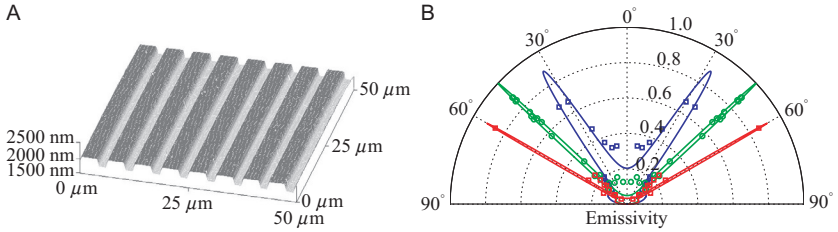


**Fig. 5** Coherent thermal emission from a silicon carbide (SiC) micrograting. (A) Image of the SiC grating obtained by atomic force microscopy. (B) Emissivity for *p* polarization in the far field as a function of the emission angle at wavelength $\lambda = 11.04\ \mu$m (blue), $\lambda = 11.36\ \mu$m (red), and $\lambda = 11.86\ \mu$m (green). Experimental data at ambient temperature are indicated by circles; the lines show the theoretical results. *From Greffet, J.-J., Carminati, R., Joulain, K., Mulet, J.-P., Mainguy, S., & Chen, Y. (2002). Coherent emission of light by thermal sources. Nature, 416(6876), 61–64.*

control the angle of propagation of the radiated field. Fig. 5A shows a SiC grating, with the angular emission pattern at room temperature displayed in Fig. 5B. We observe that the grating radiates infrared light into a very narrow solid angle to the far field, an indication of a large coherence width in each lobe. One finds also that the emission spectrum of the radiation depends strongly on the observation direction.

More recently, a two-dimensional periodic microstructure, ruled on polar material, was reported to create a spectrally narrow and highly directional thermal emission beam (Han & Norris, 2010; Park et al., 2016). Fig. 6A shows such a two-dimensional arrangement with a specific bull's eye structure of tungsten. The calculated emissivity at $T = 25°$C for grooves with a period of 3.5 $\mu$m, depth of 1.825 $\mu$m, and width of 1.925 $\mu$m is displayed in Figs. 6B and C, while the measured emissivity at $T = 900°$C with respective groove dimensions 3.52 $\mu$m, 0.18 $\mu$m, and 1.76 $\mu$m is shown in Figs. 6D and E. In this configuration, cavity modes are excited inside the grooves which then couple coherently to each other by the delocalized surface waves. At the cavity resonance frequency the coherence length can be greatly enhanced, yielding a narrow angular width of narrowband thermal emission in the plane perpendicular to the grating. Such highly directional and frequency-selective thermal emission in the far field, induced by surface-wave modulation of the near-field coherence, leads to several exciting opportunities for new energy applications, including energy harvesting, local thermal control and management, daytime radiative cooling, nanoscale infrared imaging and mapping, and nanomanufacturing (Li & Fan, 2018).

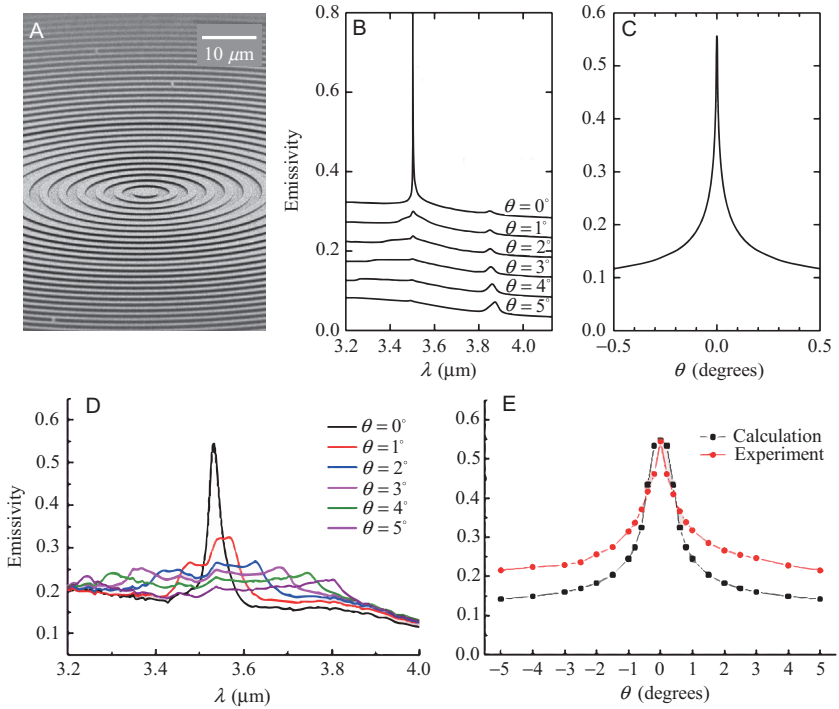


**Fig. 6** Beaming thermal emission by a two-dimensional bull's eye pattern of tungsten (W). (A) Electron micrograph of a bull's eye pattern on a W film. (B) Calculated emissivity spectra at various angles $\theta$ from the surface normal, and (C) angular dependence of the emissivity at the peak wavelength $\lambda = 3.502$ $\mu$m, for grooves having a period, depth, and width of 3.5 $\mu$m, 1.825 $\mu$m, and 1.925 $\mu$m, respectively, at temperature $T = 25$°C. (D) Experimental results of the thermal emission spectra at various angles $\theta$ from the surface normal, and (E) angular emissivity at the peak $\lambda = 3.532$ $\mu$m (for the calculation $\lambda = 3.552$ $\mu$m), for $T = 900$°C and groove dimensions 3.52 $\mu$m (period), 0.18 $\mu$m (depth), and 1.76 $\mu$m (width). *From Han, S. E. (2009). Thermal emission control with periodic microstructures (Doctoral dissertation). University of Minnesota; Han, S. E., & Norris, D. J. (2010). Beaming thermal emission from hot metallic bull's eyes. Optics Express, 18(5), 4829–4837; Park, J. H., Han, S. E., Nagpal, P., & Norris, D. J. (2016). Observation of thermal beaming from tungsten and molybdenum bull's eyes. ACS Photonics, 3(3), 494–500.*

## 3. Surface-plasmonic impacts on optical beam coherence

Ever since the observation of an extraordinary strong light transmission through subwavelength hole arrays in metallic plates (Ebbesen, Lezec, Ghaemi, Thio, & Wolff, 1998), surface electromagnetic modes have been

used to manipulate and to control optical transmission via diverse nanostructures (Garcia-Vidal, Martin-Moreno, Ebbesen, & Kuipers, 2010). Coherence, especially, can be strongly modulated by surface waves at the apertures, with significant impacts on light transmission. For example, SPPs excited in a metallic double-slit configuration can either enhance or reduce the spatial coherence of a light beam traversing the interferometer (Divitt, Frimmer, Visser, & Novotny, 2016; Gan, Gbur, & Visser, 2007), having notable effects on the transmitted far-field behavior also when only one of the openings is illuminated (Kanseri, Kandpal, & Budhani, 2012; Kuzmin et al., 2007; Ravets et al., 2009). Engineering the SPP-induced modulations enables broad and continuous control of the spatial coherence of the output optical beam (Li & Pacifici, 2017), which consequently allows versatile tunability of the transmission in general. Besides modifying and controlling the statistical properties of optical beams, SPP interactions can be harnessed to measure subwavelength spatial coherence widths of light with even nanoscopic precision (Morrill, Li, & Pacifici, 2016). The control and determination of optical beam coherence via surface-wave resonances may thus be widely useful in high-resolution biomedical imaging, tomographic schemes, source characterization, and engineered nanophotonic elements with multifunctional capabilities.

In this section, we review how SPP interactions can be exploited to modulate, control, and measure spatial coherence of optical beams in the arguably most fundamental interferometric system, Young's double-slit configuration. We emphasize, however, that other SPP-based metallic structures, such as a three-slit interferometer (Gan & Gbur, 2008), dense arrays of nanoholes (Gan, Gu, Visser, & Gbur, 2012), subwavelength gratings (Saastamoinen & Lajunen, 2013), nanocylinders (Lindberg, Setälä, Kaivola, & Friberg, 2006), and even randomly rough interfaces (Leskova, Maradudin, & Munoz-Lopez, 2005), can be used to modify the spatial coherence of a beam. The coherence modulations in all these setups originate from SPP-mediated interference and encompass novel physical effects, including optical coherence resonances and optical coherence band gaps (Smith & Gbur, 2019), which are anticipated to be quite useful for plasmonic coherence-converting devices. As an alternative to SPPs supported by corrugated and lossy metal surfaces, photonic modes (Laroche et al., 2006) in planar waveguides coupled with dielectric metasurfaces (Liu et al., 2011) may also be utilized to achieve strong coherence modulation, with potential applications in light-transforming low-loss optical transmission elements.

## 3.1 Plasmon-modulated two-slit interference

Fig. 7 illustrates a plasmonic modification of Young's seminal double-slit interferometer, where a thin metal film deposited on glass and containing two identical slits is illuminated by TM-polarized light. For a suitable metal, angular frequency $\omega$, and slit separation $d$, SPPs are excited at the bottom (metal–glass) and top (metal–air) interfaces, which then travel between the openings and eventually scatter back into freely propagating radiation fields. The output field is thus composed not only of the directly transmitted fields from the slits, but also of the scattered radiation fields induced by the SPPs. Taking these contributions into account, and letting $E_{\mathrm{in}}(\mathbf{r}_1, \omega)$ and $E_{\mathrm{in}}(\mathbf{r}_2, \omega)$ denote spectral realizations of the time-stationary electric illumination fields at openings 1 and 2, respectively, the corresponding output radiation fields can be expressed as (Divitt et al., 2016; Gan et al., 2007)

$$E_{\mathrm{out}}(\mathbf{r}_1, \omega) = \tau(\omega)[E_{\mathrm{in}}(\mathbf{r}_1, \omega) + \beta(\omega)E_{\mathrm{in}}(\mathbf{r}_2, \omega)], \tag{8}$$

$$E_{\mathrm{out}}(\mathbf{r}_2, \omega) = \tau(\omega)[E_{\mathrm{in}}(\mathbf{r}_2, \omega) + \beta(\omega)E_{\mathrm{in}}(\mathbf{r}_1, \omega)], \tag{9}$$

with $\tau(\omega)$ being the slit transmission coefficient. Especially, the quantity

$$\beta(\omega) = \beta_{\mathrm{b}}(\omega)\mathrm{e}^{\mathrm{i}k_{\mathrm{b}}(\omega)d} + \beta_{\mathrm{t}}(\omega)\mathrm{e}^{\mathrm{i}k_{\mathrm{t}}(\omega)d}, \tag{10}$$

where $\beta_{\mathrm{b}}(\omega)$ and $\beta_{\mathrm{t}}(\omega)$ are the SPP-coupling coefficients at the bottom and top surfaces, respectively, and $k_{\mathrm{b}}(\omega)$ and $k_{\mathrm{t}}(\omega)$ are the associated (complex) SPP wave numbers, specifies the field transmission induced by SPP coupling. We note that the SPP field components perpendicular to the metal surfaces are omitted.

Equations (8)–(10) imply that when no SPPs are involved, i.e., $\beta_{\mathrm{b}}(\omega) = \beta_{\mathrm{t}}(\omega) = \beta(\omega) = 0$, the output field from a slit is directly proportional to the

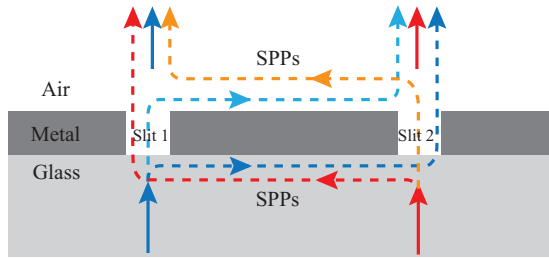


**Fig. 7** Plasmonic double-slit configuration. The incident light beam at each slit is split into three components: one part is directly transmitted, the other two parts generate SPPs at the bottom (metal–glass) and top (metal–air) interfaces. The excited SPPs travel to the other slit and scatter back into freely propagating radiation.

incident light impinging that slit. However, if SPPs are generated, the fields emanating from the slits may be *strongly modulated*, depending on $\omega$ and $d$, which subsequently affects the output spectral densities (spectra)

$$S_{\text{out}}(\mathbf{r}_1,\omega) = \langle |E_{\text{out}}(\mathbf{r}_1,\omega)|^2 \rangle, \quad S_{\text{out}}(\mathbf{r}_2,\omega) = \langle |E_{\text{out}}(\mathbf{r}_2,\omega)|^2 \rangle, \tag{11}$$

where the angle brackets stand for ensemble averaging. The SPP interactions may have a strong impact also on the output spatial correlations between the slits, which in the space–frequency domain are encoded in the *spectral electric correlation function* (Mandel & Wolf, 1995)

$$W_{\text{out}}(\mathbf{r}_1,\mathbf{r}_2,\omega) = \langle E^*_{\text{out}}(\mathbf{r}_1,\omega) E_{\text{out}}(\mathbf{r}_2,\omega) \rangle. \tag{12}$$

Rather surprisingly, by inspection of Eqs. (8)–(12) we conclude that even when only one of the two openings is illuminated, the output spectral density at the other slit and the output spectral electric correlation function between the slits are nonzero if SPPs are involved [$\beta(\omega) \neq 0$]: for example, although $E_{\text{in}}(\mathbf{r}_2, \omega) = 0$, one nonetheless has $S_{\text{out}}(\mathbf{r}_2, \omega) = |\tau(\omega)|^2 |\beta(\omega)|^2 \langle |E_{\text{in}}(\mathbf{r}_1, \omega)|^2 \rangle$ and $W_{\text{out}}(\mathbf{r}_1, \mathbf{r}_2, \omega) = |\tau(\omega)|^2 \beta(\omega) \langle |E_{\text{in}}(\mathbf{r}_1, \omega)|^2 \rangle$. In this kind of situation, the illuminated slit scatters the incident light and launches an SPP that travels towards the partner opening, where it is converted into free-space radiation and together with the directly transmitted component leads to an observable interference pattern in the far field (Kanseri et al., 2012; Kuzmin et al., 2007; Ravets et al., 2009).

Fig. 8 shows a numerical simulation of the SPP-modulated transmission under coherent double-slit illumination for a 200 nm thick Au film in air with 200 nm wide slits (Schouten et al., 2005). In Fig. 8A the angular-integrated transmission coefficient (i.e., transmission integrated over several interference orders) is displayed as a function of the incident light's wavelength for both TE-polarized and TM-polarized illumination. In the case of TE polarization, the transmission is small and weakly modulated because the induced surface excitations do not effectively couple to the other slit. For TM polarization, on the other hand, the transmission displays a strong modulation due to the *SPP-mediated interference*. Figs. 8B and C show the intensity distribution in close vicinity of the Au film for two different slit separations under TM-polarized illumination. For the slit separation $d = 5\lambda_{\text{SPP}}/2$, where $\lambda_{\text{SPP}}$ is the SPP wavelength, the transmission is maximum (Fig. 8B), while for $d = 4\lambda_{\text{SPP}}/2$ the transmission is minimum (Fig. 8C). In the former case, we can distinguish along the dark side of the film a well-developed,

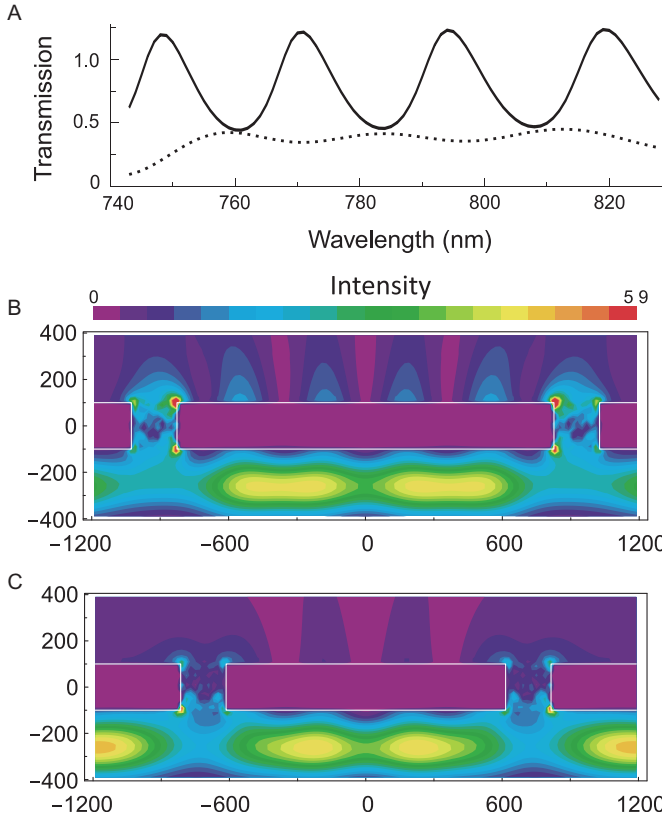


**Fig. 8** Simulation of SPP-modulated two-slit transmission under coherent illumination for a free-standing, 200 nm thick Au film with 200 nm wide slits. (A) Angular-integrated transmission coefficient as a function of the illumination wavelength for TM polarization (solid curve) and TE polarization (dotted curve) with the openings separated by 25 $\mu$m. (B) and (C) Intensity distribution in proximity of the film for TM-polarized illumination when the transmission is maximal and minimal, respectively, corresponding to slit separations $5\lambda_{SPP}/2$ and $4\lambda_{SPP}/2$, with $\lambda_{SPP}$ denoting the SPP wavelength. All lengths are in nm. *From Schouten, H. F., Kuzmin, N., Dubois, G., Visser, T. D., Gbur, G., Alkemade, P. F. A., …Eliel, E. R. (2005). Plasmon-assisted two-slit transmission: Young's experiment revisited. Physical Review Letters, 94(5), 053901.*

standing-wave pattern having six antinodes, two of which coincide with the openings themselves. In the latter situation, on the other hand, the antinodes of the pattern do not match with the slits. These results reflect the strong wavelength and slit-separation dependences of the SPP-modulated transmission.

## 3.2 Spatial correlation control

As discussed above, the SPPs can modulate the statistical characteristics of the output fields and thus the total transmission of the double-slit system. Accordingly, *controlling* the correlation properties of the radiation at the slits via SPP interactions yields access to manage the total optical transmission. In the space–frequency domain, the amount of spatial correlations among the stationary output fields can be quantified in terms of the *spectral degree of coherence* (Mandel & Wolf, 1995)

$$\mu_{\text{out}}(\mathbf{r}_1, \mathbf{r}_2, \omega) = \frac{W_{\text{out}}(\mathbf{r}_1, \mathbf{r}_2, \omega)}{\sqrt{S_{\text{out}}(\mathbf{r}_1, \omega) S_{\text{out}}(\mathbf{r}_2, \omega)}}. \tag{13}$$

Taking the input spectral densities equal, $\langle |E_{\text{in}}(\mathbf{r}_1, \omega)|^2 \rangle = \langle |E_{\text{in}}(\mathbf{r}_2, \omega)|^2 \rangle = S_{\text{in}}(\omega)$, Eqs. (8)–(13) result in (Divitt et al., 2016; Gan et al., 2007)

$$\mu_{\text{out}}(\mathbf{r}_1, \mathbf{r}_2, \omega) = \frac{\mu_{\text{in}}(\mathbf{r}_1, \mathbf{r}_2, \omega) + |\beta(\omega)|^2 \mu_{\text{in}}^*(\mathbf{r}_1, \mathbf{r}_2, \omega) + 2\text{Re}[\beta(\omega)]}{\sqrt{[1 + \alpha_1(\mathbf{r}_1, \mathbf{r}_2, \omega)][1 + \alpha_2(\mathbf{r}_1, \mathbf{r}_2, \omega)]}}, \tag{14}$$

where $\mu_{\text{in}}(\mathbf{r}_1, \mathbf{r}_2, \omega) = \langle E_{\text{in}}^*(\mathbf{r}_1, \omega) E_{\text{in}}(\mathbf{r}_2, \omega) \rangle / S_{\text{in}}(\omega)$ is the spectral degree of coherence of the input fields at the slits, and where we have introduced

$$\alpha_1(\mathbf{r}_1, \mathbf{r}_2, \omega) = |\beta(\omega)|^2 + 2\text{Re}[\beta(\omega) \mu_{\text{in}}(\mathbf{r}_1, \mathbf{r}_2, \omega)], \tag{15}$$

$$\alpha_2(\mathbf{r}_1, \mathbf{r}_2, \omega) = |\beta(\omega)|^2 + 2\text{Re}[\beta^*(\omega) \mu_{\text{in}}(\mathbf{r}_1, \mathbf{r}_2, \omega)]. \tag{16}$$

Three main conclusions can be drawn from Eq. (14). First, the *coherence modulation originates from the SPPs*: when no SPPs are present [$\beta(\omega) = 0$], $\mu_{\text{out}}(\mathbf{r}_1, \mathbf{r}_2, \omega) = \mu_{\text{in}}(\mathbf{r}_1, \mathbf{r}_2, \omega)$, indicating that the output degree of coherence is equal to the input degree of coherence. Second, if the illumination is fully coherent and in phase, the output radiation is totally coherent as well, viz., $\mu_{\text{out}}(\mathbf{r}_1, \mathbf{r}_2, \omega) = \mu_{\text{in}}(\mathbf{r}_1, \mathbf{r}_2, \omega) = 1$, so in this particular case the SPPs will not modify the coherence. Third, if the incident light field is incoherent, i.e., $\mu_{\text{in}}(\mathbf{r}_1, \mathbf{r}_2, \omega) = 0$, we obtain $\mu_{\text{out}}(\mathbf{r}_1, \mathbf{r}_2, \omega) = 2\text{Re}[\beta(\omega)]/[1 + |\beta(\omega)|^2]$, implying that not only can the coherence of the output radiation be *greater* than that of the incident field, but it may also *switch signs*, owing to SPP interactions, resulting in anticorrelated fields at the slits (Li & Pacifici, 2017).

The way the *slit separation* affects the SPP-modulated coherence can be studied by replacing the parallel slits with nonparallel slits (Divitt et al., 2016). Such a setup is shown in Fig. 9A, where the incident light from a spatially extended thermal source is spectrally filtered at 633 ± 5 nm wavelength and linearly polarized before it illuminates a 200 nm thick Au film

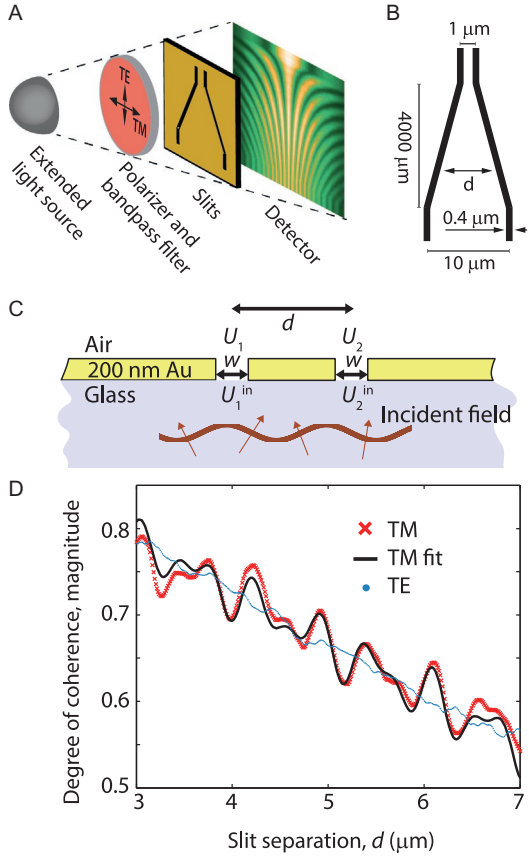


**Fig. 9** Experimental study of SPP-modulated coherence in a double-slit configuration. (A) Illustration of the experiment. Filtered and polarized light of wavelength $633 \pm 5$ nm from an extended thermal source passes via two nonparallel slits in a gold film and creates an interference pattern on a detector (shown in false color). Rotating the polarizer allows to control the SPP coupling on the metal film. (B) and (C) Schematic and cross-sectional diagrams of the double-slit setup. (D) Measured magnitude of the output spectral degree of coherence at the slits for TE-polarized (blue dots) and TM-polarized (red crosses) light as a function of the slit separation $d$. The theoretical fit (solid black curve) corresponds to Eq. (14), with the parameter values given in the text. *From Divitt, S., Frimmer, M., Visser, T. D., & Novotny, L. (2016). Modulation of optical spatial coherence by surface plasmon polaritons. Optics Letters, 41(13), 3094–3097.*

deposited on glass and with two nonparallel slits having a width of 400 nm. Figs. 9B and C provide schematic and cross-sectional diagrams, respectively, of the double-slit sample. The experimental data for the magnitude of the output spectral degree of coherence under both TE-polarized (blue dots) and TM-polarized (red crosses) illumination are displayed in Fig. 9D. The solid

curve in Fig. 9D is a theoretical result for TM polarization according to Eq. (14), with the SPP-coupling coefficients $\beta_b(\omega) = 0.026$ and $\beta_t(\omega) = 0.023$ being the only fitting parameters; the values for $k_b(\omega) = 1.65 \cdot 10^7 + i1.3 \cdot 10^5\ m^{-1}$ and $k_t(\omega) = 1.03 \cdot 10^7 + i3.3 \cdot 10^4\ m^{-1}$ are dictated by the materials, and a linear fit to the plotted TE curve was utilized for $\mu_{in}(\mathbf{r}_1, \mathbf{r}_2, \omega)$ (Divitt et al., 2016). For TE polarization no SPPs are excited and $\mu_{out}(\mathbf{r}_1, \mathbf{r}_2, \omega)$ decreases nearly linearly with $d$ in the given range, whereby the double-slit sample acts like a simple binary mask for measuring $\mu_{in}(\mathbf{r}_1, \mathbf{r}_2, \omega)$ produced by the bare source. In contrast, for TM-polarized light the output degree of coherence shows a strong modulation as a function of the slit separation, originating from SPP coupling at both the upper and lower interfaces of the Au layer.

Not only the *magnitude* but also the *phase* of the (complex-valued) degree of coherence can be modified via SPP coupling by varying the slit separation, allowing *full control* of the output radiation coherence (Li & Pacifici, 2017). In addition, besides the slit separation, the *operating frequency* (wavelength) may have a strong impact on the SPP-mediated interference and thus on the spatial correlation of the emanating light field from the openings. Fig. 10 shows measurements of the wavelength-resolved interference

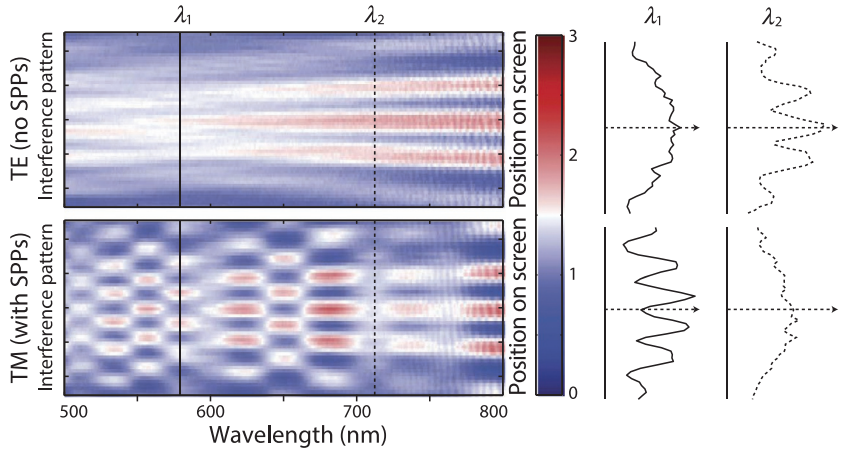


**Fig. 10** Measurements of wavelength-resolved interference patterns for broadband light exiting a 200 nm thick Ag film with two parallel slits under TE (top) and TM (bottom) polarized Köhler illumination. The slits are 200 nm wide, 15 $\mu$m long, and separated by 5 $\mu$m. Insets (right panels): conversion of incoherent light into partially coherent light at wavelength $\lambda_1 = 581$ nm (solid curves), and vice versa at $\lambda_2 = 712$ nm (dashed curves), as a result of strong SPP coupling for TM polarization. *From Li, D., & Pacifici, D. (2017). Strong amplitude and phase modulation of optical spatial coherence with surface plasmon polaritons. Science Advances, 3(10), e1700133.*

patterns induced by two parallel slits etched on a 200 nm thick Ag film and illuminated by linearly polarized broadband light under Köhler illumination (Li & Pacifici, 2017), with the openings being 200 nm wide, 15 $\mu$m long, and separated by 5 $\mu$m. The results show striking changes in the observed fringe visibility, and thus in the spatial coherence between the slits, under SPP coupling. For instance, whereas at wavelength $\lambda_1 = 581$ nm the field is virtually incoherent when no SPPs are present (TE polarization), the field turns *partially coherent* under SPP excitation (TM polarization) as evidenced by enhanced fringe visibility. Vice versa, the decreased fringe contrast at $\lambda_2 = 712$ nm for TM polarization with respect to TE polarization is a manifestation of the strong *SPP-induced reduction* of spatial correlations between the slits, rendering the output field effectively incoherent.

## 3.3 Nanoscale coherence width measurement

Not only does the SPP-mediated interference modulate spatial correlations of the propagating light beam, but it also provides novel means for *measuring nanoscale coherence widths* of optical fields (Morrill et al., 2016). Such a measurement can be performed by using a modified double-slit setup, as illustrated in Fig. 11, in which one of the two openings is replaced with a subwavelength groove that converts a fraction of the incident light into SPPs propagating towards the neighboring slit. The interference of the scattered SPPs and the incident field at the opening results in a measurable change in the light intensity transmitted through the slit, from which the spatial coherence width of the input optical beam can be determined (Morrill et al., 2016). A similar arrangement can be employed to achieve

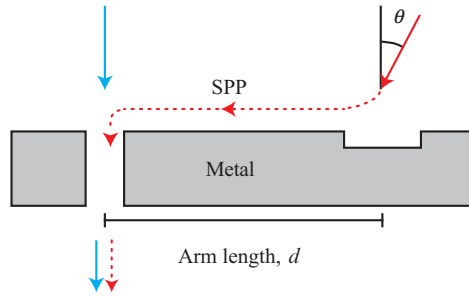


**Fig. 11** Schematic of a slit-groove setup for measuring nanoscale coherence widths of optical fields. The light impinging the metal groove at an angle of incidence $\theta$ excites SPPs that after propagation interfere with the light at the slit. Measuring the SPP-modulated transmission through the opening allows to extract information about the spatial coherence width of the incident optical field.

full dynamical control of optical transmission through a nanoscopic slit by varying the incident beam's phase relative to that of the generated SPPs at a nearby grating (Daniel et al., 2015).

In more precise terms, when the metallic slit-groove system is illuminated, the part of the light incident on the groove, $E_{\text{in}}(\mathbf{r}_{\text{G}}, \omega)$, is partially scattered into an SPP, with the SPP-coupling efficiency determined by the (complex-valued) groove scattering coefficient $\beta_{\text{G}}(\omega)$. After propagating the distance $d$ between the groove and the slit, the SPP has attenuated as dictated by the imaginary part of the SPP wave number, $k''_{\text{SPP}}(\omega)$, and it has also acquired the additional phase (Morrill et al., 2016)

$$\psi(\omega) = k'_{\text{SPP}}(\omega)d - k(\omega)\sin\theta\ d + \phi(\omega), \tag{17}$$

where $k'_{\text{SPP}}(\omega)$ is the real part of the SPP wave number, $k(\omega)$ is the free-space wave number, $\theta$ is the angle of incidence respective to the screen normal, and $\phi(\omega)$ is the phase resulting from scattering events at the groove and the slit. Eventually the SPP interferes with the electric component $E_{\text{in}}(\mathbf{r}_{\text{S}}, \omega)$ incident on the slit, resulting in the output spectral density

$$\begin{aligned} S_{\text{out}}(\mathbf{r}_{\text{S}}, \omega) \propto\ & S_{\text{in}}(\mathbf{r}_{\text{S}}, \omega) + |\beta_{\text{G}}(\omega)|^2 S_{\text{in}}(\mathbf{r}_{\text{G}}, \omega) \mathrm{e}^{-2k''_{\text{SPP}}(\omega)d} \\ & + 2|\beta_{\text{G}}(\omega)| \sqrt{S_{\text{in}}(\mathbf{r}_{\text{S}}, \omega) S_{\text{in}}(\mathbf{r}_{\text{G}}, \omega)}\ \mathrm{e}^{-k''_{\text{SPP}}(\omega)d} \\ & \times |\mu_{\text{in}}(\mathbf{r}_{\text{S}}, \mathbf{r}_{\text{G}}, \omega)| \cos\{\psi(\omega) + \arg[\mu_{\text{in}}(\mathbf{r}_{\text{S}}, \mathbf{r}_{\text{G}}, \omega)]\}, \end{aligned} \tag{18}$$

including the spectral densities $S_{\text{in}}(\mathbf{r}_{\text{S}}, \omega) = \langle |E_{\text{in}}(\mathbf{r}_{\text{S}}, \omega)|^2 \rangle$ and $S_{\text{in}}(\mathbf{r}_{\text{G}}, \omega) = \langle |E_{\text{in}}(\mathbf{r}_{\text{G}}, \omega)|^2 \rangle$ of the input fields, and the input spectral degree of coherence

$$\mu_{\text{in}}(\mathbf{r}_{\text{S}}, \mathbf{r}_{\text{G}}, \omega) = \frac{\langle E^*_{\text{in}}(\mathbf{r}_{\text{S}}, \omega) E_{\text{in}}(\mathbf{r}_{\text{G}}, \omega) \rangle}{\sqrt{S_{\text{in}}(\mathbf{r}_{\text{S}}, \omega) S_{\text{in}}(\mathbf{r}_{\text{G}}, \omega)}}. \tag{19}$$

We note that Eq. (18) is an approximation that considers only first-order interference effects; a more accurate model involves higher-order terms arising from multiple SPP pathways between the slit and the groove (Morrill et al., 2016).

The magnitude of the input degree of coherence in Eq. (19) is obtained by measuring the SPP-modulated visibility $V(\omega)$ of the output field when $S_{\text{in}}(\mathbf{r}_{\text{S}}, \omega) = S_{\text{in}}(\mathbf{r}_{\text{G}}, \omega)$ (Morrill et al., 2016). The associated *spatial coherence width* $L_{\text{C}}(\omega)$ is then considered as the slit-groove separation over which the fringe visibility drops from $V(\omega) = 1$ to $V(\omega) = 0.88$ (Morrill et al., 2016). Fig. 12 shows coherence width measurements for light of varying degree of coherence incident on a 300 nm thick Ag layer deposited on glass. The slit is 100 nm wide and 15 $\mu$m long, paralleled by an equally long groove with a

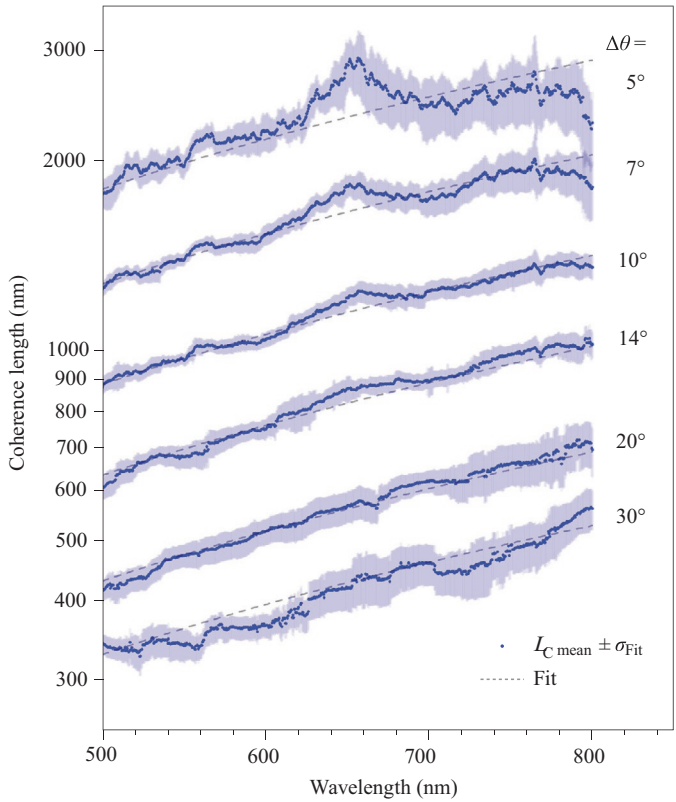


**Fig. 12** Coherence width measurements as a function of wavelength for light of varying degree of spatial coherence incident on a slit-groove system (see Fig. 11) composed of Ag. The slit etched on the 300 nm thick Ag layer is 100 nm wide and 15 $\mu$m long, whereas the equally long groove paralleling the slit is 200 nm wide and 20 nm deep. The subtended angle $\Delta\theta$ of the incident light is adjusted by a condenser aperture in Köhler illumination, with increasing $\Delta\theta$ reducing the spatial coherence. The blue bands show a 95% confidence interval, determined by statistical and error analyses, while the dashed lines are theoretical fits indicating the general coherence width behavior. *From Morrill, D., Li, D., & Pacifici, D. (2016). Measuring subwavelength spatial coherence with plasmonic interferometry. Nature Photonics, 10(10), 681–687.*

width of 200 nm and depth of 20 nm. The spatial coherence of the incident beam is varied by adjusting a condenser aperture under Köhler illumination, such that increasing the subtended angle $\Delta\theta$ reduces the coherence (Morrill et al., 2016). We find from Fig. 12 that for larger apertures, and thus lower degrees of spatial coherence, *subwavelength coherence widths* are possible; especially, for $\Delta\theta = 30°$ we have $L_C(\omega) = 330$ nm at wavelength $\lambda = 500$ nm. In addition, the remarkable spectral resolution ($\sim 0.4$ nm) in

Fig. 12 owing to SPP interactions provides unforeseen precision into the very fine structure of spatial coherence of light, thereby establishing plasmonic interferometry as a unique metrological platform to probe optical coherence at the nanoscale.

## 4. Partially coherent evanescent wave fields

Optical evanescent waves are a special type of electromagnetic surface waves, formed when a light field undergoes total internal reflection at a dielectric boundary (de Fornel, 2001). When interacting with matter, evanescent waves enable a phenomenon analogous to quantum mechanical tunneling through a potential barrier (de Fornel, 2001; Novotny & Hecht, 2012). They also allow to study biological samples with a resolution well beyond the classical diffraction limit (Axelrod, 2001; Sako, Minoghchi, & Yanagida, 2000; Schneckenburger, 2005) and play an important role in surface-polariton excitation (Maier, 2007; Maradudin, Sambles, & Barnes, 2014). In addition, evanescent waves are associated with some remarkable physical properties, such as extraordinary transverse spin angular momentum (Aiello & Banzer, 2016; Aiello, Banzer, Neugebauer, & Leuchs, 2015; Bliokh, Bekshaev, & Nori, 2014; Bliokh & Nori, 2015) and spin-momentum locking (Bliokh, Rodríguez-Fortuño, Nori, & Zayats, 2015; Van Mechelen & Jacob, 2016), intimately related to the quantum spin Hall effect of light (Bliokh, Smirnova, & Nori, 2015), as well as nonconservation of helicity under relativistic Lorentz boosts (Bliokh, 2018). Evanescent waves have thus a pivotal position in nanophotonics and for the understanding of several optical phenomena that are confined to subwavelength dimensions.

To date, however, most studies concerning evanescent waves have dealt with monochromatic and therefore completely coherent and polarized fields. Partially coherent and partially polarized evanescent wave fields have gained attention only recently, and they differ from their deterministic (monochromatic) counterparts in several fundamental physical aspects, with potential applications in near-field probing, optical tweezing, nanoparticle excitation, among other surface electromagnetic light–matter interactions. For example, while the polarization ellipse of a monochromatic evanescent wave is always restricted to a fixed plane in space, the electric field of a partially polarized evanescent wave fluctuates in three orthogonal spatial directions in any reference frame (Norrman, Friberg, Gil, & Setälä, 2017). A partially polarized evanescent wave is also in a so-called nonregular polarization state (Norrman, Gil, Friberg, & Setälä, 2019), constituting a rich and

significant family of genuine three-component light fields that cannot be characterized with the traditional polarization formalism for beam-like fields (Gil, Friberg, Setälä, & San José, 2017; Gil, Norrman, Friberg, & Setälä, 2018a). Furthermore, random evanescent fields may exhibit subwavelength surface coherence lengths and their degree of polarization can change notably when moving only a fraction of a wavelength away from the supporting interface (Norrman, Setälä, & Friberg, 2011). Generation and electromagnetic coherence of completely unpolarized three-component evanescent fields in multibeam illumination have also been explored, revealing the possibility to tailor evanescent fields sharing polarization properties identical to those of universal blackbody radiation, yet with tunable coherence states (Norrman, Setälä, & Friberg, 2015a).

In this section, after recalling the monochromatic evanescent wave in total internal reflection, we review the recent discoveries and progress regarding the subwavelength coherence structure and three-dimensional polarization of such random evanescent wave fields.

## 4.1 Evanescent wave in total internal reflection

Fig. 13 illustrates a monochromatic light beam, represented as a homogeneous electromagnetic plane-wave field, generating an optical evanescent wave via total internal reflection at a planar interface ($z = 0$) between two uniform dielectric media. Both medium 1 ($z < 0$) and medium 2 ($z > 0$), having ($\omega$-dependent) refractive indices $n_1$ and $n_2$, respectively, are lossless. The incoming wave, generally carrying both an $s$-polarized and a $p$-polarized

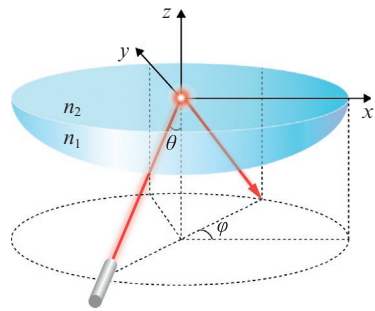


**Fig. 13** Evanescent wave excitation via total internal reflection at a planar interface ($z = 0$) between two lossless dielectric media having refractive indices $n_1$ ($z < 0$) and $n_2$ ($z > 0$). The incident beam impinges the surface with an azimuthal angle $\varphi$ at the angle of incidence $\theta$.

component, hits the surface at an azimuthal angle $0 \leq \varphi < 2\pi$ (with respect to the $x$ axis) and at an angle of incidence $\theta_c < \theta < \pi/2$, where $\theta_c = \arcsin \tilde{n}^{-1}$ is the critical angle with $\tilde{n} = n_1/n_2 > 1$. Under these conditions, the spatial part of the electric field for the evanescent wave takes the form

$$\mathbf{E}(\mathbf{r}, \omega) = (t_s E_s \hat{\mathbf{s}} + t_p E_p \hat{\mathbf{p}}) \mathrm{e}^{\mathrm{i}\mathbf{k}\cdot\mathbf{r}}, \tag{20}$$

where $E_s$ and $E_p$ are the ($\omega$-dependent) complex field amplitudes of the $s$- and $p$-polarized parts of the incident wave in medium 1. The Fresnel transmission coefficients $t_s$ and $t_p$ are given by (Norrman et al., 2011)

$$t_s = \frac{2\cos\theta}{\cos\theta + \mathrm{i}\gamma}, \quad t_p = \frac{2\tilde{n}^2\cos\theta\chi}{\cos\theta + \mathrm{i}\tilde{n}^2\gamma}, \tag{21}$$

including the ($\omega$-dependent) quantities

$$\gamma = \tilde{n}^{-1}\sqrt{\tilde{n}^2\sin^2\theta - 1}, \quad \chi = \sqrt{\sin^2\theta + \gamma^2}, \tag{22}$$

where the former may be interpreted as the decay constant of the evanescent wave. Furthermore, in Cartesian coordinates, the wave vector $\mathbf{k}$ and the unit polarization vectors $\hat{\mathbf{s}}$ and $\hat{\mathbf{p}}$ of the evanescent wave read (Norrman et al., 2015a)

$$\mathbf{k} = k_1 \begin{pmatrix} \sin\theta\cos\varphi \\ \sin\theta\sin\varphi \\ \mathrm{i}\gamma \end{pmatrix}, \quad \hat{\mathbf{s}} = \begin{pmatrix} -\sin\varphi \\ \cos\varphi \\ 0 \end{pmatrix}, \quad \hat{\mathbf{p}} = \frac{1}{\chi}\begin{pmatrix} -\mathrm{i}\gamma\cos\varphi \\ -\mathrm{i}\gamma\sin\varphi \\ \sin\theta \end{pmatrix}, \tag{23}$$

with $k_1$ being the ($\omega$-dependent) wave number in medium 1.

We emphasize that the polarization vectors in Eq. (23) are constructed as $\hat{\mathbf{p}} = \hat{\mathbf{k}} \times \hat{\mathbf{s}}$, with especially $\hat{\mathbf{k}} = \mathbf{k}/|\mathbf{k}|$ where $|\mathbf{k}|$ is the wave-vector magnitude, whereupon $\{\hat{\mathbf{k}}, \hat{\mathbf{s}}, \hat{\mathbf{p}}\}$ forms a right-handed and unit-normalized vector triad (Norrman et al., 2011). Owing to this construction, the Fresnel transmission coefficient $t_p$ in Eq. (21) differs from the conventional expression (de Fornel, 2001; Novotny & Hecht, 2012). The difference stems from the wave-vector normalization: instead of the magnitude $|\mathbf{k}|$, it is customary to normalize $\mathbf{k}$ of the evanescent wave with respect to the wave number $k_2$ in medium 2 (de Fornel, 2001; Novotny & Hecht, 2012). Such a choice, however, does not yield a $\hat{\mathbf{k}}$ of unit magnitude because $|\mathbf{k}| = k_1\chi \neq k_2$ according to Eqs. (22) and (23). The virtue of the normalization $\hat{\mathbf{k}} = \mathbf{k}/|\mathbf{k}|$, not only for evanescent waves but for general electromagnetic surface waves including absorptive media (Norrman, 2016), is that it always preserves the physical

meaning of the transmission coefficient as being the ratio between the complex field amplitudes on the two opposite sides of the interface. If $\mathbf{k}$ is normalized with respect to the wave number, this is only true for purely propagating waves in lossless media having real-valued wave vectors.

Another fundamental feature concerning Eq. (23) is that the polarization vectors can be expressed solely in terms of the wave vector, i.e.,

$$\hat{\mathbf{s}} = \mathrm{i}\frac{\mathbf{k}^* \times \mathbf{k}}{|\mathbf{k}^* \times \mathbf{k}|}, \qquad \hat{\mathbf{p}} = \mathrm{i}\hat{\mathbf{k}} \times \frac{\mathbf{k}^* \times \mathbf{k}}{|\mathbf{k}^* \times \mathbf{k}|}. \tag{24}$$

This property is known as spin-momentum locking (Van Mechelen & Jacob, 2016) or spin-direction locking (Bliokh, Rodríguez-Fortuño, et al., 2015) of the evanescent wave, viz., the wave vector fundamentally locks the polarization (spin) of the field. The locking in Eq. (24) is totally coordinate independent and actually covers any electromagnetic surface wave (also in lossy media) with a wave vector $\mathbf{k} = k_{\parallel}\hat{\mathbf{e}}_{\parallel} + k_{\perp}\hat{\mathbf{e}}_{\perp}$, where $k_{\parallel}$ and $k_{\perp}$ are complex numbers while $\hat{\mathbf{e}}_{\parallel}$ and $\hat{\mathbf{e}}_{\perp}$ are real-valued unit vectors lying parallel and perpendicular to the surface, respectively, such that the triad $\{\hat{\mathbf{k}}, \hat{\mathbf{s}}, \hat{\mathbf{p}}\}$ is right-handed, unit-normalized, and satisfies $\hat{\mathbf{k}} \cdot \hat{\mathbf{s}} = \hat{\mathbf{k}} \cdot \hat{\mathbf{p}} = 0$ as required by Maxwell's equations (Norrman, 2016). Consequently, the vectors $\hat{\mathbf{k}}$ and $\hat{\mathbf{p}}$ are generally not mutually orthogonal when the wave vector is complex-valued, as for an evanescent wave in *p*-polarized excitation which is elliptically polarized in the plane of incidence (Józefowski, Fiutowski, Kawalec, & Rubahn, 2007; Kawalec, Józefowski, Fiutowski, Kasprowicz, & Dohnalik, 2007).

## 4.2 Degrees of coherence and polarization

Taking $\mathbf{E}(\mathbf{r}, \omega)$ in Eq. (20) as a field realization, the spectral coherence matrix [Eq. (2)] characterizing all the second-order statistical properties of a *random*, stationary evanescent wave is expressible as

$$\mathbf{W}(\mathbf{r}_1, \mathbf{r}_2, \omega) = \mathbf{W}_0 \mathrm{e}^{\mathrm{i}k_1 \sin\theta(\cos\varphi\Delta x + \sin\varphi\Delta y)} \mathrm{e}^{-k_1\gamma(z_1+z_2)}, \tag{25}$$

including $\Delta x = x_2 - x_1$, $\Delta y = y_2 - y_1$, and the Hermitian matrix

$$\mathbf{W}_0 = w_s\hat{\mathbf{s}}^*\hat{\mathbf{s}}^{\mathrm{T}} + w_p\hat{\mathbf{p}}^*\hat{\mathbf{p}}^{\mathrm{T}} + |\mu|\sqrt{w_s w_p}(\mathrm{e}^{\mathrm{i}\varphi}\hat{\mathbf{s}}^*\hat{\mathbf{p}}^{\mathrm{T}} + \mathrm{e}^{-\mathrm{i}\varphi}\hat{\mathbf{p}}^*\hat{\mathbf{s}}^{\mathrm{T}}), \tag{26}$$

with $w_s = |t_s|^2\langle|E_s|^2\rangle$ and $w_p = |t_p|^2\langle|E_p|^2\rangle$ being proportional to the energy densities of the *s*- and *p*-polarized components, respectively, of the evanescent wave at the surface ($z = 0$). Moreover, $\mu = \langle E_s^* E_p\rangle / (\langle|E_s|^2\rangle\langle|E_p|^2\rangle)^{1/2}$

is the spectral correlation coefficient between the *s*- and *p*-polarized parts of the incident excitation light beam, and $\varphi = \arg(\mu) - \arg(t_s) + \arg(t_p)$ is a phase. The associated spectral polarization matrix [Eq. (6)] reads

$$\mathbf{\Phi}(\mathbf{r}, \omega) = \mathbf{W}_0 \mathrm{e}^{-2k_1 \gamma z}, \tag{27}$$

which spatially depends only on the height $z$.

While the (three-dimensional) polarization characteristics of the random evanescent wave can be quantified further by the degree of polarimetric purity given in Eq. (7), its coherence properties can be assessed quantitatively by the *electromagnetic degree of coherence* (Setälä, Tervo, & Friberg, 2004)

$$\mu_{\mathrm{EM}}(\mathbf{r}_1, \mathbf{r}_2, \omega) = \frac{\| \mathbf{W}(\mathbf{r}_1, \mathbf{r}_2, \omega) \|_{\mathrm{F}}}{\sqrt{S(\mathbf{r}_1, \omega) S(\mathbf{r}_2, \omega)}}, \tag{28}$$

where $\| \cdots \|_{\mathrm{F}}$ refers to the Frobenius matrix norm and $S(\mathbf{r}, \omega) = \mathrm{tr}\mathbf{W}(\mathbf{r}, \mathbf{r}, \omega)$ is the spectral density, as before. An analogous quantity can be used in the space–time domain (Tervo, Setälä, & Friberg, 2003). The degree of coherence in Eq. (28) includes every element of the coherence matrix and is thereby a measure of the spectral correlations among all the orthogonal components of the electric field at two points. It satisfies $0 \leq \mu_{\mathrm{EM}}(\mathbf{r}_1, \mathbf{r}_2, \omega) \leq 1$ and remains invariant under local unitary transformations. The upper bound corresponds uniquely to the situation in which all the electric field components are fully correlated, while the lower bound stands for the case where no correlations (coherence) exist between any of the components. For beam-like fields, the electromagnetic degree of coherence characterizes the modulation of the four Stokes parameters in Young's interference experiment, i.e., not merely the intensity variation but also the polarization-state modulation (Leppänen, Saastamoinen, Friberg, & Setälä, 2014; Setälä, Tervo, & Friberg, 2006a), and is thus a generalization of the traditional degree of coherence for scalar-light fields (which exclusively involves the visibility of intensity fringes). Likewise, its recently introduced quantum counterpart (Norrman, Blomstedt, Setälä, & Friberg, 2017), as also the degree of polarization for quantum light beams (Norrman, Friberg, & Leuchs, 2020), is fundamentally connected to complementarity and wave-particle duality of genuine vector-light fields in photon interference.

For a stationary evanescent wave, the electromagnetic degree of coherence in Eq. (28) takes the form (Norrman et al., 2011)

$$\mu_{\mathrm{EM}}(\mathbf{r}_1, \mathbf{r}_2, \omega) = \mu_{\mathrm{EM}}(\omega) = \sqrt{1 - \frac{2(1 - |\mu|^2) w_s w_p}{(w_s + w_p)^2}}, \tag{29}$$

and in a similar fashion the degree of polarimetric purity given by Eq. (7) reads (Norrman et al., 2011)

$$P_{3D}(\mathbf{r},\omega) = P_{3D}(\omega) = \sqrt{1 - \frac{3(1-|\mu|^2)w_s w_p}{(w_s + w_p)^2}}. \tag{30}$$

The maximum values $\mu_{EM}(\omega) = P_{3D}(\omega) = 1$, representing a totally coherent and polarized evanescent wave, are saturated only when the excitation beam is polarized, i.e., $\langle|E_s|^2\rangle = 0$, $\langle|E_p|^2\rangle = 0$, or $|\mu| = 1$. For all other cases the evanescent wave is partially coherent and partially polarized with $\mu_{EM}(\omega) < 1$ and $P_{3D}(\omega) < 1$. The lower bounds $\mu_{EM}(\omega) = 1/\sqrt{2}$ and $P_{3D}(\omega) = 1/2$ are met exclusively if $\langle|E_s|^2\rangle/\langle|E_p|^2\rangle = |t_p|^2/|t_s|^2$ and $|\mu| = 0$, a situation in which the evanescent wave attains its highest degree of *polarimetric nonregularity* (Norrman et al., 2019). The concept of polarimetric nonregularity (Gil et al., 2017, 2018a) is discussed in detail in Section 4.4. Furthermore, the lower limit $P_{3D}(\omega) = 1/2$ for the evanescent wave is a specific manifestation of a more general result, stating that light created by an optical system out of a single, arbitrary polarized beam obeys $P_{3D}(\mathbf{r},\omega) \geq 1/2$ (Setälä, Lindfors, & Friberg, 2009).

Contrary to a single evanescent wave, a superposition of evanescent waves can form a random near field that exhibits subwavelength spatial variations in the degrees of coherence and polarization. For example, evanescent fields at high refractive-index-contrast interfaces may show coherence lengths much smaller than the light's wavelength (Norrman et al., 2011). The coherence lengths are typically smallest in the immediate vicinity of the surface, but can get very large already within a wavelength of it. Unlike for the thermal near fields (Section 2.2), the subwavelength coherence lengths of evanescent fields are not a consequence of absorption because the involved media are lossless. Likewise, evanescent fields can display variations in the degree of polarization at subwavelength scales and they can also exhibit polarization states for which $P_{3D}(\mathbf{r},\omega) < 1/2$ (Norrman et al., 2011), a regime not accessible for ordinary beam-like fields (Setälä, Shevchenko, et al., 2002). Already two partially polarized beams sharing the same plane of incidence are sufficient for the excitation of an evanescent field having $P_{3D}(\mathbf{r},\omega) < 1/2$, and allowing the incident beams to have different planes of incidence can even lead to $P_{3D}(\mathbf{r},\omega) \approx 0$ (Norrman et al., 2015a), a result that has been confirmed to be valid in the space–time domain too (Hassinen, Popov, Friberg, & Setälä, 2016).

A light field with $P_{3D}(\mathbf{r}, \omega) = 0$ is regarded completely unpolarized in the full three-dimensional sense: its polarization ellipse evolves totally randomly in the whole three-dimensional space and it unambiguously corresponds to a polarization matrix which is proportional to the $3 \times 3$ identity matrix. Recently the generation and spectral electromagnetic coherence of stationary, fully unpolarized three-component evanescent fields involving a multibeam illumination configuration were explored (Norrman et al., 2015a). Fig. 14 illustrates the spatial behavior of the spectral electromagnetic degree

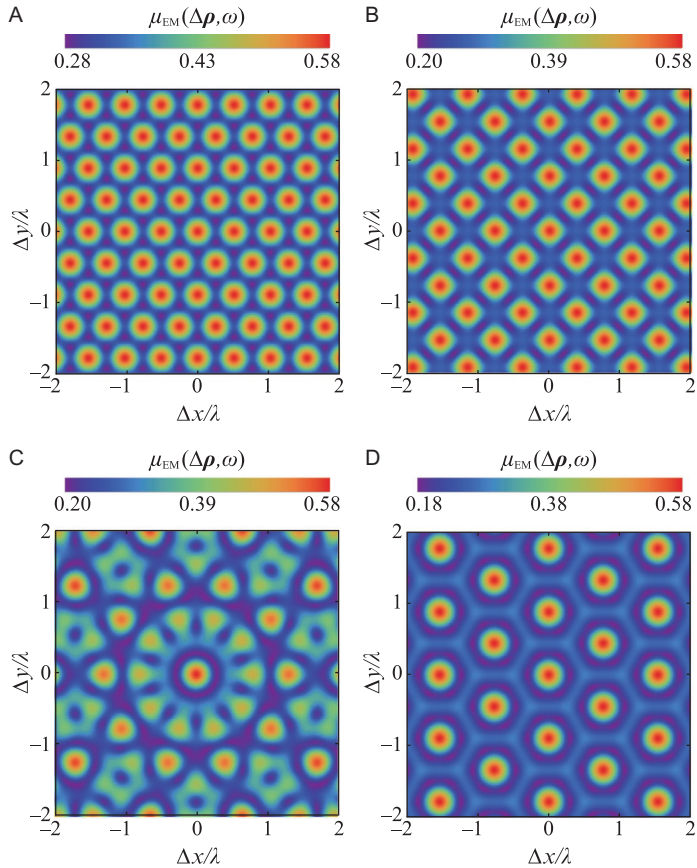


**Fig. 14** Spatial behavior of the spectral electromagnetic coherence $\mu_{EM}(\Delta\boldsymbol{\rho}, \omega)$ for an unpolarized three-component evanescent field above a $SiO_2$/air interface excited by (A) $N = 3$, (B) $N = 4$, (C) $N = 5$, and (D) $N = 6$ uniformly distributed and uncorrelated incident beams with the same angle of incidence $\theta = \pi/3$. The refractive indices are $n_1 = 1.5$ and $n_2 = 1$, and $\lambda$ is the free-space wavelength. *From Norrman, A. (2016). Electromagnetic coherence of optical surface and quantum light fields (Doctoral dissertation). University of Eastern Finland.*

of coherence for such an unpolarized evanescent field at a $SiO_2$/air interface, created by different numbers of uniformly distributed excitation beams sharing the same angle of incidence $\theta = \pi/3$. The beams are independent and have uncorrelated *s*- and *p*-polarized parts, with the respective intensity ratio $\langle|E_s|^2\rangle/\langle|E_p|^2\rangle$ specifically fixed (Norrman et al., 2015a). Owing to these conditions $\mu_{\mathrm{EM}}(\mathbf{r}_1, \mathbf{r}_2, \omega) = \mu_{\mathrm{EM}}(\Delta\boldsymbol{\rho}, \omega)$, where $\Delta\boldsymbol{\rho} = \Delta x\hat{\mathbf{e}}_x + \Delta y\hat{\mathbf{e}}_y$ with $\hat{\mathbf{e}}_x$ and $\hat{\mathbf{e}}_y$ being the unit vectors in the $x$ and $y$ directions, respectively. One observes that the degree of coherence can vary considerably, exhibiting diverse subwavelength lattice-like structures depending on the used modality. This reveals the feasibility to tailor evanescent fields possessing polarization qualities identical to those of universal blackbody radiation, yet with tunable spatial coherence characteristics.

## 4.3 Polarimetric dimension

Polarization of light (Brosseau, 1998; Gil & Ossikovski, 2016) is determined by the orientation of the electric field vector. In a specific coordinate system, the electric part of random light may fluctuate in three orthogonal spatial directions, but by changing the frame of reference it may turn out that the field vector actually is restricted to a plane, or even that it vibrates in just a single direction. Optical fields can hence be classified into one-dimensional (1D), two-dimensional (2D), or three-dimensional (3D) light, depending on the minimum number of orthogonal coordinate axes needed to describe them. The dimensional nature of light becomes especially important when addressing polarization characteristics of complex-structured light, electromagnetic near fields, and tightly focused optical beams.

Let $\mathbf{R}$ be the $3 \times 3$ polarization matrix either in the space–time domain or in the space–frequency domain. The dimensionality of light is formally defined by the eigenvalues $a_1 \geq a_2 \geq a_3 \geq 0$ of the real part $\mathbf{R}'$ of the full complex polarization matrix $\mathbf{R}$ as (Norrman, Friberg, et al., 2017)

$$\text{1D light:} \quad a_1 > 0,\ a_2 = 0,\ a_3 = 0; \tag{31}$$

$$\text{2D light:} \quad a_1 > 0,\ a_2 > 0,\ a_3 = 0; \tag{32}$$

$$\text{3D light:} \quad a_1 > 0,\ a_2 > 0,\ a_3 > 0. \tag{33}$$

The eigenvalues of $\mathbf{R}'$, constituting the total intensity $I = a_1 + a_2 + a_3$ of the whole state $\mathbf{R}$, are referred to as *principal intensities* and they are introduced via the so-called *intrinsic coordinate frame* in which $\mathbf{R}'$ is a diagonal matrix (Dennis, 2004; Gil, 2014, 2015). Physically, for 1D light the electric field vibrates in only one direction, viz., the light is linearly polarized, for 2D light

the electric field is restricted to a fixed plane, and for 3D light the electric field fluctuates in three orthogonal spatial directions in any reference frame. Furthermore, for intensity-isotropic 2D light $a_1 = a_2$ and $a_3 = 0$, while for intensity-isotropic 3D light $a_1 = a_2 = a_3$. It is important to understand that the number of nonnegative eigenvalues of the full complex polarization matrix $\mathbf{R}$ does not necessarily provide information about the physical dimension of the light field. For example, the full polarization matrix of a circularly polarized light beam involves just a single nonzero eigenvalue, whereas its real part satisfies $a_1 = a_2$ and $a_3 = 0$, hence corresponding to (intensity-isotropic) 2D light in view of Eq. (32).

To characterize the dimensionality of a light field more quantitatively, one may use the *polarimetric dimension* (Norrman, Friberg, et al., 2017)

$$D = 3 - 2d, \tag{34}$$

where $d$ is the *dimensionality index*, or the *degree of intensity anisotropy*, of the polarization state $\mathbf{R}$ (Gil et al., 2019):

$$d = \sqrt{\frac{3}{2}\left(\frac{\mathrm{tr}\mathbf{R}'^2}{\mathrm{tr}^2\mathbf{R}'} - \frac{1}{3}\right)}. \tag{35}$$

Especially, the quantity $d$ is the distance between the real-valued matrix $\mathbf{R}'$ and the $3 \times 3$ identity matrix corresponding to intensity-isotropic 3D light, with the scaling chosen so that $0 \leq d \leq 1$. The polarimetric dimension is thus a real number that obeys $1 \leq D \leq 3$ and remains invariant under orthogonal transformations. It should not be identified as such with the actual physical dimension of the light [specified by Eqs. (31)–(33)], but as an effective dimension describing the intensity-distribution spread.

The physical meaning of $D$ becomes more clear by writing Eq. (34) in terms of the eigenvalues of $\mathbf{R}'$, viz.,

$$D = 3 - \frac{\sqrt{2\left[(a_1 - a_2)^2 + (a_1 - a_3)^2 + (a_2 - a_3)^2\right]}}{a_1 + a_2 + a_3}. \tag{36}$$

The minimum $D = 1$ is encountered only for 1D light ($a_2 = a_3 = 0$), while the maximum $D = 3$ is saturated exclusively for intensity-isotropic 3D light ($a_1 = a_2 = a_3$). For 2D light ($a_3 = 0$, $a_2 > 0$) necessarily $1 < D \leq 2$, with the upper limit $D = 2$ taking place for intensity-isotropic 2D light ($a_1 = a_2$). Values in the domain $D > 2$ are thereby clear signatures of a 3D light field (3D light can nevertheless assume any value within the interval $1 < D \leq 3$).

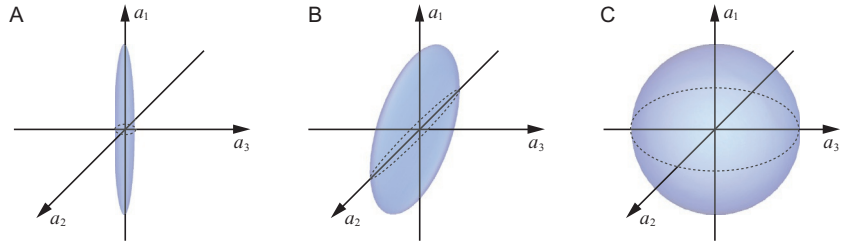


**Fig. 15** Examples of principal-intensity distributions for 3D light fields with polarimetric dimension (A) $D \approx 1$, (B) $D \approx 2$, and (C) $D \approx 3$. *From Norrman, A., Friberg, A. T., Gil, J. J., & Setälä, T. (2017). Dimensionality of random light fields. Journal of the European Optical Society-Rapid Publications, 13, 36.*

Fig. 15 provides a schematic illustration for the polarimetric dimension, depicting principal-intensity distributions for three different 3D light fields. In Fig. 15A $a_1$ is significantly larger than $a_2$ and $a_3$, rendering the light virtually one dimensional with $D \approx 1$. In Fig. 15B $a_1 \approx a_2 \gg a_3$, whereupon the light field is effectively 2D intensity-isotropic having $D \approx 2$. In Fig. 15C $a_1 \approx a_2 \approx a_3$, corresponding to intensity-isotropic 3D light with $D \approx 3$.

In the case of stationary evanescent waves in the spectral domain, whenever the excitation beam is partially polarized, i.e., $\langle |E_s|^2 \rangle \neq 0$, $\langle |E_p|^2 \rangle \neq 0$, and $|\mu| \neq 1$, the ensuing partially coherent and partially polarized evanescent field is invariably 3D in character (Norrman, Friberg, et al., 2017). In other words, for an evanescent wave being partially coherent and partially polarized it is never possible to find a fixed plane in which the electric field vector is restricted. This implies that optical evanescent waves are predominantly 3D light fields, which requires a rigorous 3D treatment to fully understand and characterize their statistical properties. It has been shown further that the spectral polarimetric dimension of any stationary evanescent wave obeys (Norrman, Friberg, et al., 2017)

$$D(\mathbf{r}, \omega) = D(\omega) \leq 3 - \frac{2}{\sqrt{1 + 3\tilde{n}^4 \chi^4}}, \tag{37}$$

with the upper bound reached when the incident light possesses

$$|\mu| = 0, \quad \frac{\langle |E_s|^2 \rangle}{\langle |E_p|^2 \rangle} = \left( \frac{\sin^4 \theta + \gamma^4}{\chi^4} \right) \left( \frac{|t_p|}{|t_s|} \right)^2. \tag{38}$$

For a high refractive-index-contrast interface, such as GaP/air with $\tilde{n} \approx 4$ in the visible regime (Palik, 1998), Eq. (37) implies that the polarimetric dimension may be as high as $D(\omega) \approx 2.96$, while for a usual $SiO_2$/air surface

with $\tilde{n} \approx 1.5$ the maximum is roughly $D(\omega) \approx 2.67$. We especially find that the second condition in Eq. (38) corresponding to the maximum of $D(\omega)$ does not coincide with $\langle|E_s|^2\rangle/\langle|E_p|^2\rangle = |t_p|^2/|t_s|^2$ associated with the minima $\mu_{\mathrm{EM}}(\omega) = 1/\sqrt{2}$ and $P_{3\mathrm{D}}(\omega) = 1/2$ of Eqs. (29) and (30), respectively. Consequently, an evanescent wave which is maximally 3D intensity isotropic does not attain the lowest possible values for the degrees of coherence and polarization, an indication that a 3D evanescent wave with high intensity isotropy (polarimetric dimension) possesses a quite large spin anisotropy (Gil et al., 2019).

## 4.4 Polarimetric nonregularity

A specific recent finding is that polarization states of 3D light fields can be classified into *regular states* and *nonregular states* (Gil et al., 2017, 2018a). Such a classification is based on the structure of the so-called *characteristic decomposition* of the 3 × 3 polarization matrix $\mathbf{R}$ (Gil, 2007; Gil & San José, 2010):

$$\mathbf{R} = I[P_1\hat{\mathbf{R}}_{\mathrm{p}} + (P_2 - P_1)\hat{\mathbf{R}}_{\mathrm{m}} + (1 - P_2)\hat{\mathbf{R}}_{\mathrm{u}}]. \tag{39}$$

Here $I = \mathrm{tr}\mathbf{R} = \lambda_1 + \lambda_2 + \lambda_3$ is the intensity as before, with $\lambda_1 \geq \lambda_2 \geq \lambda_3 \geq 0$ being the eigenvalues of $\mathbf{R}$, while

$$P_1 = \hat{\lambda}_1 - \hat{\lambda}_2, \quad P_2 = 1 - 3\hat{\lambda}_3 \quad (0 \leq P_1 \leq P_2 \leq 1) \tag{40}$$

are the *indices of polarimetric purity* (Gil, 2007; San José & Gil, 2011), with $\hat{\lambda}_j = \lambda_j/I$ for $j \in \{1, 2, 3\}$. In addition,

$$\begin{gathered}\hat{\mathbf{R}}_{\mathrm{p}} = \mathbf{U}\mathrm{diag}(1,0,0)\mathbf{U}^{\dagger}, \quad \hat{\mathbf{R}}_{\mathrm{m}} = \frac{1}{2}\mathbf{U}\mathrm{diag}(1,1,0)\mathbf{U}^{\dagger}, \\ \hat{\mathbf{R}}_{\mathrm{u}} = \frac{1}{3}\mathbf{U}\mathrm{diag}(1,1,1)\mathbf{U}^{\dagger} = \frac{1}{3}\mathbf{I},\end{gathered} \tag{41}$$

where $\mathbf{U}$ is the unitary matrix that diagonalizes $\mathbf{R}$, $\mathbf{I}$ is the 3 × 3 identity matrix, and the dagger denotes conjugate transpose. While the matrices $\hat{\mathbf{R}}_{\mathrm{p}}$ and $\hat{\mathbf{R}}_{\mathrm{u}}$ describe, respectively, a polarized state and an unpolarized 3D state, the physical meaning of $\hat{\mathbf{R}}_{\mathrm{m}}$ is more involved.

When $\hat{\mathbf{R}}_{\mathrm{m}}$ is a real matrix, it represents unpolarized 2D light, i.e., light whose electric field evolves fully randomly in a fixed plane. In this case (and in the particular scenario $P_1 = P_2$ for which $\hat{\mathbf{R}}_{\mathrm{m}}$ is absent in the characteristic decomposition) the polarization state $\mathbf{R}$ is called *regular*, only encountered when the smallest eigenvalue $0 \leq \hat{m}_3 \leq 1/4$ of the real part $\hat{\mathbf{R}}'_{\mathrm{m}}$ is zero (Gil et al., 2017). If $\hat{\mathbf{R}}_{\mathrm{m}}$ is instead a complex matrix, it corresponds

to an equiprobable mixture of two mutually orthogonal states whose electric field ellipses lie in different planes (Gil et al., 2017), whereupon $\hat{\mathbf{R}}_{\mathrm{m}}$ does not represent unpolarized 2D light but genuine 3D light. The polarization state $\mathbf{R}$ of such a light field, met when $0 < \hat{m}_3 \leq 1/4$, is said to be *nonregular*. The maximum value $\hat{m}_3 = 1/4$ is saturated when the middle component $\hat{\mathbf{R}}_{\mathrm{m}}$ is in a *perfect nonregular state*, viz., a state which is an equiprobable mixture of a circularly polarized state and a mutually orthogonal linearly polarized state (Gil et al., 2018a). The nonregularity of the full state $\mathbf{R}$ can be characterized quantitatively by means of the *degree of nonregularity* (Gil et al., 2018a)

$$P_{\mathrm{N}} = 4(P_2 - P_1)\hat{m}_3, \tag{42}$$

with the minimum $P_{\mathrm{N}} = 0$ always, and only, taking place for regular states, while values within the interval $0 < P_{\mathrm{N}} \leq 1$ are signatures of nonregularity. The maximum $P_{\mathrm{N}} = 1$ is reached exclusively for *maximally nonregular states* with $P_1 = 0$, $P_2 = 1$, and $\hat{m}_3 = 1/4$. Thus $P_{\mathrm{N}} = 1$ corresponds univocally to 3D polarization states satisfying $\mathbf{R} = I\hat{\mathbf{R}}_{\mathrm{m}}$ and $\hat{m}_3 = 1/4$, implying that all maximally nonregular states are perfect nonregular states.

It has been shown that in the space–frequency domain the middle term $\hat{\mathbf{\Phi}}_{\mathrm{m}}(\mathbf{r}, \omega)$ of a stationary partially coherent and partially polarized evanescent wave takes the form (Norrman et al., 2019)

$$\hat{\mathbf{\Phi}}_{\mathrm{m}}(\mathbf{r}, \omega) = \hat{\mathbf{\Phi}}_{\mathrm{m}}(\omega) = \frac{1}{2}\left(\hat{\mathbf{s}}^{*}\hat{\mathbf{s}}^{\mathrm{T}} + \hat{\mathbf{p}}^{*}\hat{\mathbf{p}}^{\mathrm{T}}\right), \tag{43}$$

with the polarization vectors $\hat{\mathbf{s}}$ and $\hat{\mathbf{p}}$ given in Eq. (23). The state $\hat{\mathbf{\Phi}}_{\mathrm{m}}(\omega)$ in Eq. (43) can thus be interpreted physically as an equiprobable mixture of a linear *s*-polarized state and an elliptical *p*-polarized state. Most importantly, the fact that $\hat{\mathbf{\Phi}}_{\mathrm{m}}(\omega)$ is a complex matrix dictates that any partially coherent and partially polarized evanescent wave is always in a nonregular polarization state (Norrman et al., 2019). Moreover, the degree of nonregularity for the whole state in Eq. (27) reads (Norrman et al., 2019)

$$P_{\mathrm{N}}(\mathbf{r}, \omega) = P_{\mathrm{N}}(\omega) = 2(1 - P_1)\left(\frac{\gamma}{\chi}\right)^2, \tag{44}$$

with the associated indices of purity given as

$$P_1 = \sqrt{1 - 4\frac{(1 - |\mu|^2)w_s w_p}{(w_s + w_p)^2}}, \quad P_2 = 1. \tag{45}$$

The condition $P_2 = 1$ indicates that the last component in the characteristic decomposition (39) always vanishes for the evanescent wave.

From Eqs. (22), (44), and (45) one further concludes that the degree of nonregularity of the evanescent wave is bounded from above as

$$P_{\mathrm{N}}(\omega) \leq 1 - \frac{1}{2(\tilde{n}\sin\theta)^2 - 1}, \tag{46}$$

with the upper limit saturated for an excitation beam satisfying

$$|\mu| = 0, \quad \frac{\langle |E_s|^2 \rangle}{\langle |E_p|^2 \rangle} = \frac{|t_p|^2}{|t_s|^2}. \tag{47}$$

In such a case $P_1 = 0$ according to Eq. (45), whereupon the characteristic decomposition (39) states that the full polarization matrix of the evanescent wave in Eq. (27) is directly proportional to the middle term in Eq. (43). The conditions in Eq. (47) corresponding to the maximum value of $P_{\mathrm{N}}(\omega)$ are actually exactly the same as those corresponding to the minimum values $\mu_{\mathrm{EM}}(\omega) = 1/\sqrt{2}$ and $P_{3\mathrm{D}}(\omega) = 1/2$ of Eqs. (29) and (30), respectively. This implies that an evanescent wave of maximal possible degree of nonregularity has lowest attainable degrees of coherence and polarization, and vice versa. As an example, if $\tilde{n} \approx 4$ as for GaP/air in the visible regime (Palik, 1998), Eq. (46) indicates that the spectral degree of nonregularity may be as high as $P_{\mathrm{N}}(\omega) \approx 0.97$, which virtually corresponds to a perfect nonregular state. In such a scenario, the evanescent wave is in an equiprobable mixture of a linear *s*-polarized state and an almost circular *p*-polarized state (Norrman et al., 2019). For a typical $SiO_2$/air interface ($\tilde{n} \approx 1.5$), the maximum is about $P_{\mathrm{N}}(\omega) \approx 0.71$.

## 5. Partially coherent surface plasmon polariton fields

Due to its unique physical characteristics, the celebrated SPP has been in the spotlight of nanophotonics (Novotny & Hecht, 2012) and triggered the emergence of plasmonics (Maier, 2007; Maradudin et al., 2014) as an own separate field covering cross-disciplinary science and engineering (Zayats, Smolyaninov, & Maradudin, 2005; Zhang, Zhang, & Xu, 2012). As discussed in Sections 2 and 3, SPPs can have a significant impact on the coherence of external light fields; yet, very little research has been devoted to investigate the coherence of SPPs themselves. Usually the SPPs are considered as completely coherent, but in practice thermal effects, surface roughness, metal impurities, and random light fluctuations under

SPP excitation, among other effects, inevitably reduce the SPP coherence to some extent, rendering the SPP field partially coherent. However, there is an increasing recognition that partial coherence, as a novel degree of freedom, has a decisive role in manipulating the spatial, temporal, and polarization properties of SPP fields (Aberra Guebrou, Laverdant, Symonds, Vignoli, & Bellessa, 2012; Laverdant, Aberra Guebrou, Bessueille, Symonds, & Bellessa, 2014; Norrman, Setälä, & Friberg, 2015b; Wang et al., 2014). Controlling and customizing the coherence of SPPs, as of propagating optical beams (Chen & Cai, 2014; Chen, Gu, Wang, & Cai, 2015; Chen, Liu, Wang, Zhao, & Cai, 2014; Chen, Ponomarenko, & Cai, 2016, 2017; Chen, Wang, et al., 2014; Mao et al., 2019), is thereby of fundamental importance and may pave new avenues for sensing, interferometry, spectroscopy, morphological studies, subwavelength imaging, excitation of nanoparticles, coupling of light-emitting elements, and photonic information transfer.

A crucial step in this direction was taken recently via the advancement of a general theory of partially coherent, polychromatic SPPs in the Kretschmann setup (Norrman, Ponomarenko, & Friberg, 2016). The concept of plasmon coherence engineering for tailoring the SPP field coherence by controlling the statistical properties of the excitation light source was also established (Norrman et al., 2016). Soon after, a simple and robust scheme based on point-dipole nanoscattering to recover the SPP coherence from a spectrum measurement in the far zone was proposed (Chen, Norrman, Ponomarenko, & Friberg, 2017), which was later confirmed numerically by studying scattering of partially coherent SPPs from a metallic nanostripe (Daniel, Saastamoinen, Ponomarenko, & Friberg, 2019). In these contexts, the coherent-mode decomposition (Mao, Chen, Ponomarenko, & Friberg, 2018) and the two-point Stokes parameters (Chen, Norrman, et al., 2017) have proven powerful in understanding the intrinsic SPP-coherence character. Moreover, utilizing radially propagating SPPs, and suitably customizing their correlations by means of plasmon coherence engineering, enables to generate a variety of complex-structured SPP fields of controlled coherence states (Chen, Norrman, Ponomarenko, & Friberg, 2018a, 2018b, 2019), with potential applications in nanoparticle excitation, optical tweezing, plasmonic field traps, and other photonic manipulations at subwavelength scales.

In this section, we review the recent breakthroughs and advances in this emerging branch of nanophotonics—statistical plasmonics.

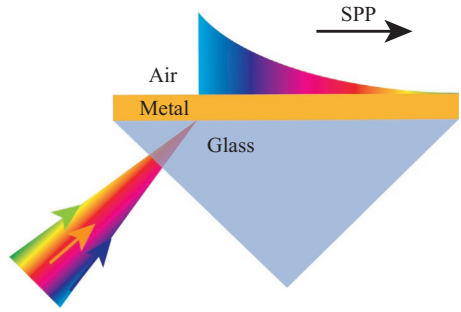


**Fig. 16** Excitation of a polychromatic SPP field in the Kretschmann configuration.

## 5.1 Plasmon coherence engineering

Let us consider a *polychromatic* SPP field generated by a TM-polarized beam in the Kretschmann setup (Fig. 16), involving a homogenous, isotropic, and nonmagnetic metal film deposited on a glass prism and situated in the $xy$ plane. The planar metal–air interface coincides with $z = 0$ and the SPP propagation direction is taken along the $x$ axis. The SPP electric field in air, at a space–time point $(\mathbf{r}, t)$, then reads (Norrman et al., 2016)

$$\mathbf{E}(\mathbf{r},t) = \int_{\omega_-}^{\omega_+} E(\omega)\hat{\mathbf{p}}(\omega)\mathrm{e}^{\mathrm{i}[\mathbf{k}(\omega)\cdot\mathbf{r}-\omega t]}\mathrm{d}\omega, \tag{48}$$

where $\omega_\pm$ is the (angular) frequency bandwidth, $E(\omega)$ denotes the (complex) spectral amplitude of a monochromatic SPP at the origin ($\mathbf{r} = 0$), and

$$\mathbf{k}(\omega) = k_x(\omega)\hat{\mathbf{e}}_x + k_z(\omega)\hat{\mathbf{e}}_z, \quad \hat{\mathbf{p}}(\omega) = [\mathbf{k}(\omega) \times \hat{\mathbf{e}}_y]/|\mathbf{k}(\omega)| \tag{49}$$

are the SPP wave and unit polarization vectors, respectively, with $\hat{\mathbf{e}}_x$, $\hat{\mathbf{e}}_y$, and $\hat{\mathbf{e}}_z$ being the Cartesian unit vectors. The film is assumed to be thick enough so that any mode overlap across the metal can be neglected (Norrman, Setälä, & Friberg, 2014a, 2014b), whereupon the components of the SPP wave vector at the metal–air interface in Eq. (49) are given by (Norrman, Setälä, & Friberg, 2013)

$$k_x(\omega) = \frac{\omega}{c}\sqrt{\frac{\epsilon(\omega)}{\epsilon(\omega)+1}}, \qquad k_z(\omega) = \frac{\omega}{c}\sqrt{\frac{1}{\epsilon(\omega)+1}}, \tag{50}$$

where $c$ is the speed of light and $\epsilon(\omega)$ is the complex (relative) permittivity of the metal.

The second-order correlations of a (generally nonstationary) electric field are in the space–time and space–frequency domains encoded in the temporal and spectral coherence matrices (Voipio, Setälä, & Friberg, 2013)

$$\mathbf{\Gamma}(\mathbf{r}_1, t_1; \mathbf{r}_2, t_2) = \langle \mathbf{E}^*(\mathbf{r}_1, t_1)\mathbf{E}^{\mathrm{T}}(\mathbf{r}_2, t_2)\rangle, \tag{51}$$

$$\mathbf{W}(\mathbf{r}_1, \omega_1; \mathbf{r}_2, \omega_2) = \langle \mathbf{E}^*(\mathbf{r}_1, \omega_1)\mathbf{E}^{\mathrm{T}}(\mathbf{r}_2, \omega_2)\rangle, \tag{52}$$

where the asterisk, superscript T, and angle brackets stand for complex conjugate, matrix transpose, and ensemble average, respectively, as before. Taking $\mathbf{E}(\mathbf{r},t)$ in Eq. (48) as a field realization, we obtain the *SPP temporal coherence matrix* (Norrman et al., 2016)

$$\mathbf{\Gamma}(\mathbf{r}_1, t_1; \mathbf{r}_2, t_2) = \iint_{\omega_-}^{\omega_+} \mathbf{W}(\mathbf{r}_1, \omega_1; \mathbf{r}_2, \omega_2) \mathrm{e}^{-\mathrm{i}(\omega_2 t_2 - \omega_1 t_1)} \mathrm{d}\omega_1 \mathrm{d}\omega_2, \tag{53}$$

including the corresponding *SPP spectral coherence matrix*

$$\mathbf{W}(\mathbf{r}_1, \omega_1; \mathbf{r}_2, \omega_2) = W(\omega_1, \omega_2)\hat{\mathbf{p}}^*(\omega_1)\hat{\mathbf{p}}^{\mathrm{T}}(\omega_2)\mathrm{e}^{\mathrm{i}[\mathbf{k}(\omega_2)\cdot\mathbf{r}_2 - \mathbf{k}^*(\omega_1)\cdot\mathbf{r}_1]}, \tag{54}$$

which in turn contains the *SPP spectral correlation function*

$$W(\omega_1, \omega_2) = \langle E^*(\omega_1)E(\omega_2)\rangle. \tag{55}$$

Eqs. (53) and (54) are general electric coherence matrices which cover any partially coherent polychromatic SPP field; they place no restrictions on metal dispersion/absorption, the field spectrum, or the spectral correlations (Norrman et al., 2016).

It can be inferred from Eqs. (53) and (54) that once the metal parameters and the frequency bandwidth are known, all elements apart from $W(\omega_1, \omega_2)$ are specified in the coherence matrices. Hence, the SPP spectral correlation function $W(\omega_1, \omega_2)$ in Eq. (55) provides an essential *degree of freedom* that can be exploited to govern the spectral and thus also the temporal statistical properties of the SPP field. The idea of *plasmon coherence engineering* is to morph the SPP spectral correlation function $W(\omega_1, \omega_2)$ exactly into a desired form by controlling the coherence state of the excitation light (Norrman et al., 2016).

To this end, we first consider the angular spectrum representation (Mandel & Wolf, 1995) of an incident, partially coherent, polychromatic light beam. The spectral electric correlation function of the beam can be written as

$$\mathcal{W}(k_{X1}, \omega_1; k_{X2}, \omega_2) = \langle \mathcal{E}^*(k_{X1}, \omega_1)\mathcal{E}(k_{X2}, \omega_2)\rangle, \tag{56}$$

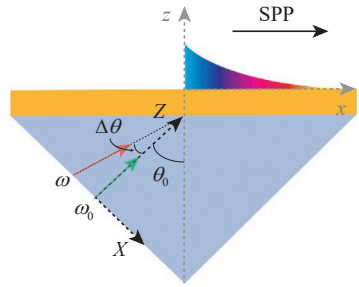


**Fig. 17** Notations related to plasmon coherence engineering with polychromatic beam illumination. The angle $\theta_0$ between the *xz* and *XZ* frames corresponds to perfect phase matching between the central angular spectrum mode of frequency $\omega_0$ and the respective SPP. The angular spectrum wave of $\omega \neq \omega_0$ and incident at an angle $\Delta\theta$ with respect to the *Z* axis excites the associated SPP for every frequency within the excitation bandwidth.

where $\mathcal{E}(k_X, \omega)$ is the electric field amplitude of the angular spectrum mode at frequency $\omega$, with $k_X$ being the tangential wave-vector component in a new coordinate frame $XZ$, in which the $Z$ axis makes an angle $\theta_0$ with respect to the $z$ axis of the original $xz$ frame (Fig. 17). We further choose $\theta_0$ such that, in the $xz$ frame, the tangential wave-vector component of the beam mode at the central frequency $\omega_0$ and $k_X = 0$ within the angular spectrum exactly corresponds to the real part $k'_x(\omega_0)$ of the SPP obtained from Eq. (50), i.e.,

$$n(\omega_0)\frac{\omega_0}{c}\sin\theta_0 = k'_x(\omega_0), \tag{57}$$

where $n(\omega_0)$ is the refractive index of the prism. This condition represents precise phase matching between the central illuminating plane wave and the central excited SPP mode at the metal–air interface.

Next, a similar phase matching condition must be imposed for the other illumination plane waves as well to ensure that an SPP mode is generated at every frequency $\omega$ within the excitation source bandwidth. In other words, for a frequency $\omega \neq \omega_0$, the angular spectrum mode having $k_X \approx n(\omega)(\omega/c)\sin\Delta\theta$ couples to the corresponding SPP mode, where $\Delta\theta$ is the angle between the wave vector and $Z$ axis. In the $xz$ frame this implies the constraint

$$n(\omega)\frac{\omega}{c}\sin\theta = k_Z\sin\theta_0 + k_X\cos\theta_0 = k'_x(\omega), \tag{58}$$

with $\theta = \theta_0 + \Delta\theta$ and $k_Z^2 + k_X^2 = [n(\omega)\omega/c]^2$. By assuming a paraxial incident beam, i.e., $\Delta\theta \approx k_X/k_Z \ll \theta_0$ and $k_Z \approx n(\omega)\omega/c$, we obtain from Eqs. (57) and (58) the coupling condition

$$k_X = \frac{k_x'(\omega) - k_x'(\omega_0)}{\cos\theta_0}. \tag{59}$$

Thus, at each frequency $\omega$ within the bandwidth, the angular spectrum wave satisfying Eq. (59) will generate the respective monochromatic SPP mode. Eventually, as the spectral amplitudes of the SPP field and the illumination obey $E(\omega) \propto \mathcal{E}(k_X, \omega)$, with the exact coupling strength specified by the slab transmission coefficient, we obtain the relation between the SPP correlation function and the correlation function of the incident beam (Norrman et al., 2016):

$$W(\omega_1, \omega_2) \propto \mathcal{W}\left[\frac{k_x'(\omega_1) - k_x'(\omega_0)}{\cos\theta_0}, \omega_1; \frac{k_x'(\omega_2) - k_x'(\omega_0)}{\cos\theta_0}, \omega_2\right]. \tag{60}$$

Eq. (60) dictates exactly how the spectral correlations of the illumination are to be tuned for engineering the spectral correlations, and thereby all the statistical properties, of the SPP field into the desired form.

## 5.2 Plasmon coherence determination

Optical coherence of a genuine vector-light field is usually determined in Young's two-pinhole experiment with the aid of polarization wave plates and polarizers (Friberg & Setälä, 2016). Yet, in the case of optical near and surface fields, customary polarization elements cannot be employed when measuring such *electromagnetic coherence*, due to the specific field and nanoscale features, whereupon other methods must be used (Leppänen, Friberg, & Setälä, 2014). Recently it was shown that the electromagnetic coherence of a *statistically stationary*, polychromatic SPP field can be determined by measuring the far-field spectrum scattered by a nanoprobe placed in the vicinity of the metal surface in the Kretschmann setup (Chen, Norrman, et al., 2017). This result is understood by first considering the SPP coherence matrices in Eqs. (53) and (54). Since different frequency components are uncorrelated for a stationary field (Mandel & Wolf, 1995), the SPP spectral coherence matrix becomes

$$\mathbf{W}(\mathbf{r}_1, \mathbf{r}_2, \omega) = W(\omega)\hat{\mathbf{p}}^*(\omega)\hat{\mathbf{p}}^{\mathrm{T}}(\omega)\mathrm{e}^{\mathrm{i}[\mathbf{k}(\omega)\cdot\mathbf{r}_2 - \mathbf{k}^*(\omega)\cdot\mathbf{r}_1]}, \tag{61}$$

including the SPP spectral function

$$W(\omega) = \langle |E(\omega)|^2 \rangle. \tag{62}$$

The corresponding SPP temporal coherence matrix, which in the stationary scenario depends only on the time separation $\tau = t_2 - t_1$, is obtained via the (generalized) Wiener–Khinchin theorem (Mandel & Wolf, 1995)

$$\Gamma(\mathbf{r}_1, \mathbf{r}_2, \tau) = \int_0^\infty \mathbf{W}(\mathbf{r}_1, \mathbf{r}_2, \omega) \mathrm{e}^{-\mathrm{i}\omega\tau} \mathrm{d}\omega. \tag{63}$$

In particular, for a given metal, the two SPP coherence matrices are entirely specified by the single spectral function $W(\omega)$. Hence, once $W(\omega)$ is known, all the second-order statistical properties of the stationary SPP field can be completely recovered. We demonstrate next how the function $W(\omega)$ may be simply determined by utilizing nanoparticle scattering.

Let us consider a spherical metallic nanoparticle placed in close proximity of the metal slab at the position $\mathbf{r}_0 = x_0\hat{\mathbf{e}}_x + z_0\hat{\mathbf{e}}_z$ (Fig. 18), with the radius much smaller than the minimum wavelength and the minimum penetration depth within the SPP bandwidth. The scattering can thereby be treated in the electrostatic dipole approximation (Novotny & Hecht, 2012), whereupon the radiated electric far field in the $xz$ plane, at a distance $s$ in the

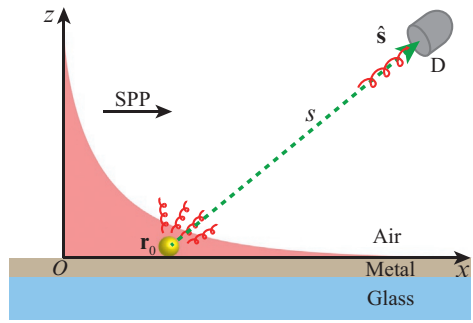


**Fig. 18** Schematic of determining the electromagnetic coherence of a stationary, polychromatic SPP field via nanoscattering in the Kretschmann setup. The geometry and the SPP field are uniform in the $y$ direction. The nanoparticle is located at point $\mathbf{r}_0$ near the metal surface $z = 0$ and the scattered far field is observed by detector D at a distance $s$ in the direction $\hat{\mathbf{s}}$ from $\mathbf{r}_0$. *From Chen, Y., Norrman, A., Ponomarenko, S. A., & Friberg, A. T. (2017). Plasmon coherence determination by nanoscattering. Optics Letters, 42(17), 3279–3282.*

direction $\hat{\mathbf{s}} = \mathbf{s}/s$ [measured from $\mathbf{r}_0$ and not to be mixed with the unit polarization vector in Eq. (23)], is given by

$$\mathbf{E}_\infty(\mathbf{r},\omega) = \left(\frac{\omega^2}{4\pi c^2\epsilon_0}\right)\hat{\mathbf{s}} \times [\mathbf{d}(\mathbf{r}_0,\omega) \times \hat{\mathbf{s}}]\,\frac{e^{i(\omega/c)s}}{s}, \tag{64}$$

with $\epsilon_0$ being the vacuum permittivity and $\mathbf{d}(\mathbf{r}_0, \omega)$ denoting the scatterer's dipole moment. In the electrostatic regime, $\mathbf{d}(\mathbf{r}_0, \omega)$ is directly proportional to the SPP field through (Novotny & Hecht, 2012)

$$\mathbf{d}(\mathbf{r}_0,\omega) = \alpha(\omega)\mathbf{E}(\mathbf{r}_0,\omega), \quad \alpha(\omega) = 4\pi\epsilon_0\,\frac{\varepsilon(\omega)-1}{\varepsilon(\omega)+2}\,a^3, \tag{65}$$

where $\alpha(\omega)$ is the polarizability, $\varepsilon(\omega)$ is the complex permittivity, and $a$ is the radius of the nanosphere. In Eqs. (64) and (65) we neglect the effects of radiation reaction and the presence of the metal surface. In practice, $\alpha(\omega)$ will be replaced by an effective polarizability $\alpha_{\text{eff}}(\omega)$ and $\mathbf{E}_\infty(\mathbf{r}, \omega)$ acquires an additional contribution from the metal reflection. These effects may readily be included in a quantitative analysis and in experiments (Leppänen, Saastamoinen, Lehtolahti, Friberg, & Setälä, 2016), and they will not impact the main conclusions below.

In polar coordinates, with $\theta$ being the angle between $\hat{\mathbf{s}}$ and the $x$ axis, we obtain from Eqs. (64) and (65) the far-field expression

$$\mathbf{E}_\infty(\mathbf{r},\theta,\omega) = \left(\frac{\omega^2}{4\pi c^2\epsilon_0}\right)\alpha(\omega)\mathbf{M}(\theta)\mathbf{E}(\mathbf{r}_0,\omega)\,\frac{e^{i(\omega/c)s}}{s}, \tag{66}$$

where we have introduced the symmetric matrix

$$\mathbf{M}(\theta) = \begin{pmatrix} \sin^2\theta & -\sin\theta\cos\theta \\ -\sin\theta\cos\theta & \cos^2\theta \end{pmatrix}. \tag{67}$$

Using Eq. (66) together with the property $\mathbf{M}^2(\theta) = \mathbf{M}(\theta)$, one finds that the spectrum of the scattered field in the far zone at point $\mathbf{r}$ becomes

$$\begin{aligned} S_\infty(\mathbf{r},\theta,\omega) &= \mathrm{tr}[\langle \mathbf{E}^*_\infty(\mathbf{r},\theta,\omega)\mathbf{E}^{\mathrm{T}}_\infty(\mathbf{r},\theta,\omega)\rangle] \\ &= \left(\frac{\omega^2}{4\pi c^2\epsilon_0}\right)^2 \frac{|\alpha(\omega)|^2}{s^2}\,\mathrm{tr}[\mathbf{M}(\theta)\mathbf{\Phi}(\mathbf{r}_0,\omega)], \end{aligned} \tag{68}$$

where $\mathbf{\Phi}(\mathbf{r}_0, \omega) = \langle \mathbf{E}^*(\mathbf{r}_0, \omega)\mathbf{E}^{\mathrm{T}}(\mathbf{r}_0, \omega)\rangle$ is the spectral polarization matrix of the SPP field at point $\mathbf{r}_0$. According to Eq. (61),

$$\mathbf{\Phi}(\mathbf{r}_0, \omega) = W(\omega)\hat{\mathbf{p}}^*(\omega)\hat{\mathbf{p}}^{\mathrm{T}}(\omega)\mathrm{e}^{-2\mathbf{k}''(\omega)\cdot\mathbf{r}_0}, \tag{69}$$

with the double prime denoting the imaginary part. On combining Eqs. (68) and (69), we then find a *one-to-one relationship* between the SPP spectral function $W(\omega)$ and the far-field spectrum $S_\infty(\mathbf{r}, \theta, \omega)$, viz.,

$$W(\omega) = \left(\frac{4\pi c^2\epsilon_0}{\omega^2}\right)^2 \frac{s^2}{|\alpha(\omega)|^2} \frac{\mathrm{e}^{2\mathbf{k}''(\omega)\cdot\mathbf{r}_0}}{\mathrm{tr}[\mathbf{M}(\theta)\hat{\mathbf{p}}^*(\omega)\hat{\mathbf{p}}^{\mathrm{T}}(\omega)]} S_\infty(\mathbf{r}, \theta, \omega). \tag{70}$$

Eq. (70) clearly implies that when the material parameters and the radius of the nanoscatterer are known, the spectral function $W(\omega)$, and thereby the spectral coherence matrix $\mathbf{W}(\mathbf{r}_1, \mathbf{r}_2, \omega)$ in Eq. (61) as well as the temporal coherence matrix $\mathbf{\Gamma}(\mathbf{r}_1, \mathbf{r}_2, \tau)$ in Eq. (63), can be completely recovered from just a single spectrum measurement in the far zone.

## 5.3 Coherent-mode representation

According to Wolf's *coherent-mode expansion* (Mandel & Wolf, 1995), a partially coherent field can be decomposed into a set of mutually uncorrelated elementary coherent modes. Such a representation often proves instrumental to gain insight into a generally quite complicated space–time behavior of partially coherent fields, and it also allows to assess how coherent, on average, a random field is within a finite volume (Ostrovsky, 2006). The coherent-mode representation for partially coherent SPP fields has been developed by expanding the SPP spectral correlation function $W(\omega_1, \omega_2)$ in Eq. (55) via scalar coherent modes as (Mao et al., 2018)

$$W(\omega_1, \omega_2) = \sum_n \beta_n \varphi_n^*(\omega_1)\varphi_n(\omega_2), \tag{71}$$

where $\{\beta_n\}$ are real and nonnegative eigenvalues (to ensure the nonnegative definiteness condition of a coherence function) of the linear Fredholm integral equation, and the respective eigenfunctions $\{\varphi_n(\omega)\}$ form an orthonormal set. It follows from Eqs. (53)–(55) and (71) that the SPP temporal coherence matrix can be expressed as a *vectorial coherent-mode representation*

$$\mathbf{\Gamma}(\mathbf{r}_1, t_1; \mathbf{r}_2, t_2) = \sum_n \nu_n \mathbf{\Phi}_n^*(\mathbf{r}_1, t_1)\mathbf{\Phi}_n^{\mathrm{T}}(\mathbf{r}_2, t_2), \tag{72}$$

where $\{\mathbf{\Phi}_n(\mathbf{r}, t)\}$ are *coherent vector pseudo-modes*; they are normalized, but generally not orthogonal even if the scalar coherent modes $\{\varphi_n(\omega)\}$ are (Mao et al., 2018). Yet, the coherent vector pseudo-modes are still uncorrelated and the modal weights $\{\nu_n\}$, which specify the fraction of the source energy carried by a given mode, add up to the total energy of the source.

The coherent-mode representation outlined above is helpful in a quantitative assessment of how coherent the entire field is by means of the global (which is sometimes also referred to as overall or effective) degree of coherence (Blomstedt, Setälä, & Friberg, 2007b, 2015; Mandel & Wolf, 1995; Ostrovsky, 2006). The *global degree of coherence* of the partially coherent SPPs is then defined as the ratio of the energy carried by the lowest-order mode to the total energy of the SPP source, in complete analogy with partially coherent volume sources (Starikov, 1982), as

$$G = \frac{\nu_0}{\sum_{n=0}^{N_\mathrm{m}-1} \nu_n}, \tag{73}$$

where $N_\mathrm{m}$ is an effective number of coherent vector modes. The quantity $G$ is bounded between 0 and 1, with $G = 1$ and $G = 0$ representing a fully coherent and incoherent SPP source, respectively. Given the orthonormal modes and the corresponding modal weights of $W(\omega_1, \omega_2)$, which can be determined, at least in principle, by solving the Fredholm integral equation (Mandel & Wolf, 1995), we can obtain the coherent vector pseudo-mode representation for any partially coherent SPP field in the Kretschmann setup, and thus assess the average global coherence of the SPPs within an excitation volume.

As an example, we consider the vectorial coherent pseudo-mode representation of narrowband SPP fields with spectral correlations of the Gaussian Schell-model (GSM) type (Mao et al., 2018)

$$W(\omega_1, \omega_2) = I_0 \mathrm{e}^{-[(\omega_1-\omega_0)^2+(\omega_2-\omega_0)^2]/4\sigma_s^2} \mathrm{e}^{-(\omega_1-\omega_2)^2/2\sigma_c^2}, \tag{74}$$

where $I_0$ is a constant, $\omega_0$ is the central frequency of the polychromatic SPP field, and $\sigma_s$ and $\sigma_c$ denote the SPP spectral width and spectral coherence width, respectively. The normalized eigenfunctions and the corresponding eigenvalues of the GSM source can be obtained analytically (Mandel & Wolf, 1995). If we invoke the narrowband approximation $\epsilon(\omega) \approx \epsilon(\omega_0)$, we end up with the (unnormalized) coherent pseudo-modes (Mao et al., 2018)

$$\mathbf{\Theta}_n(\mathbf{r}, t) = \hat{\mathbf{p}}(\omega_0)\Theta_n(\mathbf{r}, t), \tag{75}$$

including the scalar modal functions

$$\Theta_n(\mathbf{r},t)=\left(\frac{2\pi}{c_0}\right)^{1/4}\frac{\mathrm{i}^n}{(2^n n!)^{1/2}}\mathrm{e}^{\mathrm{i}[\mathbf{k}(\omega_0)\cdot\mathbf{r}-\omega_0 t]} \times H_n\left[\frac{\mathbf{k}(\omega_0)\cdot\mathbf{r}-\omega_0 t}{\sqrt{2c_0}\omega_0}\right]\mathrm{e}^{-[\mathbf{k}(\omega_0)\cdot\mathbf{r}-\omega_0 t]^2/(4c_0\omega_0^2)}, \tag{76}$$

where $H_n[\cdot]$ is a Hermite polynomial of order $n$, and $c_0=(a_0^2+2a_0b_0)^{1/2}$ with $a_0=(4\sigma_s^2)^{-1}$ and $b_0=(2\sigma_c^2)^{-1}$. Fig. 19 displays the space–time distributions

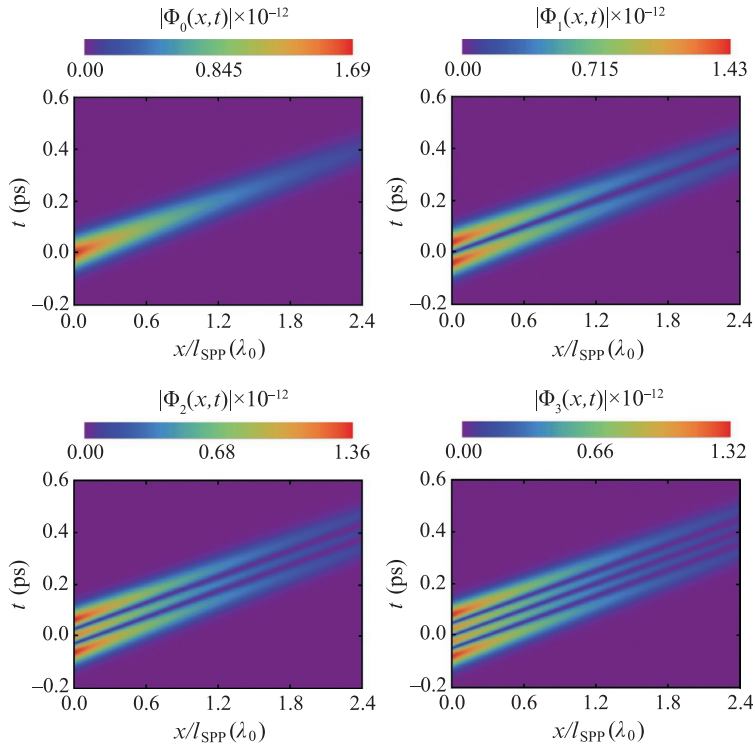


**Fig. 19** Space–time distributions of the first four pseudo-mode amplitudes $|\Phi_n(x, t)|$ for a narrowband GSM SPP field at an Ag/air interface having the central wavelength $\lambda_0 = 653$ nm. The spectral width $\sigma_s$ and the spectral coherence length $\sigma_c$ are $0.02\omega_0$ and $0.004\omega_0$, respectively, where $\omega_0$ is the SPP central frequency. The quantity $l_{\mathrm{SPP}}(\lambda_0)$ is the SPP propagation length. The complex permittivity of Ag is taken from empirical data (Palik, 1998). *From Mao, H., Chen, Y., Ponomarenko, S. A., & Friberg, A. T. (2018). Coherent pseudo-mode representation of partially coherent surface plasmon polaritons. Optics Letters, 43(6), 1395–1398.*

of the first four coherent pseudo-mode functions $\Phi_n(x,t) \equiv \hat{\mathbf{p}}(\omega_0) \cdot \mathbf{\Phi}_n(x,t)$ for narrowband GSM SPPs at an Ag/air surface with the SPP central wavelength $\lambda_0 = 653$ nm. It can be inferred from Fig. 19 that each coherent mode remains highly confined over the SPP propagation length $l_{\mathrm{SPP}}(\lambda_0)$ and that the peak amplitude position of the mode experiences a time shift on SPP propagation away from the excitation point. The lateral shift of each mode in the space–time domain in the absence of dispersion arises from the mode phase shift in the space–frequency domain. Further, the mode of order $n$ has exactly $n$ nodes and thus appears to be split into $n + 1$ lobes due to the GSM source mode modulation.

Fig. 20 shows the global degree of coherence $G$ of narrowband GSM SPPs for $\lambda_0 = 653$ nm at an Ag/air interface as a function of $\sigma_c$ and $\sigma_s$. One finds that $G$ increases with the SPP spectral coherence length $\sigma_c$ (Fig. 20A) and decreases with the SPP spectral width $\sigma_s$ (Fig. 20B). We also observe that $G$ tends to zero for spectrally uncorrelated SPPs ($\sigma_c \to 0$), even though the longitudinal spatial coherence length of such SPPs remains on the order of a few wavelengths. As monochromatic SPP fields ($\sigma_s \to 0$) are completely coherent, their global degree of coherence is unity. It is also instructive to conclude from Fig. 21 that the global degree of coherence of the narrowband GSM SPPs is virtually independent of the central wavelength $\lambda_0$ in the visible range, and is only weakly affected by the metal properties, at least, for typical plasmonic materials. Hence, the global degree of coherence $G$ can be viewed as a robust measure of the overall narrowband SPP coherence.

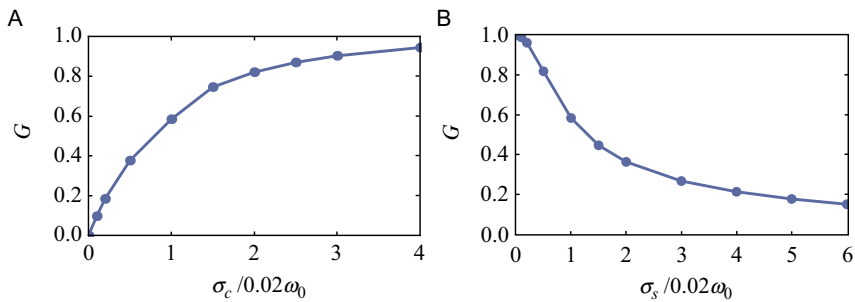


**Fig. 20** Global degree of coherence $G$ of a narrowband GSM SPP field with the central wavelength $\lambda_0 = 653$ nm at an Ag/air interface as a function of (A) the spectral coherence width $\sigma_c$ and (B) the spectral width $\sigma_s$. In (A) $\sigma_s = 0.02\omega_0$ and in (B) $\sigma_c = 0.02\omega_0$, where $\omega_0$ is the SPP central frequency. The complex permittivity of Ag corresponds to empirical data (Palik, 1998). *From Mao, H., Chen, Y., Ponomarenko, S. A., & Friberg, A. T. (2018). Coherent pseudo-mode representation of partially coherent surface plasmon polaritons. Optics Letters, 43(6), 1395–1398.*

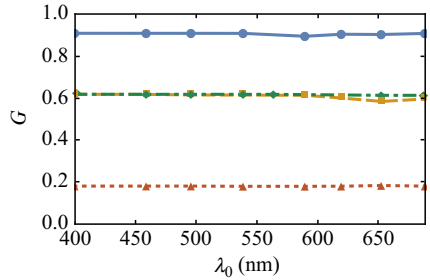


**Fig. 21** Global degree of coherence $G$ of a narrowband GSM SPP field at an Ag/air interface as a function of the central wavelength $\lambda_0$ for different spectral coherence widths $\sigma_c$: $\sigma_c = 0.06\omega_0$ (blue solid curve), $\sigma_c = 0.02\omega_0$ (orange dashed curve), $\sigma_c = 0.004\omega_0$ (red dotted curve). The green dash-dotted curve represents $G$ at an Au/air interface with $\sigma_c = 0.02\omega_0$. The source spectral width $\sigma_s$ is in all cases $0.02\omega_0$, where $\omega_0$ is the central frequency at $\lambda_0 = 653$ nm. Empirical data are used for the complex permittivities of Ag and Au (Palik, 1998). *From Mao, H., Chen, Y., Ponomarenko, S. A., & Friberg, A. T. (2018). Coherent pseudo-mode representation of partially coherent surface plasmon polaritons. Optics Letters, 43(6), 1395–1398.*

## 5.4 Two-point Stokes parameters

Alternatively to the coherence matrix formalism, the second-order correlation properties of a planar light field can be described in terms of the *two-point Stokes parameters* (Ellis & Dogariu, 2004; Korotkova & Wolf, 2005). The two-point Stokes parameters have specific interpretations similar to those of the usual (one-point) Stokes parameters and they have clear physical meanings in beam interferometry (Setälä et al., 2006a; Setälä, Tervo, & Friberg, 2006b; Tervo, Setälä, Roueff, Réfrégier, & Friberg, 2009; Tervo, Setälä, Turunen, & Friberg, 2013), not merely for classical but also for quantum light (Norrman, Blomstedt, et al., 2017; Norrman et al., 2020). For a stationary, two-component field, the two-point Stokes parameters may in the space–time domain be expressed as (Leppänen, Saastamoinen, et al., 2014)

$$\mathcal{S}_n(\mathbf{r}_1, \mathbf{r}_2, \tau) = \mathrm{tr}[\boldsymbol{\Gamma}(\mathbf{r}_1, \mathbf{r}_2, \tau)\boldsymbol{\sigma}_n], \quad n \in \{0, \ldots, 3\}, \tag{77}$$

where $\boldsymbol{\Gamma}(\mathbf{r}_1, \mathbf{r}_2, \tau)$ is the $2 \times 2$ electric coherence matrix, $\boldsymbol{\sigma}_0$ is the $2 \times 2$ unit matrix, and $\boldsymbol{\sigma}_1$, $\boldsymbol{\sigma}_2$, $\boldsymbol{\sigma}_3$ are the Pauli matrices. On using the normalization

$$s_n(\mathbf{r}_1, \mathbf{r}_2, \tau) = \frac{\mathcal{S}_n(\mathbf{r}_1, \mathbf{r}_2, \tau)}{\sqrt{\mathcal{S}_0(\mathbf{r}_1, \mathbf{r}_1, 0)\mathcal{S}_0(\mathbf{r}_2, \mathbf{r}_2, 0)}}, \quad n \in \{0, \ldots, 3\}, \tag{78}$$

the *electromagnetic degree of coherence* (Tervo et al., 2003), describing the totality of vector-field correlations, becomes (Friberg & Setälä, 2016)

$$\gamma_{\mathrm{EM}}(\mathbf{r}_1,\mathbf{r}_2,\tau)=\left[\frac{1}{2}\sum_{n=0}^{3}\left|s_n(\mathbf{r}_1,\mathbf{r}_2,\tau)\right|^2\right]^{1/2}, \tag{79}$$

being the temporal analog of the spectral electromagnetic degree of coherence in Eq. (28).

In plasmonics, the role of the two-point Stokes parameters is more elusive, as the SPP electric field is confined to the propagation plane, but nevertheless they are measurable and yield detailed information about the SPP coherence structure (Chen, Norrman, et al., 2017). According to Eqs. (61)–(63) and (77), the *SPP temporal two-point Stokes parameters* take the form

$$\mathcal{S}_n(\mathbf{r}_1,\mathbf{r}_2,\tau)=\int_0^\infty \mathcal{S}_n(\mathbf{r}_1,\mathbf{r}_2,\omega)\mathrm{e}^{-\mathrm{i}\omega\tau}\mathrm{d}\omega,\quad n\in\{0\ldots,3\}, \tag{80}$$

where the *SPP spectral two-point Stokes parameters* read

$$\mathcal{S}_0(\mathbf{r}_1,\mathbf{r}_2,\omega)=W(\omega)\mathrm{e}^{\mathrm{i}[\mathbf{k}(\omega)\cdot\mathbf{r}_2-\mathbf{k}^*(\omega)\cdot\mathbf{r}_1]}, \tag{81}$$

$$\mathcal{S}_1(\mathbf{r}_1,\mathbf{r}_2,\omega)=W(\omega)\frac{|k_z(\omega)|^2-|k_x(\omega)|^2}{|\mathbf{k}(\omega)|^2}\mathrm{e}^{\mathrm{i}[\mathbf{k}(\omega)\cdot\mathbf{r}_2-\mathbf{k}^*(\omega)\cdot\mathbf{r}_1]}, \tag{82}$$

$$\mathcal{S}_2(\mathbf{r}_1,\mathbf{r}_2,\omega)=W(\omega)\frac{-2[k_x^*(\omega)k_z(\omega)]'}{|\mathbf{k}(\omega)|^2}\mathrm{e}^{\mathrm{i}[\mathbf{k}(\omega)\cdot\mathbf{r}_2-\mathbf{k}^*(\omega)\cdot\mathbf{r}_1]}, \tag{83}$$

$$\mathcal{S}_3(\mathbf{r}_1,\mathbf{r}_2,\omega)=W(\omega)\frac{2[k_x^*(\omega)k_z(\omega)]''}{|\mathbf{k}(\omega)|^2}\mathrm{e}^{\mathrm{i}[\mathbf{k}(\omega)\cdot\mathbf{r}_2-\mathbf{k}^*(\omega)\cdot\mathbf{r}_1]}, \tag{84}$$

with the prime and double prime standing for the real and imaginary parts, respectively. Eqs. (80)–(84) show explicitly that, for a given metal, the two-point and thus also the one-point ($\mathbf{r}_1=\mathbf{r}_2=\mathbf{r}$) Stokes parameters of a statistically stationary SPP field are fully determined by the SPP spectral function $W(\omega)$ in Eq. (62). Consequently, employing the scheme of plasmon coherence determination by nanoscattering discussed in Section 5.2, all the SPP Stokes parameters and thereby also all the SPP statistical properties can be completely ascertained.

Fig. 22 shows the equal-time ($\tau=0$) longitudinal coherence behavior of a stationary SPP field on an Ag/air interface ($z_1=z_2=0$), excited by two independent Kr lasers at point $x_1=0$ of wavelengths 676.4 and

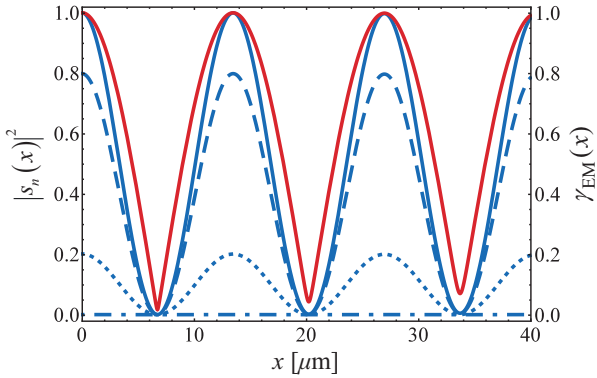


**Fig. 22** Squared magnitudes of the normalized, equal-time, two-point Stokes parameters $s_0(x)$ (solid blue curve), $s_1(x)$ (dashed blue curve), $s_2(x)$ (dash-dotted blue curve), and $s_3(x)$ (dotted blue curve), as well as the equal-time degree of electromagnetic coherence $\gamma_{EM}(x)$ (solid red curve), for a stationary SPP field excited by two independent Kr lasers of wavelengths 676.4 and 647.1 nm at an Ag/air interface. The complex permittivity of Ag is obtained from empirical data (Palik, 1998). *From Chen, Y., Norrman, A., Ponomarenko, S. A., & Friberg, A. T. (2017). Plasmon coherence determination by nanoscattering. Optics Letters, 42(17), 3279–3282.*

647.1 nm (Chen, Norrman, et al., 2017). One observes that both the electromagnetic degree of coherence $\gamma_{EM}(x)$ as well as the magnitudes of the normalized two-point Stokes parameters $|s_n(x)|$, with the abbreviation $x = x_2$, display a persistent, long-range coherence oscillation. The strong coherence modulation follows from *statistical similarity* (Ponomarenko, Roychowdhury, & Wolf, 2005; Voipio, Setälä, & Friberg, 2015) and is not strictly periodic owing to the slightly different polarization states and decay rates of the two SPP modes. We further find that apart from $|s_0(x)|$, which describes the sum of the $x$- and $z$-polarized field correlations between points (0, 0) and ($x$, 0), the main contributor to $\gamma_{EM}(x)$ is $|s_1(x)|$, i.e., the measure of the $z$-polarized field correlations over the $x$-polarized ones, and to a lesser extent $|s_3(x)|$, which indicates excess of correlations among the circularly polarized field components. The contribution from $|s_2(x)|$, corresponding to correlations in the $\pm\pi/4$-polarized field components, is seen to be negligible. Similar relative strengths of the two-point Stokes parameters are encountered for a broadband Gaussian SPP field (Chen, Norrman, et al., 2017). These properties originate from the SPP electric field being almost linearly polarized in the $z$ direction, as does the fact that the degree of polarization is nearly unity for SPP fields in general (Norrman et al., 2016).

## 5.5 Structured axiconic fields

Structured light, referring to optical fields with tailored amplitude, phase, and polarization profiles, attracts ever-growing attention and has interdisciplinary influences on many applications (Rubinsztein-Dunlop et al., 2016). *Structured SPP fields* occur in the form of Bessel (Bliokh, Gorodetski, Kleiner, & Hasman, 2008; Garcia-Ortiz, Coello, Han, & Bozhevolnyi, 2013; Lerman, Yanai, & Levy, 2009), vortex (Gorodetski, Niv, Kleiner, & Hasman, 2008; Kim et al., 2010), long-range nondiffracting cosine-Gaussian (Lin et al., 2012), polarization-tunable (Lin et al., 2013), and self-accelerating Airy beams (Epstein & Arie, 2014; Minovich et al., 2011; Salandrino & Christodoulides, 2010), among others (Wang & Zhao, 2019). Nevertheless, most structured SPP fields investigated so far have been either monochromatic, i.e., spatially and temporally coherent, or polychromatic but spatially completely coherent. Only very recently structured SPP fields of arbitrary spectrum and arbitrary degree of coherence have been explored (Chen et al., 2018a, 2018b, 2019).

We first review a class of structured, partially coherent SPP fields reminiscent of traditional optical axicon fields (Jaroszewicz, Burvall, & Friberg, 2005), referred to as *axiconic surface plasmon polariton (ASPP) fields* (Chen et al., 2018b). The considered geometry is akin to the usual Kretschmann setup (Fig. 23), but now the SPP field at the metal–air interface ($z = 0$) is composed of *radially propagating* SPPs with their excitation positions distributed uniformly along a circular ring of radius $a$. We let $\mathbf{r}_0 = -a\hat{\mathbf{e}}_{\parallel}(\theta)$ represent the excitation point of an SPP that propagates in the direction of $\hat{\mathbf{e}}_{\parallel}(\theta) = \cos\theta\hat{\mathbf{e}}_x + \sin\theta\hat{\mathbf{e}}_y$ toward the circle center ($\mathbf{r} = 0$), where $0 \leq \theta < 2\pi$ is the azimuthal angle with respect to the $x$ axis. On taking all the contributing SPPs into account, the spatial electric part of the ASPP field in air, for $(x^2+y^2)^{1/2} \leq a$ and at angular frequency $\omega$, is given by (Chen et al., 2018b)

$$\mathbf{E}(\mathbf{r},\omega) = \int_0^{2\pi} E(\theta,\omega)\hat{\mathbf{p}}(\theta,\omega)\mathrm{e}^{\mathrm{i}\mathbf{k}(\theta,\omega)\cdot[\mathbf{r}-\mathbf{r}_0(\theta)]}\mathrm{d}\theta, \tag{85}$$

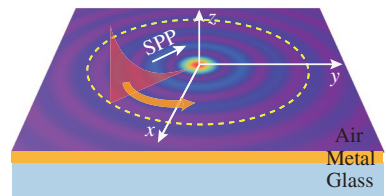


**Fig. 23** Geometry for synthesis of structured partially coherent SPP fields via radially propagating SPPs of arbitrary correlations. One of the SPPs, excited on a circle at the metal–air interface and propagating toward the center, is explicitly displayed in the figure.

where $E(\theta, \omega)$ is a complex field amplitude of the monochromatic SPP at the excitation point, and

$$\mathbf{k}(\theta,\omega) = k_{\parallel}(\omega)\hat{\mathbf{e}}_{\parallel}(\theta) + k_z(\omega)\hat{\mathbf{e}}_z, \quad \hat{\mathbf{p}}(\theta,\omega) = \hat{\mathbf{k}}(\theta,\omega) \times [\hat{\mathbf{e}}_z \times \hat{\mathbf{e}}_{\parallel}(\theta)] \quad (86)$$

are the corresponding SPP wave and unit polarization vectors, respectively, with $\hat{\mathbf{k}}(\theta, \omega) = \mathbf{k}(\theta, \omega)/|\mathbf{k}(\omega)|$ [we note that the wave-vector magnitude $|\mathbf{k}(\omega)|$ is independent of $\theta$]. Again, the film is assumed thick enough so that mode overlap across the metal is negligible, whereupon the tangential and normal wave-vector components in Eq. (86) coincide with those in Eq. (50).

Considering $\mathbf{E}(\mathbf{r}, \omega)$ in Eq. (85) as a realization of a *stationary* field, the *ASPP spectral coherence matrix* [Eq. (2)] takes the form

$$\mathbf{W}(\mathbf{r}_1,\mathbf{r}_2,\omega) = \mathrm{e}^{-2k_{\parallel}''(\omega)a} \iint_0^{2\pi} W(\theta_1,\theta_2,\omega)\hat{\mathbf{p}}^*(\theta_1,\omega)\hat{\mathbf{p}}^{\mathrm{T}}(\theta_2,\omega) \times \mathrm{e}^{\mathrm{i}[\mathbf{k}(\theta_2,\omega)\cdot\mathbf{r}_2 - \mathbf{k}^*(\theta_1,\omega)\cdot\mathbf{r}_1]}\mathrm{d}\theta_1\mathrm{d}\theta_2, \quad (87)$$

where the double prime denotes the imaginary part, as before, and

$$W(\theta_1,\theta_2,\omega) = \langle E^*(\theta_1,\omega)E(\theta_2,\omega)\rangle \quad (88)$$

is the *angular SPP correlation function*. Eq. (87) shows that the excitation circle radius $a$ acts effectively merely as a scaling factor of $\mathbf{W}(\mathbf{r}_1, \mathbf{r}_2, \omega)$, and thereby of all the quantities derived from it, highlighting the *structural stability* of the ASPP field with respect to variations in $a$ (Chen et al., 2018b). Yet, in practical cases, the SPP propagation length $l_{\mathrm{SPP}}(\omega) = 1/k_{\parallel}''(\omega)$ serves as a natural maximum radius. Furthermore, utilizing plasmon coherence engineering enables to sculpt the angular SPP correlation function $W(\theta_1, \theta_2, \omega)$ into virtually any form, thus rendering the ASPP fields broadly versatile as regards their fundamental physical properties, such as the spectral density, polarization state, energy flow, and coherence (Chen et al., 2018b).

Fig. 24A illustrates the spectral density [Eq. (5)] for an ASPP field composed of correlated SPPs on an Ag/air interface at free-space wavelength $\lambda = 532$ nm for $a = l_{\mathrm{SPP}}(\lambda)$. Each SPP mode has the same initial intensity $\langle|E(\theta, \omega)|^2\rangle = \langle|E(\omega)|^2\rangle = I_{\mathrm{SPP}}(\omega)$. The profile displays clearly the characteristic oscillatory pattern of an axicon field, similar to that of a plasmonic lens (Lerman et al., 2009; Liu et al., 2005), with a strong and highly confined peak at the circle center, induced by interference among the SPPs. As the SPP correlations become weaker, the confined intensity

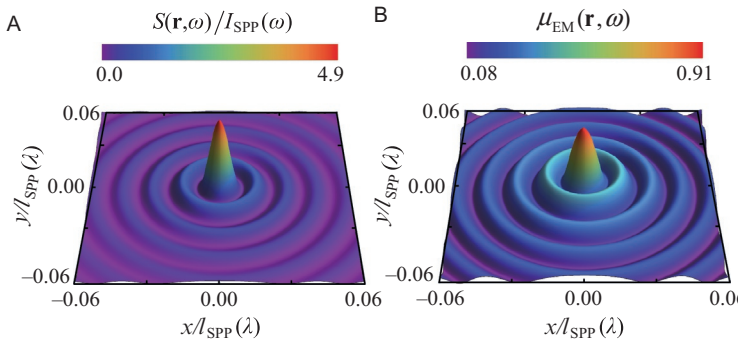


**Fig. 24** (A) Spatial behavior of the spectral density $S(\mathbf{r}, \omega)$ for an ASPP field composed of fully correlated SPPs, and (B) spatial behavior of the spectral electromagnetic degree of coherence $\mu_{\mathrm{EM}}(\mathbf{r}, \omega)$ for an ASPP field consisting of fully uncorrelated SPPs, at an Ag/air surface at free-space wavelength $\lambda = 532$ nm. In (A) $I_{\mathrm{SPP}}(\omega)$ is the initial SPP intensity and $a = l_{\mathrm{SPP}}(\lambda)$, where $a$ is the circle radius and $l_{\mathrm{SPP}}(\lambda)$ is the SPP propagation length. In (B) $\mu_{\mathrm{EM}}(\mathbf{r}, \omega)$ is independent of $a$ but $(x^2+y^2)^{1/2} \leq a$. The complex permittivity of Ag is from empirical data (Palik, 1998). *From Chen, Y., Norrman, A., Ponomarenko, S. A., & Friberg, A. T. (2018b). Partially coherent axiconic surface plasmon polariton fields. Physical Review A, 97(4), 041801(R).*

at the center gradually fades away and the spatial distribution of the spectral density becomes smoothly distributed over the interior of the circle (Chen et al., 2018b). In the fully uncorrelated limit, the oscillatory pattern totally disappears and the maximum spectral density shifts toward the excitation positions (circle's edge). Nevertheless, as shown in Fig. 24B, with $\mathbf{r}_1 = 0$ and $\mathbf{r}_2 = \mathbf{r}$, the axiconic profile *reemerges* in the electromagnetic degree of coherence [Eq. (28)] due to statistical similarity (Ponomarenko et al., 2005; Voipio et al., 2015), whereby the ASPP field is highly coherent near the center even if the SPPs are fully uncorrelated and thus do not interfere (Chen et al., 2018b).

## 5.6 Structured lattice fields

The second class of structured, partially coherent SPP fields that we consider are *surface plasmon polariton lattice (SPPL) fields* (Chen et al., 2018a). The geometry is the same as for ASPP fields (Fig. 23), but instead of an SPP mode continuum the SPPL fields consist of a *discrete* number $N$ of uniformly distributed SPPs, such that $\mathbf{r}_{0n} = -a\hat{\mathbf{e}}_n$ represents the excitation position of the $n$th SPP propagating in the direction $\hat{\mathbf{e}}_n = \cos\theta_n\hat{\mathbf{e}}_x + \sin\theta_n\hat{\mathbf{e}}_y$ toward the

circle center, with $\theta_n = 2\pi(n-1)/N$ being the respective azimuthal angle. The SPPL electric field realization in air is then (Chen et al., 2018a)

$$\mathbf{E}(\mathbf{r},\omega) = \sum_{n=1}^{N} E_n(\omega)\hat{\mathbf{p}}_n(\omega)\mathrm{e}^{\mathrm{i}\mathbf{k}_n(\omega)\cdot(\mathbf{r}-\mathbf{r}_{0n})}, \tag{89}$$

where $E_n(\omega)$ is the spectral amplitude of the $n$th SPP mode at the excitation point, while the SPP wave and unit polarization vectors read

$$\mathbf{k}_n(\omega) = k_{\parallel}(\omega)\hat{\mathbf{e}}_n + k_z(\omega)\hat{\mathbf{e}}_z, \quad \hat{\mathbf{p}}_n(\omega) = \hat{\mathbf{k}}_n(\omega)\times(\hat{\mathbf{e}}_z\times\hat{\mathbf{e}}_n) \tag{90}$$

with $\hat{\mathbf{k}}_n(\omega) = \mathbf{k}_n(\omega)/|\mathbf{k}(\omega)|$. As for the ASPP fields, the wave-vector magnitude $|\mathbf{k}(\omega)|$ is independent of $\theta_n$, and the tangential and normal wave-vector components in Eq. (90) are the same as those in Eq. (50).

Averaging over the electric field realizations in Eq. (89), we end up with the *SPPL spectral coherence matrix*

$$\mathbf{W}(\mathbf{r}_1,\mathbf{r}_2,\omega) = \mathrm{e}^{-2k_{\parallel}''(\omega)a}\sum_{n,m=1}^{N} W_{nm}(\omega)\hat{\mathbf{p}}_n^{*}(\omega)\hat{\mathbf{p}}_m^{\mathrm{T}}(\omega)\mathrm{e}^{\mathrm{i}[\mathbf{k}_m(\omega)\cdot\mathbf{r}_2-\mathbf{k}_n^{*}(\omega)\cdot\mathbf{r}_1]}, \tag{91}$$

containing the (discrete) angular SPP correlation function

$$W_{nm}(\omega) = \langle E_n^{*}(\omega)E_m(\omega)\rangle. \tag{92}$$

It follows from Eqs. (90)–(92) that for a given complex permittivity $\epsilon(\omega)$, excitation radius $a$, and mode number $N$, everything besides the SPPL spectral correlation function $W_{nm}(\omega)$ is determined in Eq. (91). Consequently, similarly to $W(\theta_1, \theta_2, \omega)$ in Eq. (88) of the ASPP field, the quantity $W_{nm}(\omega)$ provides an additional *degree of freedom* that can be tailored via plasmon coherence engineering to control the fundamental physical characteristics of the partially coherent SPPL field.

As an example, Figs. 25A–C show the spatial behavior of the spectral electromagnetic degree of coherence [Eq. (28)] for an SPPL field composed of fully uncorrelated SPPs on an Ag/air interface at free-space wavelength $\lambda = 532$ nm. Here $\mathbf{r}_1 = 0$, $\mathbf{r}_2 = \mathbf{r}$, and each SPP mode has the same initial intensity $\langle|E_n(\omega)|^2\rangle = \langle|E(\omega)|^2\rangle = I_{\mathrm{SPP}}(\omega)$. Moreover, we stress that $\mu_{\mathrm{EM}}(\mathbf{r}, \omega)$ is independent of the circle radius $a$ (for any $N$) which merely scales the general SPPL coherence matrix in Eq. (91); hence the spatial coherence structure of the SPPL fields is stable (Chen et al., 2018a). Despite the absence of SPP interference, Figs. 25A–C demonstrate clearly

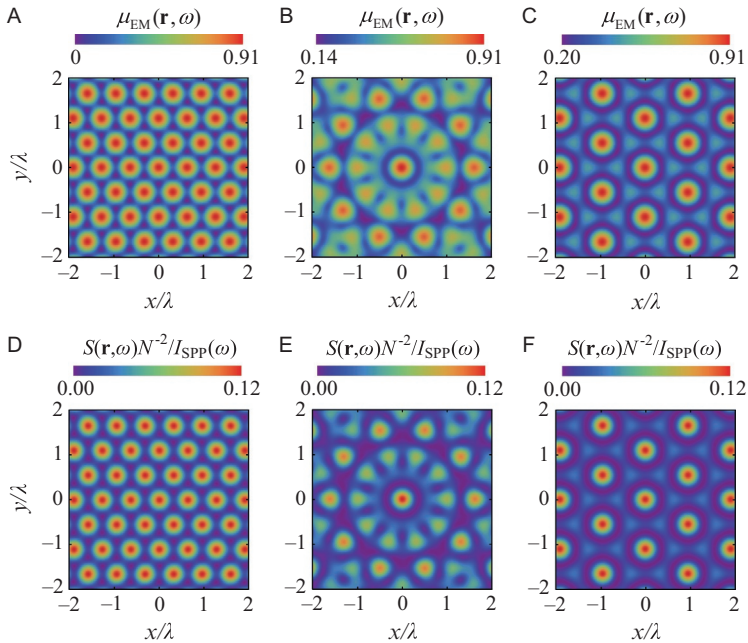


**Fig. 25** (A)–(C) Spatial behavior of the spectral electromagnetic degree of coherence $\mu_{EM}(\mathbf{r}, \omega)$ for SPPL fields composed of uncorrelated SPPs at an Ag/air interface at free-space wavelength $\lambda = 532$ nm. (D)–(F) Spatial behavior of the spectral density $S(\mathbf{r}, \omega)$ for SPPL fields consisting of correlated SPPs for the same parameters as in (A)–(C). The number of SPP modes is $N = 3$ [(A) and (D)], $N = 5$ [(B) and (E)], and $N = 6$ [(C) and (F)]. Note that $S(\mathbf{r}, \omega)$ is normalized with the initial SPP intensity $I_{SPP}(\omega)$ and the squared mode number $N^2$. The complex permittivity of Ag is from empirical data (Palik, 1998). *From Chen, Y., Norrman, A., Ponomarenko, S. A., & Friberg, A. T. (2018a). Coherence lattices in surface plasmon polariton fields. Optics Letters, 43(14), 3429–3432.*

that the electromagnetic degree of coherence has a lattice-like, subwavelength structure with periodic rotational symmetry that originates from statistical similarity (Ponomarenko et al., 2005; Voipio et al., 2015). In the extreme scenario of fully correlated SPP modes, the *coherence lattices* disappear due to complete coherence, but the lattice structure remarkably reemerges in terms of *spectral density lattices* owing to beating among the SPP modes, as illustrated in Figs. 25D–F. Also *polarization lattices* can be customized by modifying the correlations of the individual SPPs via plasmon coherence engineering (Chen et al., 2018a). The subwavelength periodicity of SPPL fields is attractive for many applications, ranging from controlled excitation of random molecule or quantum dot sets (coherence lattices) to nanoparticle

trapping (spectral density or polarization lattices). In particular, partially coherent SPPL fields may be used to engineer controllable multiparticle nanoantenna array configurations which are stable to surface defects and environment fluctuations.

## 5.7 Structured vortex fields

The third and last family of structured surface electromagnetic fields that we discuss are partially coherent SPP fields carrying optical vortices, i.e., *surface plasmon polariton vortex (SPPV) fields* (Chen et al., 2019). Similarly to the ASPP fields, the SPPV fields are formed by a continuum of radially propagating SPP modes, but now each SPP is equipped with a certain initial *phase profile*. The initial phase distribution among the SPPs can be introduced, e.g., with the help of a plasmonic vortex lens, plasmonic metasurface, or by using a circularly polarized, spatially partially coherent illumination beam carrying *orbital angular momentum* (OAM). Prior to focusing the source beam onto the glass prism and metal film, one first transmits the beam through a circular spatial filter with a narrow transmission band situated in front of the prism (Fig. 26A), yielding a ring of circularly polarized light with the phase gradient following the input beam's OAM (Fig. 26B). The angle of incidence $\varphi_{\text{inc}}$, controlled by the focal distance of the focusing lens, optimizes phase matching for SPP excitation [Eq. (57)]. The illuminated ring then excites SPPs with appropriate phase distributions propagating toward the circle center.

As for the ASPP field, we let $\mathbf{r}_0(\theta) = -a\hat{\mathbf{e}}_{\parallel}(\theta)$ denote the excitation position of an individual SPP that travels in the direction $\hat{\mathbf{e}}_{\parallel}(\theta) = \cos\theta\hat{\mathbf{e}}_x + \sin\theta\hat{\mathbf{e}}_y$, where $0 \leq \theta < 2\pi$ is the azimuthal angle with respect to the $x$ axis.

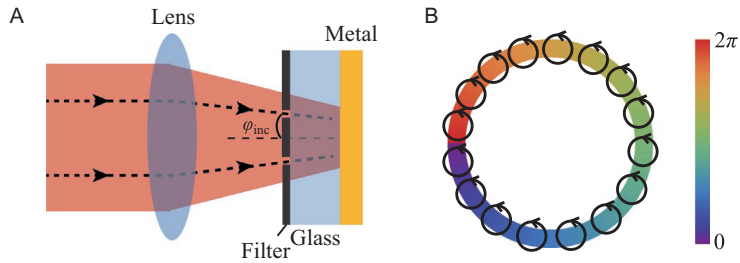


**Fig. 26** Excitation of the SPPV fields. (A) Focused circularly polarized, OAM carrying beam incident onto the circular spatial filter, glass prism, and metal slab structure, with $\varphi_{\text{inc}}$ being the angle of incidence of light selected by the filter. (B) Illustration of the polarization and phase distribution of the light on the circular ring transmitted by the filter, with $s = 1$ and $l = 1$. *From Chen, Y., Norrman, A., Ponomarenko, S. A., & Friberg, A. T. (2019). Partially coherent surface plasmon polariton vortex fields. Physical Review A, 100(5), 053833.*

Likewise, we let $\mathbf{k}(\theta, \omega)$ and $\hat{\mathbf{p}}(\theta, \omega)$ in Eq. (86) stand for the wave and unit polarization vectors, respectively, of the SPP mode. A spectral realization of the SPPV electric field in air can thus be expressed as (Chen et al., 2019)

$$\mathbf{E}(\mathbf{r}, \omega) = \int_0^{2\pi} E(\theta, \omega)\hat{\mathbf{p}}(\theta, \omega)\mathrm{e}^{\mathrm{i}\mathbf{k}(\theta,\omega)\cdot[\mathbf{r}-\mathbf{r}_0(\theta)]}\mathrm{e}^{\mathrm{i}\phi(\theta)}\mathrm{d}\theta, \tag{93}$$

where $E(\theta, \omega)$ is a complex-valued amplitude and $\phi(\theta)$ is the initial phase of the monochromatic SPP at the excitation point. As in our context the SPPV field is excited by a circularly polarized, OAM carrying incident beam, the spin–orbit coupling of light in SPP generation (Bliokh, Rodríguez-Fortuño, et al., 2015) implies that the initial phase difference between any two SPP constituents satisfy

$$\phi(\theta_1) - \phi(\theta_2) = m(\theta_1 - \theta_2). \tag{94}$$

Here $m = s + l$, with $s$ and $l$ denoting the spin and orbital angular momentum (in units of $\hbar$ per photon) of the illumination beam, respectively.

Assuming a time-stationary electric field, one obtains the *SPPV spectral coherence matrix*

$$\begin{aligned}\mathbf{W}(\mathbf{r}_1, \mathbf{r}_2, \omega) = \mathrm{e}^{-2k_{\parallel}''(\omega)a} \iint_0^{2\pi} W(\theta_1, \theta_2, \omega)\hat{\mathbf{p}}^*(\theta_1, \omega)\hat{\mathbf{p}}^{\mathrm{T}}(\theta_2, \omega) \\ \times \mathrm{e}^{\mathrm{i}[\mathbf{k}(\theta_2,\omega)\cdot\mathbf{r}_2 - \mathbf{k}^*(\theta_1,\omega)\cdot\mathbf{r}_1]}\mathrm{e}^{\mathrm{i}m(\theta_2-\theta_1)}\mathrm{d}\theta_1\mathrm{d}\theta_2,\end{aligned} \tag{95}$$

where $W(\theta_1, \theta_2, \omega)$ is the angular SPP correlation function, as specified in Eq. (88), governing the correlations among the individual SPPs excited at different angular coordinates. The coherent-mode expansion of $W(\theta_1, \theta_2, \omega)$ in terms of a two-dimensional Fourier series with respect to the angular coordinates has been adopted for analyzing the physical properties of partially coherent SPPV fields possessing arbitrary correlations (Chen et al., 2019). In particular,

$$W(\theta_1, \theta_2, \omega) = I_{\mathrm{SPP}}(\omega) \sum_{n=-\infty}^{\infty} \beta_n(\omega)\mathrm{e}^{\mathrm{i}n(\theta_2-\theta_1)}, \tag{96}$$

where $I_{\mathrm{SPP}}(\omega)$ is the initial intensity of an SPP, $n$ is the mode index, and $\beta_n(\omega)$ are real and nonnegative Fourier coefficients that ensure $W(\theta_1, \theta_2, \omega)$ is a genuine correlation function (Mandel & Wolf, 1995). Hence, each Fourier coefficient $\beta_n(\omega)$ corresponds to the modal weight that represents the amount of energy carried by the individual coherent mode.

Employing the coherent-mode representation, the energy density, energy flow, polarization, and *orbital and spin angular momenta* (OAM and SAM) of the structured SPPV fields can be assessed by regarding electromagnetic coherence as a new degree of freedom that can be controlled by adjusting the individual SPP correlations (Chen et al., 2019). Fig. 27 shows the energy density and in-plane energy flow, and Fig. 28 shows the in-plane polarization-state distribution, for SPPV fields on an Au/air interface at free-space wavelength $\lambda = 632.8$ nm with a variable number of coherent modes and average OAM. We note that in Fig. 27 also the magnetic field is taken into account. Whenever the SPPs are mutually fully uncorrelated, the average OAM and SAM for the SPPV field are zero, and the energy flow and polarization state exhibit radial distribution patterns, with the energy density showing a hot spot at the circle center (Figs. 27A and 28A), similar to that of a partially coherent ASPP field (Fig. 24). In contrast, the SPPV fields carrying OAM exhibit a circular energy flow around the excitation ring center (Figs. 27B–H), the signature of an *optical vortex*, resulting in doughnut-like energy density distributions at the metal–air interface. The energy circulation direction is determined by the sign of the average OAM: a positive OAM induces a counterclockwise circulation, whereas the energy flow is reversed for a negative OAM (Figs. 27C and D). The characteristic doughnut-type energy density distribution generally disappears as the number of coherent modes is increased (Figs. 27E–H), implying reduced spatial coherence. For example, when the number of modes reaches 15 (Fig. 27H), the energy density displays a flat-top profile at the metal surface, caused by partially impaired interference among the partially correlated SPPs.

Moreover, the in-plane polarization distribution of the partially coherent SPPV fields carrying OAM has a rather intricate local structure, exhibiting nonuniform regions of elliptical polarization (Figs. 28B–H). Hence, such SPPV fields carry also a *nonzero average SAM*. Further, as the average OAM flips sign, the right and left elliptically polarized regions switch places (Figs. 28C and D), thereby causing the SAM to change direction. We also observe that the polarization distribution of the fully coherent SPPV field, composed of only a single coherent mode, is quite involved (Fig. 28E). As the number of modes increases, therefore reducing the field coherence, the in-plane polarization turns progressively more radial (Figs. 28F–H) and becomes strictly radial in the limit $N \to \infty$. The novel physical properties of the SPPV fields are expected to find numerous applications, for instance, to nanoparticle trapping and angular momentum controlled SPP lasers.

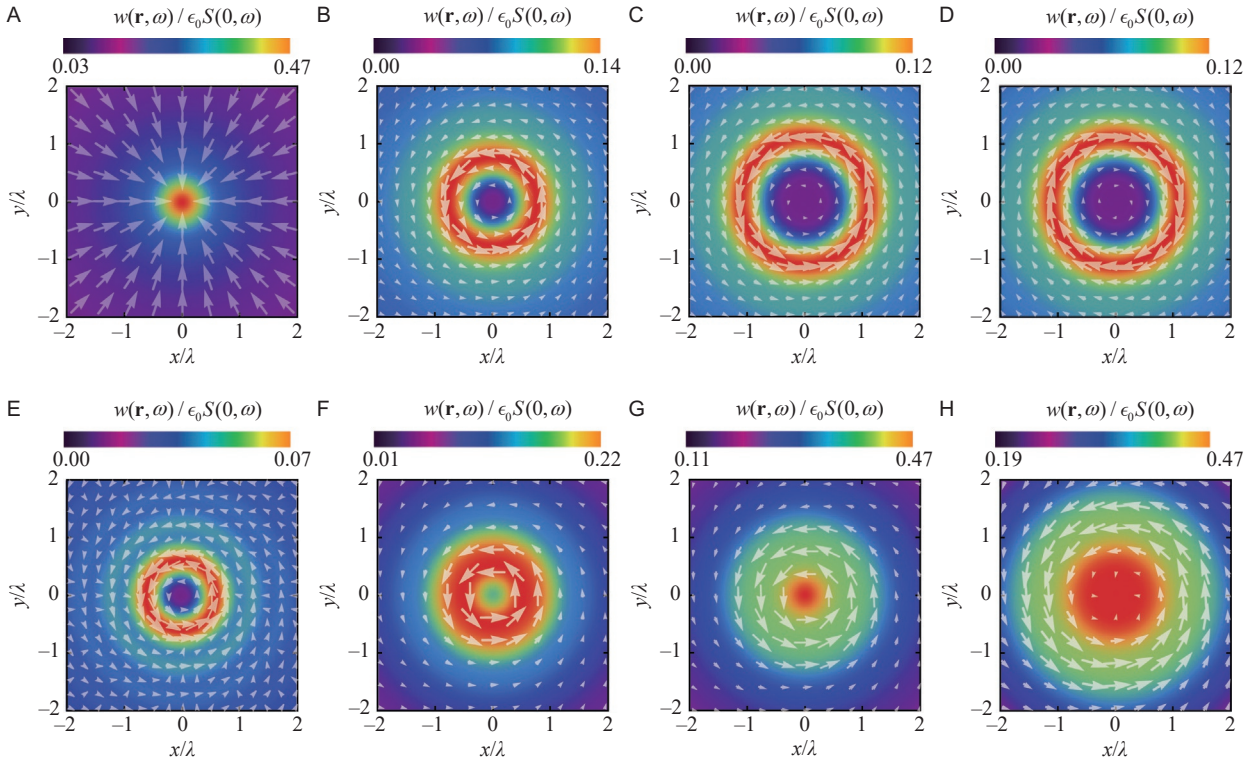


**Fig. 27** Energy density $w(\mathbf{r}, \omega)$ and the in-plane Poynting vector components for SPPV fields on an Au/air interface at free-space wavelength $\lambda = 632.8$ nm, for different numbers of coherent modes $N$ and average OAM $\mathcal{L}(\omega)$: (A) $N = 3$, $\beta_n(\omega) = 1$ for $n \in (-3, -2, -1)$, $\mathcal{L}(\omega) = 0$; (B) $N = 3$, $\beta_n(\omega) = 1$ for $n \in (1, 2, 3)$, $\mathcal{L}(\omega) = 4\hbar\hat{\mathbf{e}}_z$; (C) $N = 3$, $\beta_n(\omega) = 1$ for $n \in (3, 4, 5)$, $\mathcal{L}(\omega) = 6\hbar\hat{\mathbf{e}}_z$; (D) $N = 3$, $\beta_n(\omega) = 1$ for $n \in (-9, -8, -7)$, $\mathcal{L}(\omega) = -6\hbar\hat{\mathbf{e}}_z$; (E) $N = 1$, $\beta_n(\omega) = 1$ for $n = 1$, $\mathcal{L}(\omega) = 3\hbar\hat{\mathbf{e}}_z$; (F) $N = 5$, $\beta_n(\omega) = 1$ for $n \in (-1, \ldots, 3)$, $\mathcal{L}(\omega) = 3\hbar\hat{\mathbf{e}}_z$; (G) $N = 9$, $\beta_n(\omega) = 1$ for $n \in (-3, \ldots, 5)$, $\mathcal{L}(\omega) = 3\hbar\hat{\mathbf{e}}_z$; (H) $N = 15$, $\beta_n(\omega) = 1$ for $n \in (-6, \ldots, 8)$, $\mathcal{L}(\omega) = 3\hbar\hat{\mathbf{e}}_z$. The excitation light angular momentum is fixed at $m = 2$ and the excitation ring radius is $a = l_{\mathrm{SPP}}(\lambda)$. The energy density $w(\mathbf{r}, \omega)$ is normalized with respect to $\epsilon_0 S(0, \omega)$, where $\epsilon_0$ is the vacuum permittivity and $S(0, \omega) = 4\pi^2 l_{\mathrm{SPP}}(\omega) \exp\left[-2k''_{\parallel}(\omega)a\right]$. The complex permittivity of Au is from empirical data (Palik, 1998). *From Chen, Y., Norrman, A., Ponomarenko, S. A., & Friberg, A. T. (2019). Partially coherent surface plasmon polariton vortex fields. Physical Review A, 100(5), 053833.*

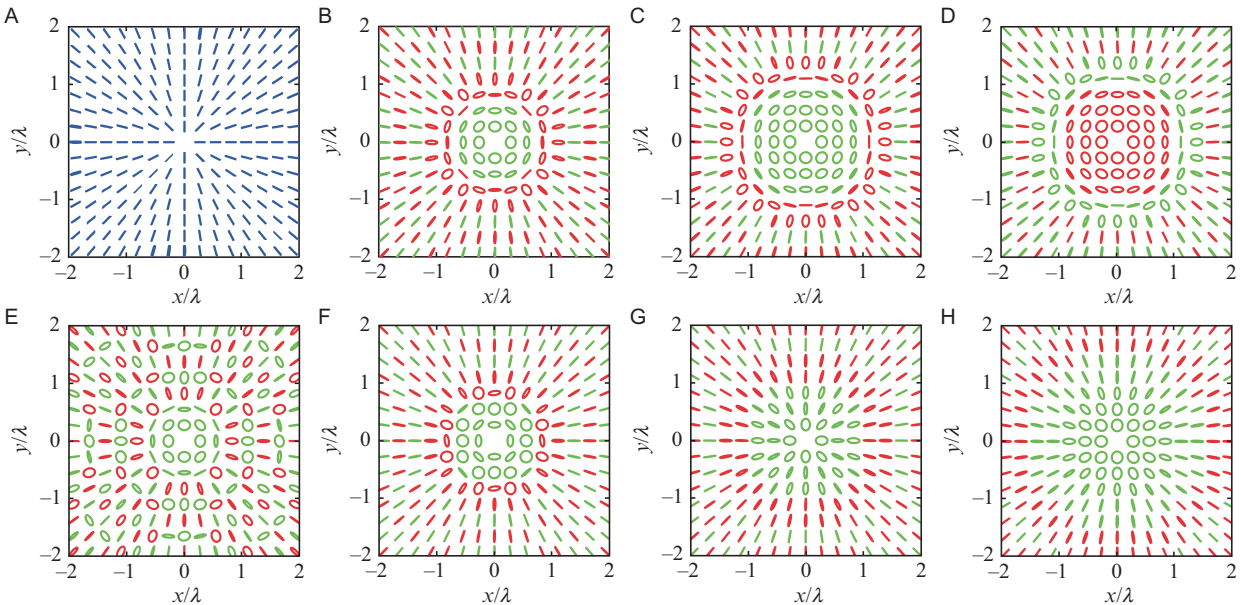


**Fig. 28** Polarization-state distribution of the in-plane electric component for the SPPV fields of Fig. 27. The blue lines correspond to linear polarization, while the orange and green ellipses represent right and left elliptical polarizations, respectively. *From Chen, Y., Norrman, A., Ponomarenko, S. A., & Friberg, A. T. (2019). Partially coherent surface plasmon polariton vortex fields. Physical Review A, 100(5), 053833.*

## 6. Concluding remarks

In conclusion, we have reviewed the fundamental discoveries and recent progress in the application of optical coherence theory to electromagnetic surface waves. Although optical coherence and electromagnetic surface waves are both venerable subjects, the two first crossed their paths only a couple of decades ago. The two key results that have emerged since then may be summarized as follows. On the one hand, it has been firmly established that the presence of surface-wave excitations in a system can profoundly affect the coherence properties of external light fields. In particular, surface-wave resonances may have significant impacts on the spectrum, polarization, and spatial correlation properties of thermal near-field radiation, and they can be harnessed to modulate, control, and measure the spatial coherence of optical beams in various interferometric contexts. On the other hand, there is now a solid recognition that coherence of electromagnetic surface waves themselves does not only yield deeper understanding of optical near-field coherence, but it also provides a novel and versatile degree of freedom to control the unique physical properties of these waves. Especially, it is now appreciated that partially polarized evanescent waves are genuinely three-dimensional in nature with subwavelength coherence characteristics, and that the concept of plasmon coherence engineering enables to tailor structured SPP fields of flexible intensity, polarization, coherence, energy flow, and angular momentum distributions.

The two research thrusts that have led to these major results appear to be complementary: they facilitate fundamental insights into the intricate coherence structure of complex electromagnetic fields, and they are anticipated to find use in diverse light–matter interactions and photonic manipulations at the nanoscale. At the same time, there are naturally still a rich diversity of physics to explore and important open questions that deserve further investigation on this subject. For example, whereas coherence modulation of thermal radiation and optical beams under surface-polariton excitation has been verified in practice, to the best of our knowledge, the experimental confirmation of three-dimensional evanescent waves and structured SPP fields of controlled coherence is still lacking. The possibilities of customizing curved light trajectories, spin–orbit interactions, optical forces, nanoscale thermodynamics, and even relativistic effects through coherence control in surface-wave contexts also constitute interesting, fully unexplored research topics. Ultimately, the emergence of quantum nanophotonics and quantum

plasmonics, as well as the foundational problem of quantizing the electromagnetic near field, identify new directions and challenges for future research on optical coherence and electromagnetic surface waves.

## Acknowledgments

The authors thank José J. Gil and Tero Setälä for useful discussions related to partially coherent evanescent electromagnetic fields. Financial support is gratefully acknowledged as follows: Y.C.—National Natural Science Foundation of China (NSFC) (11904247), Natural Science Foundation of Jiangsu Higher Education Institutions of China (19KJB140017), Natural Science Foundation of Shandong Province (ZR2019QA004); A.N.—Swedish Cultural Foundation in Finland, Jane and Aatos Erkko Foundation; S.A.P.—Natural Sciences and Engineering Research Council of Canada (RGPIN-2018-05497), Joensuu University Foundation; ATF—Academy of Finland (310511). This work is part of the Academy of Finland Flagship Program "Photonics Research and Innovation" (PREIN, 320166).

## References

Aberra Guebrou, S., Laverdant, J., Symonds, C., Vignoli, S., & Bellessa, J. (2012). Spatial coherence properties of surface plasmon investigated by Young's slit experiment. *Optics Letters*, *37*(11), 2139–2141.

Agranovich, V. M., & Mills, D. L. (1982). *Surface polaritons*. Amsterdam: North-Holland.

Aiello, A., & Banzer, P. (2016). The ubiquitous photonic wheel. *Journal of Optics*, *18*(8), 085605.

Aiello, A., Banzer, P., Neugebauer, M., & Leuchs, G. (2015). From transverse angular momentum to photonic wheels. *Nature Photonics*, *9*(12), 789–795.

Apostol, A., & Dogariu, A. (2003). Spatial correlations in the near field of random media. *Physical Review Letters*, *91*(9), 093901.

Auñón, J. M., & Nieto-Vesperinas, M. (2011). Near-field spatial correlations from partially coherent homogeneous planar sources: Effects on surface wave excitation. *Optics Letters*, *36*(17), 3410–3412.

Auñón, J. M., & Nieto-Vesperinas, M. (2013). Partially coherent fluctuating sources that produce the same optical force as a laser beam. *Optics Letters*, *38*(15), 2869–2872.

Axelrod, D. (2001). Total internal reflection fluorescence microscopy in cell biology. *Traffic*, *2*(11), 764–774.

Babuty, A., Joulain, K., Chapuis, P.-O., Greffet, J.-J., & De Wilde, Y. (2013). Blackbody spectrum revisited in the near field. *Physical Review Letters*, *110*(14), 146103.

Bliokh, K. Y. (2018). Lorentz-boosted evanescent waves. *Physics Letters A*, *382*(25), 1695–1700.

Bliokh, K. Y., Bekshaev, A. Y., & Nori, F. (2014). Extraordinary momentum and spin in evanescent waves. *Nature Communications*, *5*, 3300.

Bliokh, K. Y., Gorodetski, Y., Kleiner, V., & Hasman, E. (2008). Coriolis effect in optics: Unified geometric phase and spin-Hall effect. *Physical Review Letters*, *101*(3), 030404.

Bliokh, K. Y., & Nori, F. (2015). Transverse and longitudinal angular momenta of light. *Physics Reports*, *592*, 1–38.

Bliokh, K. Y., Rodríguez-Fortuño, F. J., Nori, F., & Zayats, A. V. (2015). Spin–orbit interactions of light. *Nature Photonics*, *9*(12), 796–808.

Bliokh, K. Y., Smirnova, D., & Nori, F. (2015). Quantum spin Hall effect of light. *Science*, *348*(6242), 1448–1451.

Blomstedt, K., Friberg, A. T., & Setälä, T. (2017). Classical coherence of blackbody radiation. *Progress in Optics*, *62*, 293–346.

Blomstedt, K., Setälä, T., & Friberg, A. T. (2007a). Arbitrarily short coherence length within finite lossless source regions. *Physical Review E*, *75*(2), 026610.
Blomstedt, K., Setälä, T., & Friberg, A. T. (2007b). Effective degree of coherence: General theory and application to electromagnetic fields. *Journal of Optics A: Pure and Applied Optics*, *9*(10), 907–919.
Blomstedt, K., Setälä, T., & Friberg, A. T. (2015). Effective degree of coherence: A second look. *Journal of the Optical Society of America A*, *32*(5), 718–732.
Born, M., & Wolf, E. (1999). *Principles of optics*. (7th ed.). Cambridge: Cambridge University Press.
Brosseau, C. (1998). *Fundamentals of polarized light: A statistical optics approach*. New York: Wiley.
Cai, Y., Chen, Y., Yu, J., Liu, X., & Liu, L. (2017). Generation of partially coherent beams. *Progress in Optics*, *62*, 157–223.
Carminati, R., & Greffet, J.-J. (1999). Near-field effects in spatial coherence of thermal sources. *Physical Review Letters*, *82*(8), 1660–1663.
Chen, Y., & Cai, Y. (2014). Generation of a controllable optical cage by focusing a Laguerre-Gaussian correlated Schell-model beam. *Optics Letters*, *39*(9), 2549–2552.
Chen, Y., Gu, J., Wang, F., & Cai, Y. (2015). Self-splitting properties of a Hermite-Gaussian correlated Schell-model beam. *Physical Review A*, *91*(1), 013823.
Chen, Y., Liu, L., Wang, F., Zhao, C., & Cai, Y. (2014). Elliptical Laguerre-Gaussian correlated Schell-model beam. *Optics Express*, *22*(11), 13975–13987.
Chen, Y., Norrman, A., Ponomarenko, S. A., & Friberg, A. T. (2017). Plasmon coherence determination by nanoscattering. *Optics Letters*, *42*(17), 3279–3282.
Chen, Y., Norrman, A., Ponomarenko, S. A., & Friberg, A. T. (2018a). Coherence lattices in surface plasmon polariton fields. *Optics Letters*, *43*(14), 3429–3432.
Chen, Y., Norrman, A., Ponomarenko, S. A., & Friberg, A. T. (2018b). Partially coherent axiconic surface plasmon polariton fields. *Physical Review A*, *97*(4), 041801(R).
Chen, Y., Norrman, A., Ponomarenko, S. A., & Friberg, A. T. (2019). Partially coherent surface plasmon polariton vortex fields. *Physical Review A*, *100*(5), 053833.
Chen, Y., Ponomarenko, S. A., & Cai, Y. (2016). Experimental generation of optical coherence lattices. *Applied Physics Letters*, *109*(6), 061107.
Chen, Y., Ponomarenko, S. A., & Cai, Y. (2017). Self-steering partially coherent beams. *Scientific Reports*, *7*, 39957.
Chen, Y., Wang, F., Liu, L., Zhao, C., Cai, Y., & Korotkova, O. (2014). Generation and propagation of a partially coherent vector beam with special correlation functions. *Physical Review A*, *89*(1), 013801.
Daniel, S., Saastamoinen, K., Ponomarenko, S. A., & Friberg, A. T. (2019). Scattering of partially coherent surface plasmon polariton fields by metallic nanostripe. *Journal of the European Optical Society-Rapid Publications*, *15*(1), 4.
Daniel, S., Saastamoinen, K., Saastamoinen, T., Rahomäki, J., Friberg, A. T., & Visser, T. D. (2015). Dynamic control of optical transmission through a nano-slit using surface plasmons. *Optics Express*, *23*(17), 22512–22519.
de Fornel, F. (2001). *Evanescent waves: From Newtonian to atomic optics*. Berlin: Springer.
Dennis, M. R. (2004). Geometric interpretation of the three-dimensional coherence matrix for nonparaxial polarization. *Journal of Optics A: Pure and Applied Optics*, *6*(3), S26.
Divitt, S., Frimmer, M., Visser, T. D., & Novotny, L. (2016). Modulation of optical spatial coherence by surface plasmon polaritons. *Optics Letters*, *41*(13), 3094–3097.
Ebbesen, T. W., Lezec, H. J., Ghaemi, H. F., Thio, T., & Wolff, P. A. (1998). Extraordinary optical transmission through sub-wavelength hole arrays. *Nature*, *391*(6668), 667–669.
Ellis, J., & Dogariu, A. (2004). Complex degree of mutual polarization. *Optics Letters*, *29*(6), 536–538.

Epstein, I., & Arie, A. (2014). Arbitrary bending plasmonic light waves. *Physical Review Letters*, *112*(2), 023903.
Erkmen, B. I., & Shapiro, J. H. (2010). Ghost imaging: From quantum to classical to computational. *Advances in Optics and Photonics*, *2*(4), 405–450.
Foley, J. T., Carter, W. H., & Wolf, E. (1986). Field correlations within a completely incoherent primary spherical source. *Journal of the Optical Society of America A*, *3*(7), 1090–1096.
Foley, J. T., Kim, K., & Nussenzveig, H. (1988). Field correlations within a Bessel-correlated spherical source. *Journal of the Optical Society of America A*, *5*(10), 1694–1708.
Friberg, A. T., & Setälä, T. (2016). Electromagnetic theory of optical coherence (invited). *Journal of the Optical Society of America A*, *33*(12), 2431–2442.
Gan, C. H., & Gbur, G. (2008). Spatial coherence conversion with surface plasmons using a three-slit interferometer. *Plasmonics*, *3*(4), 111–117.
Gan, C. H., Gbur, G., & Visser, T. D. (2007). Surface plasmons modulate the spatial coherence of light in Young's interference experiment. *Physical Review Letters*, *98*(4), 043908.
Gan, C. H., Gu, Y., Visser, T. D., & Gbur, G. (2012). Coherence converting plasmonic hole arrays. *Plasmonics*, *7*(2), 313–322.
Garcia-Ortiz, C. E., Coello, V., Han, Z., & Bozhevolnyi, S. I. (2013). Generation of diffraction-free plasmonic beams with one-dimensional Bessel profiles. *Optics Letters*, *38*(6), 905–907.
Garcia-Vidal, F. J., Martin-Moreno, L., Ebbesen, T. W., & Kuipers, L. (2010). Light passing through subwavelength apertures. *Reviews of Modern Physics*, *82*(1), 729–787.
Gbur, G. (2014). Partially coherent beam propagation in atmospheric turbulence. *Journal of the Optical Society of America A*, *31*(9), 2038–2045.
Gil, J. J. (2007). Polarimetric characterization of light and media. *European Physical Journal Applied Physics*, *40*(1), 1–47.
Gil, J. J. (2014). Interpretation of the coherency matrix for three-dimensional polarization states. *Physical Review A*, *90*(4), 043858.
Gil, J. J. (2015). Intrinsic Stokes parameters for 3D and 2D polarization states. *Journal of the European Optical Society-Rapid Publications*, *10*, 15054.
Gil, J. J., Friberg, A. T., Setälä, T., & San José, I. (2017). Structure of polarimetric purity of three-dimensional polarization states. *Physical Review A*, *95*(5), 053856.
Gil, J. J., Norrman, A., Friberg, A. T., & Setälä, T. (2018a). Nonregularity of three-dimensional polarization states. *Optics Letters*, *43*(19), 4611–4614.
Gil, J. J., Norrman, A., Friberg, A. T., & Setälä, T. (2018b). Polarimetric purity and the concept of degree of polarization. *Physical Review A*, *97*(2), 023838.
Gil, J. J., Norrman, A., Friberg, A. T., & Setälä, T. (2019). Intensity and spin anisotropy of three-dimensional polarization states. *Optics Letters*, *44*(14), 3578–3581.
Gil, J. J., & Ossikovski, R. (2016). *Polarized light and the Mueller matrix approach*. Boca Raton: CRC Press.
Gil, J. J., & San José, I. (2010). 3D polarimetric purity. *Optics Communications*, *283*(22), 4430–4434.
Gorodetski, Y., Niv, A., Kleiner, V., & Hasman, E. (2008). Observation of the spin-based plasmonic effect in nanoscale structures. *Physical Review Letters*, *101*(4), 043903.
Greffet, J.-J., Carminati, R., Joulain, K., Mulet, J.-P., Mainguy, S., & Chen, Y. (2002). Coherent emission of light by thermal sources. *Nature*, *416*(6876), 61–64.
Han, S. E., & Norris, D. J. (2010). Beaming thermal emission from hot metallic bull's eyes. *Optics Express*, *18*(5), 4829–4837.
Hassinen, T., Popov, S., Friberg, A. T., & Setälä, T. (2016). Generation of nearly 3D-unpolarized evanescent optical near fields using total internal reflection. *Optics Letters*, *41*(13), 2942–2945.
Henkel, C., Joulain, K., Carminati, R., & Greffet, J.-J. (2000). Spatial coherence of thermal near fields. *Optics Communications*, *186*(1–3), 57–67.

Inoue, T., De Zoysa, M., Asano, T., & Noda, S. (2014). Realization of dynamic thermal emission control. *Nature Materials*, *13*(10), 928–931.

Jaroszewicz, Z., Burvall, A., & Friberg, A. T. (2005). Axicon—the most important optical element. *Optics and Photonics News*, *16*(4), 34–39.

Jones, A. C., O'Callahan, B. T., Yang, H. U., & Raschke, M. B. (2013). The thermal near-field: Coherence, spectroscopy, heat-transfer, and optical forces. *Progress in Surface Science*, *88*(4), 349–392.

Joulain, K., Mulet, J.-P., Marquier, F., Carminati, R., & Greffet, J.-J. (2005). Surface electromagnetic waves thermally excited: Radiative heat transfer, coherence properties and Casimir forces revisited in the near field. *Surface Science Reports*, *57*(3–4), 59–112.

Józefowski, L., Fiutowski, J., Kawalec, T., & Rubahn, H.-G. (2007). Direct measurement of the evanescent-wave polarization state. *Journal of the Optical Society of America B*, *24*(3), 624–628.

Kanseri, B., Kandpal, H. C., & Budhani, R. C. (2012). Far field spectrum in surface plasmon-assisted Young's double-slit interferometer. *Optics Communications*, *285*(24), 4811–4815.

Kawalec, T., Józefowski, L., Fiutowski, J., Kasprowicz, M. J., & Dohnalik, T. (2007). Spectroscopic measurements of the evanescent wave polarization state. *Optics Communications*, *274*(2), 341–346.

Kim, H., Park, J., Cho, S.-W., Lee, S.-Y., Kang, M., & Lee, B. (2010). Synthesis and dynamic switching of surface plasmon vortices with plasmonic vortex lens. *Nano Letters*, *10*(2), 529–536.

Korotkova, O., & Wolf, E. (2005). Generalized Stokes parameters of random electromagnetic beams. *Optics Letters*, *30*(2), 198–200.

Kuzmin, N., 't Hooft, G. W., Eliel, E. R., Gbur, G., Schouten, H. F., & Visser, T. D. (2007). Enhancement of spatial coherence by surface plasmons. *Optics Letters*, *32*(5), 445–447.

Laroche, M., Carminati, R., & Greffet, J.-J. (2006). Coherent thermal antenna using a photonic crystal slab. *Physical Review Letters*, *96*(12), 123903.

Laverdant, J., Aberra Guebrou, S., Bessueille, F., Symonds, C., & Bellessa, J. (2014). Leakage interferences applied to surface plasmon analysis. *Journal of the Optical Society of America A*, *31*(5), 1067–1073.

Lee, B. J., Fu, C. J., & Zhang, Z. M. (2005). Coherent thermal emission from one-dimensional photonic crystals. *Applied Physics Letters*, *87*(7), 071904.

Leppänen, L.-P., Friberg, A. T., & Setälä, T. (2014). Partial polarization of optical beams and near fields probed with a nanoscatterer. *Journal of the Optical Society of America A*, *31*(7), 1627–1635.

Leppänen, L.-P., Saastamoinen, K., Friberg, A. T., & Setälä, T. (2014). Interferometric interpretation for the degree of polarization of classical optical beams. *New Journal of Physics*, *16*, 113059.

Leppänen, L.-P., Saastamoinen, K., Lehtolahti, J., Friberg, A. T., & Setälä, T. (2016). Detection of partial polarization of light beams with dipolar nanocubes. *Optics Express*, *24*(2), 1472–1479.

Lerman, G. M., Yanai, A., & Levy, U. (2009). Demonstration of nanofocusing by the use of plasmonic lens illuminated with radially polarized light. *Nano Letters*, *9*(5), 2139–2143.

Leskova, T. A., Maradudin, A. A., & Munoz-Lopez, J. (2005). Coherence of light scattered from a randomly rough surface. *Physical Review E*, *71*(3), 036606.

Li, D., & Pacifici, D. (2017). Strong amplitude and phase modulation of optical spatial coherence with surface plasmon polaritons. *Science Advances*, *3*(10), e1700133.

Li, W., & Fan, S. (2018). Nanophotonic control of thermal radiation for energy applications. *Optics Express*, *26*(12), 15995–16021.

Lin, J., Dellinger, J., Genevet, P., Cluzel, B., De Fornel, F., & Capasso, F. (2012). Cosine-Gauss plasmon beam: A localized long-range nondiffracting surface wave. *Physical Review Letters*, *109*(9), 093904.

Lin, J., Mueller, J. P. B., Wang, Q., Yuan, G., Antoniou, N., Yuan, X.-C., & Capasso, F. (2013). Polarization-controlled tunable directional coupling of surface plasmon polaritons. *Science*, *340*(6130), 331–334.
Lindberg, J., Setälä, T., Kaivola, M., & Friberg, A. T. (2006). Spatial coherence effects in light scattering from metallic nanocylinders. *Journal of Optics Society of America A*, *23*(6), 1349–1358.
Liu, X., Tyler, T., Starr, T., Starr, A. F., Jokerst, N. M., & Padilla, W. J. (2011). Taming the blackbody with infrared metamaterials as selective thermal emitters. *Physical Review Letters*, *107*(4), 045901.
Liu, X., Wang, L., & Zhang, Z. M. (2015). Near-field thermal radiation: Recent progress and outlook. *Nanoscale and Microscale Thermophysical Engineering*, *19*(2), 98–126.
Liu, Z., Steele, J. M., Srituravanich, W., Pikus, Y., Sun, C., & Zhang, X. (2005). Focusing surface plasmons with a plasmonic lens. *Nano Letters*, *5*(9), 1726–1729.
Luis, A. (2005). Degree of polarization for three-dimensional fields as a distance between correlation matrices. *Optics Communications*, *253*(1–3), 10–14.
Maier, S. A. (2007). *Plasmonics: Fundamentals and applications*. Berlin: Springer.
Mandel, L., & Wolf, E. (1995). *Optical coherence and quantum optics*. Cambridge: Cambridge University Press.
Mao, H., Chen, Y., Liang, C., Chen, L., Cai, Y., & Ponomarenko, S. A. (2019). Self-steering partially coherent vector beams. *Optics Express*, *27*(10), 14353–14368.
Mao, H., Chen, Y., Ponomarenko, S. A., & Friberg, A. T. (2018). Coherent pseudo-mode representation of partially coherent surface plasmon polaritons. *Optics Letters*, *43*(6), 1395–1398.
Maradudin, A. A., Sambles, J. R., & Barnes, W. L. (2014). *Modern plasmonics*. Amsterdam: Elsevier.
Minovich, A., Klein, A. E., Janunts, N., Pertsch, T., Neshev, D. N., & Kivshar, Y. S. (2011). Generation and near-field imaging of Airy surface plasmons. *Physical Review Letters*, *107*(11), 116802.
Morrill, D., Li, D., & Pacifici, D. (2016). Measuring subwavelength spatial coherence with plasmonic interferometry. *Nature Photonics*, *10*(10), 681–687.
Norrman, A. (2016). Electromagnetic coherence of optical surface and quantum light fields *(Doctoral dissertation)*. University of Eastern Finland.
Norrman, A., Blomstedt, K., Setälä, T., & Friberg, A. T. (2017). Complementarity and polarization modulation in photon interference. *Physical Review Letters*, *119*(4), 040401.
Norrman, A., Friberg, A. T., Gil, J. J., & Setälä, T. (2017). Dimensionality of random light fields. *Journal of the European Optical Society-Rapid Publications*, *13*, 36.
Norrman, A., Friberg, A. T., & Leuchs, G. (2020). Vector-light quantum complementarity and the degree of polarization. *Optica*, 7(2), 93–97.
Norrman, A., Gil, J. J., Friberg, A. T., & Setälä, T. (2019). Polarimetric nonregularity of evanescent waves. *Optics Letters*, *44*(2), 215–218.
Norrman, A., Ponomarenko, S. A., & Friberg, A. T. (2016). Partially coherent surface plasmon polaritons. *Europhysics Letters*, *116*(6), 64001.
Norrman, A., Setälä, T., & Friberg, A. T. (2011). Partial spatial coherence and partial polarization in random evanescent fields on lossless interfaces. *Journal of the Optical Society of America A*, *28*(3), 391–400.
Norrman, A., Setälä, T., & Friberg, A. T. (2013). Exact surface-plasmon polariton solutions at a lossy interface. *Optics Letters*, *38*(7), 1119–1121.
Norrman, A., Setälä, T., & Friberg, A. T. (2014a). Long-range higher-order surface-plasmon polaritons. *Physical Review A*, *90*(5), 053849.
Norrman, A., Setälä, T., & Friberg, A. T. (2014b). Surface-plasmon polariton solutions at a lossy slab in a symmetric surrounding. *Optics Express*, *22*(4), 4628–4648.

Norrman, A., Setälä, T., & Friberg, A. T. (2015a). Generation and electromagnetic coherence of unpolarized three-component light fields. *Optics Letters*, *40*(22), 5216–5219.
Norrman, A., Setälä, T., & Friberg, A. T. (2015b). Partial coherence and polarization of a two-mode surface-plasmon polariton field at a metallic nanoslab. *Optics Express*, *23*(16), 20696–20714.
Novotny, L., & Hecht, B. (2012). *Principles of nano-optics*. (2nd ed.). Cambridge: Cambridge University Press.
Ostrovsky, A. S. (2006). *Coherent-mode representations in optics*. Bellingham: SPIE Press.
Palik, E. D. (Ed.), (1998). *Handbook of optical constants of solids*. New York: Academic Press.
Park, J. H., Han, S. E., Nagpal, P., & Norris, D. J. (2016). Observation of thermal beaming from tungsten and molybdenum bull's eyes. *ACS Photonics*, *3*(3), 494–500.
Polo, J. A., Jr., Mackay, T. G., & Lakhtakia, A. (2013). *Electromagnetic surface waves: A modern perspective*. Amsterdam: Elsevier.
Ponomarenko, S. A., Roychowdhury, H., & Wolf, E. (2005). Physical significance of complete spatial coherence of optical fields. *Physics Letters A*, *345*(1–3), 10–12.
Pralle, M. U., Moelders, N., McNeal, M. P., Puscasu, I., Greenwald, A. C., Daly, J. T., … Biswas, R. (2002). Photonic crystal enhanced narrow-band infrared emitters. *Applied Physics Letters*, *81*(25), 4685–4687.
Ravets, S., Rodier, J.-C., Ea Kim, B., Hugonin, J.-P., Jacubowiez, L., & Lalanne, P. (2009). Surface plasmons in the Young slit doublet experiment. *Journal of the Optical Society of America B*, *26*(12), B28–B33.
Redding, B., Choma, M. A., & Cao, H. (2012). Speckle-free laser imaging using random laser illumination. *Nature Photonics*, *6*(6), 355–359.
Roman, P., & Wolf, E. (1960a). Correlation theory of stationary electromagnetic fields. Part II—Conservation laws. *Il Nuovo Cimento*, *17*(4), 462–476.
Roman, P., & Wolf, E. (1960b). Correlation theory of stationary electromagnetic fields. Part I—The basic field equations. *Il Nuovo Cimento*, *17*(4), 462–476.
Roychowdhury, H., & Wolf, E. (2003). Effects of spatial coherence on near-field spectra. *Optics Letters*, *28*(3), 170–172.
Rubinsztein-Dunlop, H., Forbes, A., Berry, M. V., Dennis, M. R., Andrews, D. L., Mansuripur, M., … Weiner, A. M. (2016). Roadmap on structured light. *Journal of Optics*, *19*(1), 013001.
Saastamoinen, T., & Lajunen, H. (2013). Increase of spatial coherence by subwavelength metallic gratings. *Optics Letters*, *38*(23), 5000–5003.
Sako, Y., Minoghchi, S., & Yanagida, T. (2000). Single-molecule imaging of EGFR signalling on the surface of living cells. *Nature Cell Biology*, *2*(3), 168–172.
Salandrino, A., & Christodoulides, D. N. (2010). Airy plasmon: A nondiffracting surface wave. *Optics Letters*, *35*(12), 2082–2084.
San José, I., & Gil, J. J. (2011). Invariant indices of polarimetric purity. Generalized indices of purity for $n \times n$ covariance matrices. *Optics Communications*, *284*(1), 38–47.
Schneckenburger, H. (2005). Total internal reflection fluorescence microscopy: Technical innovations and novel applications. *Current Opinion in Biotechnology*, *16*(1), 13–18.
Schouten, H. F., Kuzmin, N., Dubois, G., Visser, T. D., Gbur, G., Alkemade, P. F. A., … Eliel, E. R. (2005). Plasmon-assisted two-slit transmission: Young's experiment revisited. *Physical Review Letters*, *94*(5), 053901.
Setälä, T., Blomstedt, K., Kaivola, M., & Friberg, A. T. (2003). Universality of electromagnetic-field correlations within homogeneous and isotropic sources. *Physical Review E*, *67*(2), 026613.
Setälä, T., Kaivola, M., & Friberg, A. T. (2002). Degree of polarization in near fields of thermal sources: Effects of surface waves. *Physical Review Letters*, *88*(12), 123902.
Setälä, T., Lindfors, K., & Friberg, A. T. (2009). Degree of polarization in 3D optical fields generated from a partially polarized plane wave. *Optics Letters*, *34*(21), 3394–3396.

Setälä, T., Shevchenko, A., Kaivola, M., & Friberg, A. T. (2002). Degree of polarization for optical near fields. *Physical Review E*, *66*(1), 016615.
Setälä, T., Tervo, J., & Friberg, A. T. (2004). Complete electromagnetic coherence in the space–frequency domain. *Optics Letters*, *29*(4), 328–330.
Setälä, T., Tervo, J., & Friberg, A. T. (2006a). Contrasts of Stokes parameters in Young's interference experiment and electromagnetic degree of coherence. *Optics Letters*, *31*(18), 2669–2671.
Setälä, T., Tervo, J., & Friberg, A. T. (2006b). Stokes parameters and polarization contrasts in Young's interference experiment. *Optics Letters*, *31*(14), 2208–2210.
Shchegrov, A. V., Joulain, K., Carminati, R., & Greffet, J.-J. (2000). Near-field spectral effects due to electromagnetic surface excitations. *Physical Review Letters*, *85*(7), 1548–1551.
Shirai, T. (2017). Modern aspects of intensity interferometry with classical light. *Progress in Optics*, *62*, 1–72.
Smith, M., & Gbur, G. (2019). Coherence resonances and band gaps in plasmonic hole arrays. *Physical Review A*, *99*(2), 023812.
Starikov, A. (1982). Effective number of degrees of freedom of partially coherent sources. *Journal of the Optical Society of America*, *72*(11), 1538–1544.
Tervo, J., Setälä, T., & Friberg, A. T. (2003). Degree of coherence for electromagnetic fields. *Optics Express*, *11*(10), 1137–1143.
Tervo, J., Setälä, T., & Friberg, A. T. (2004). Theory of partially coherent electromagnetic fields in the space-frequency domain. *Journal of the Optical Society of America A*, *21*(11), 2205–2215.
Tervo, J., Setälä, T., Roueff, A., Réfrégier, P., & Friberg, A. T. (2009). Two-point Stokes parameters: Interpretation and properties. *Optics Letters*, *34*(20), 3074–3076.
Tervo, J., Setälä, T., Turunen, J., & Friberg, A. T. (2013). Van Cittert–Zernike theorem with Stokes parameters. *Optics Letters*, *38*(13), 2301–2303.
Van Mechelen, T., & Jacob, Z. (2016). Universal spin-momentum locking of evanescent waves. *Optica*, *3*(2), 118–126.
Voipio, T., Setälä, T., & Friberg, A. T. (2013). Partial polarization theory of pulsed optical beams. *Journal of the Optical Society of America A*, *30*(1), 71–81.
Voipio, T., Setälä, T., & Friberg, A. T. (2015). Statistical similarity and complete coherence of electromagnetic fields in time and frequency domains. *Journal of the Optical Society of America A*, *32*(5), 741–750.
Wang, S., & Zhao, C. (2019). Dynamical manipulation of surface plasmon polaritons. *Applied Sciences*, *9*(16), 3297.
Wang, T., Comtet, G., Le Moal, E., Dujardin, G., Drezet, A., Huant, S., & Boer-Duchemin, E. (2014). Temporal coherence of propagating surface plasmons. *Optics Letters*, *39*(23), 6679–6682.
Wolf, E. (1955). A macroscopic theory of interference and diffraction of light from finite sources II. Fields with a spectral range of arbitrary width. *Proceedings of the Royal Society of London. Series A. Mathematical and Physical Sciences*, *230*(1181), 246–265.
Wolf, E. (1956). The coherence properties of optical fields. In Z. Kopal (Ed.), *Proceedings of symposium on astronomical optics*. Amsterdam: North-Holland.
Wolf, E. (1959). Coherence properties of partially polarized electromagnetic radiation. *Il Nuovo Cimento*, *13*(6), 1165–1181.
Wolf, E. (1981). New spectral representation of random sources and of the partially coherent fields that they generate. *Optics Communications*, *38*(1), 3–6.
Wolf, E. (1982). New theory of partial coherence in the space–frequency domain. Part I: Spectra and cross spectra of steady-state sources. *Journal of the Optical Society of America*, *72*(3), 343–351.
Zayats, A. V., Smolyaninov, I. I., & Maradudin, A. A. (2005). Nano-optics of surface plasmon polaritons. *Physics Reports*, *408*(3–4), 131–314.
Zhang, J., Zhang, L., & Xu, W. (2012). Surface plasmon polaritons: Physics and applications. *Journal of Physics D: Applied Physics*, *45*(11), 113001.